Effect of Forward Sweep on the Performance of an Axial Blower

Zur Erlangung des akademischen Grades

Doktor der Ingenieurwissenschaften

der Fakultät für Maschinenbau
Karlsruhe Institut Für Technologie (KIT)
genehmigte

Dissertation

von

M.Sc. Salman Ahmad

aus Islamabad

Datum der mündlichen Prüfung:
18. May 2010

Supervisor: Professor Dr.-Ing. habil. H. Oertel
Co-Advisor: Professor Dr.-Ing. habil. U. Müller

Acknowledgements

In The name of Allah, The Most Beneficent, The Most Merciful

Looking back, I can call these years in Karlsruhe a wonderful experience, both in academic and personal terms, which I would not want to have missed.

First and foremost I would like to thank Allah (SWT) for all the success He granted me in my life, especially the successful accomplishment of this degree.

I would like to thank my thesis advisor, Prof. Dr.-Ing. habil. H. Oertel, for giving me the opportunity to work under his supervision and also for his continual support, guidance, extraordinary patience, and excellent instructions during this research.

My sincerest and warmest thanks to Prof. Dr.-Ing. habil. U. Müller as his help, encouragement and technical comments were really crucial to what I have accomplished at KIT.

A special thanks goes to Dr.-Ing. Torsten Schenkel for his continuous advice, constructive criticism, and encouragement to be better and work harder. My research benefited from many valuable discussions with him on the numerical modelling and related issues alongwith many insightful questions.

Also, I would like to thank Dr.-Ing. Ulrich Dohrmann (Late), Michael, Sebastian Krittian, Kathrin, Markus, Stefan, Sebastian Ruck, Thomas, Mark, Mrs. Hasecic and Mrs. Fritsch-Kirchner for keeping a wonderful friendly relationship and working atmosphere during my stay at Institut für Strömungslehre, KIT. Their company and support have helped this work more than they may realize. I am grateful to all of you for your time to time help on many ignorant questions that I had. Special thanks to Stefan and Thomas for their time, help, patience and encouragement while I was preparing for my final exam.

Thanks to Abbas, Abis, Fazal, Ibrahim, Mazhar, Dr.-Ing. Rafi-ullah Khan, Shafi, Tiwana, Umair, Usman, Waheed, Zain, Zeeshan and all other Pakistani fellows, friends and families who constantly reminded me that there is life outside KIT.

Very special thanks to my parents, Talmeez Ahmad and Mohammad Ahmad, for everything they have done for me. Their prayers, guidance, encouragement and unconditional love have always been the key sources of the achievements of my life. Thanks, as well, to my supportive brothers and sisters for their prayers and throughout love.

I am deeply grateful to my wife, Naveen, for her understanding, patience and loving support over the last few years. Thanks for being there for me during the difficult times. I would also like to thank my parents-in-laws for their continuous prayers and well wishes.

This degree is fully supported by HEC in the form of PhD scholarship. This support is gratefully acknowledged. I wish to thank DAAD for taking care of all the essential things during my stay in Germany. Special thanks to Mr. Ishfaq Anwar (HEC) and Mrs. Monika Osman (DAAD) for their extraordinary help and guidance.

Karlsruhe, May 2010. Salman Ahmad

Table of Contents

Acknowledgements I

Table of Contents III

1 Introduction **1**

1.1 Motivation 1

1.2 Axial Blowers 3

1.3 State of the Art 6

1.4 Thesis Scope 9

I Fundamentals **13**

2 Theoretical Aspects: Axial Blowers **15**

2.1 Classification 15

2.2 Types of Axial Flow Fans/Blowers 17

2.3 Reynold's Equations 21

  2.3.1 Continuity Equation 22

  2.3.2 Momentum Equation 23

2.4 Turbulence Modeling 26

2.5 Initial- and Boundary Conditions 27

2.6 Numerical Modeling of Axial Blower 28

  2.6.1 Transport Equations (SST $k-\omega$ Model) 28

  2.6.2 Elementary Axial-Blower Theory 29

2.7 Dimensionless Characteristics 31

  2.7.1 Reynold's Number 32

  2.7.2 Dimensionless Fundamental Equations 32

3 Numerical Fundamentals 33
3.1 Discretisation Methods 34
3.1.1 Time Discretisation 36
3.1.1.1 Explicit Euler Method 36
3.1.1.2 Implicit Euler Method 37
3.1.2 Space Discretisation 37
3.1.2.1 Second-Order Upwind Scheme 38
3.2 Implementation of Boundary Conditions 39
3.3 Solution Algorithm 40
3.3.1 SIMPLE-Algorithm 41

II Numerical Modelling 43

4 Verification and Validation 45
4.1 Verification 45
4.2 Validation 45
4.3 Validation Case 46
4.4 Numerical Model 47
4.4.1 CAD Model Setup 48
4.5 Grid Generation 49
4.5.1 Full-Assembly Setup 49
4.5.1.1 Mesh Data 51
4.5.2 Passage-to-Passage Setup 52
4.5.2.1 Mesh Data 54
4.6 Turbulence Model 56
4.6.1 Overview FLUENT Program 56
4.6.2 Boundary Conditions 56
4.6.3 Numerical Scheme and Solution Control 57
4.7 Verification Assessment 58
4.7.1 Richardson Extrapolation 59
4.7.2 Verification Results 60
4.8 Comparison and Analysis 62

III Blade Design 67

5 Design of Blade Profile 69

5.1 Background 69

5.2 Basic Definitions 70

5.2.1 Blade Sweep 70

5.2.2 Dihedral 70

5.2.3 Blade Skewness 71

5.3 Unswept (USW) Rotor: New Reference 71

5.4 New Design of Profile 74

5.4.1 Design Basis and Assumptions 75

5.4.2 Design Technique and Procedure 76

IV Results and Conclusions 79

6 Results and Discussion 81

6.1 Computational Mesh 81

6.1.1 Grid Independence 81

6.1.2 Solution Verification 83

6.2 Overall Performance 84

6.2.1 Steady State Simulations 84

6.2.2 Unsteady State Simulations 86

6.3 Flow Visualisation 87

6.3.1 Design Flow Rate: Steady State 88

6.3.1.1 Static Pressure Distribution 88

6.3.1.2 Surface Streamlines 94

6.3.1.3 3D-Flow Effects 100

6.3.1.4 Lambda$_2$ Method 101

6.3.2 Near-Stall: Steady State 103

6.3.2.1 Surface Streamlines 103

6.3.2.2 3D-Flow Effects 104

6.3.3 Near-Stall: Unsteady 106

7 Conclusions and Recommendations 113

7.1 Summary and Conclusions 113

7.2 Future Recommendations 115

V Appendix 117

A Abbreviations and Nomenclature 119

List of Figures 123

List of Tables 127

Bibliography 129

Chapter 1

Introduction

Turbomachine means a fan, pump, blower, compressor, or turbine that changes the energy level of a flowing fluid by momentum exchange while passing through individual blade rows. Turbomachines are second only to electric motors in their number and are widespread in practically all industries, ranging in power levels from a few watts to more than 100 MW. Billions of pumps and turbines are in use in the world, and thousands of companies seeking improvements in their design [91].

Turbomachinery design is perhaps the most practical and most active application of the principles of fluid mechanics. Because of the requirements of aircraft jet propulsion, new power plants (both steam and gas turbine), rocket propulsion research and high speed modern electronic devices, continuous active development can be found in this field today.

A large variety of different techniques for designing and analysing axial turbomachines exists in the scientific world. These range from simple empirical relations to full three-dimensional Euler/Navier-Stokes algorithms using finite-difference, finite-volume or finite-element methods to discretize the equations. Nowadays the development of turbomachinery is still performed mostly by improving existing geometries experimentally and/or applying simple design methods and rules out of the text books. The experience of the designer also plays a major role in this process [23, 78].

In spite of remarkable advances in the prediction of flow characteristics, there still exist some limitations. The classical design methods lead to 2D blade designs in concentrical cuts, which are then "stacked" to form a 3D blade. Although very worthwhile improvements in machine efficiency, by the use of such features as 3D blade stacking, have been reported, there is sometimes no clear understanding of their root cause [19]. This design method has come to a saturation level regarding Pressure rise Δp and Flux Q.

1.1 Motivation

Modern electronics have seen component heat loads increasing, while heat dissipation space has decreased, both factors working against the thermal designer. Rapid development in packaging technology allows electronic devices to gain faster processing speed and enhanced capabilities. However, thermal management in such environment is becoming increasingly difficult due to high heat load and dimensional constraints. Proper design and selection of fans/blowers and fin pitch in the heat sink is crucial to ensure the optimised thermal design of the system [52].

Due to the European and global regulation concerning acoustic emission, the goal of manufacturers is to substantially decrease the noise radiated by turbomachines, and in particular axial blowers, without degrading their aerodynamic performances. High rotation speed and increasing power add to the overall difficulties [53]. Thus careful design has always a decisive effect on the essential quality features; like overall efficiency, noise reduction, and the reliability of a turbomachine.

Fan engineers, very often, face the problems of designing high-efficiency fans at a given flow rate and for a given pressure rise. Design techniques are typically based on engineering experience, and may involve much trial and error before an acceptable design is finalised. The specific rotational speed and diameter comparison may aid the designer in determining reasonable values for the rotational speed and diameter of the rotor for a desired flow rate and pressure rise. Integrating the concept of free vortex flow design in the process reduces the need to build and evaluate new designs. However, the restrictions of the spanwise distributions of velocity and pressure in the free vortex flow design imply that analysis of the fan at off-design duties has only limited validity [79].

Design engineers rely on quality performance models to establish the physical relationship between diverse thermodynamic, geometric, and fluid dynamic parameters that govern turbomachinery performance. If these models are based on a rigorous, scientific foundation, they permit the designer to thoroughly optimise a new configuration and establish with confidence the performance levels to be expected when the product is introduced in the market [40].

The process of developing advanced models has endured more than a full century, and models of increased complexity have been introduced. However, many aspects of model development have not received thorough scientific evaluation. In the turbomachinery field, meanline performance models for axial turbines have been well developed and widely published; nearly the same can be said for the field of axial compressors [40]. Complex computational methods exist for analysing flows in, for example, high-speed axial flow compressors with multistage blade rows; however, the designers and manufacturers of low-speed, general-purpose axial flow fan equipment have been reluctant to embrace this technology [22]. Beyond these two examples, there is a need for more model development and improvement, particularly emphasising axial flow fans and blowers.

Laboratory data are expensive and it is not always practical to take all the desired measurements. In some industries (such as the commercial pump and blower field), data are usually limited to inlet and outlet parameters plus flow rate and speed. On the other extreme, aircraft engine applications support the detailed measurement of internal pressures, velocities, angles, and so forth [40].

The wide and rapid spread in the use of CFD (Computational Fluid Dynamics) in the design processes has led to the design of more efficient turbomachinery. The recent enhancement of the computing environment has made numerical optimisations using CFD more popular [6]. Although, computational tools for the simulation of the flows in turbomachines are being utilised for turbomachine development, the simulation is only as good as the geometry input for simulation [23]. Therefore, this tool is not enough to achieve substantial efficiency improvements. The combination of classical methods of turbomachinery performance analysis with the numerical simulations should give the significantly improved results.

Complex three-dimensional flow structure containing secondary flows, boundary layer separations, vortices and wakes, is commonly found in turbomachinery [6].

Many of the phenomena involved in turbomachinery flow can be understood and predicted on a two-dimensional (2D) or quasi-three-dimensional (Q3D) basis, but some aspects of the flow must be considered as fully three-dimensional (3D) and cannot be understood or predicted by the Q3D approach. Probably the best known of these fully 3D effects is secondary flow, which can only be predicted by a fully 3D calculation that includes the vorticity at inlet to the blade row. It has long been recognised that blade sweep and lean also produce fully 3D effects and approximate methods of calculating these have been developed. However, the advent of fully 3D flow field calculation methods has made predictions of these complex effects much more readily available and accurate so that they are now being exploited in design [19]. At the same time, the bowed blade concept considered by numerous researchers as the appropriate blade design to reduce the cascade loss has inconsistent findings and thus still required to be further investigated [81].

To investigate details in the flow and analyse its response to small changes of machine geometry, simulation and visualisation of the 3D flow in its proper spatial relationship with the channel geometry is crucial. Until 3D viscous flow calculations are able to give quantitative prediction of blade row loss and machine efficiency, considerable engineering judgement and experience will continue to be necessary in exploiting 3D flow phenomena for turbomachine design [19, 68].

It is of utmost importance to incorporate the third spatial dimension in the design method for full understanding of the flow in an axial blower.

3D blades are capable of higher efficiency. Full 3D **“*Design*”**, by solving the equations of motion with the actual boundary conditions, has not been developed so far because there is no straight-forward approach to design directly the “3-D blade geometries”. Secondary flows, vortices, boundary layer separations, wakes etc. have to be considered in this complex 3-D design.

1.2 Axial Blowers

Axial Flow Devices — propeller fans, tubeaxial fans, vaneaxial fans, and multi-stage axial blowers have essentially the same performance characteristics. All are distinguished by the fact that pressure is proportional to lift produced by the rotating airfoils of the impeller. Their performance may range from “free air” to a few bar gauge, with airflow from a very few cubic meter per second (m^3/sec) to more than 500 m^3/sec. Pressures above 1.0 bar gauge generally require air compressors.

Fans and blowers are widely used in industrial and commercial applications. In the manufacturing sector, they use about 78.7 billion kilowatt-hours of energy each year. Nowadays axial flow fans and blowers are also increasingly being used in an effort to combat with the heating problems arising due to the continual increase in load carrying capability of modern electronic components. During the design of such axial flow blowers, it is important to make them as small and as cost-effective as possible [1, 11].

Just as the heart circulates vital oxygen and blood to parts of the body, a well-designed cooling system circulates vital cooling air to components of modern electronics. The blower, like the heart, helps regulate internal temperature, which is fundamental to the preservation of the electronic device. If the internal temperature of a device rises too high, crucial components will fail to operate properly. In fact, the fan/blower can be thought of as the heart of any system: if it fails, other critical components are at risk of failure, thus leaving the entire system compromised and likely inoperable [93].

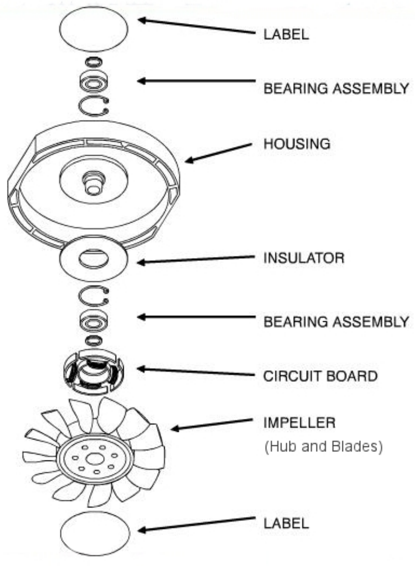

Figure 1.1: Schematic of an Axial Flow Blower

Axial blowers, as the name implies, move an airstream along the axis of the blower. The air is pressurised by the aerodynamic lift generated by the rotor blades, much like a propeller and an air plane wing. Although they can sometimes be used interchangeably with centrifugal blowers, axial blowers are commonly used in "clean air", low-pressure, high-volume applications requiring concentrated flows. Axial blowers have less rotating mass and are more compact than centrifugal blowers of comparable capacity. Additionally, axial blowers tend to have higher rotational speeds and are somewhat noisier than in-line centrifugal blowers of the same capacity; however, this noise tends to be dominated by high frequencies, which tend to be easier to attenuate. In general, they are low in cost and possess good efficiency.

A conventional axial blower is generally composed of a driving motor, a cylindrical central hub section, a plurality of blades, and a housing for encasing the blower. Each of the blades extends radially outward from the central hub section of the blower. A motor shaft of the driving motor is attached to the hub section at a central aperture. In such an arrangement, the hub section together with the blades rotate about an axis of the outer casing in order to force air flow from an inlet area to an outlet area of the blower. The rotation of blades generate a lifting force which is, in a form, the blower pressure and air flow. A breakout graphics of a typical blower is given in Figure 1.1.

The most important characteristic of a blower or a system is the relationship that links the primary variables associated with its operation. The most commonly used blower characteristic is the relationship between pressure rise/loss and volume flow rate for a constant impeller speed (rpm). Figure 1.2 represents a characteristic curve that is typical for a tubeaxial blower, and is commonly referred to as a "static pressure" curve.

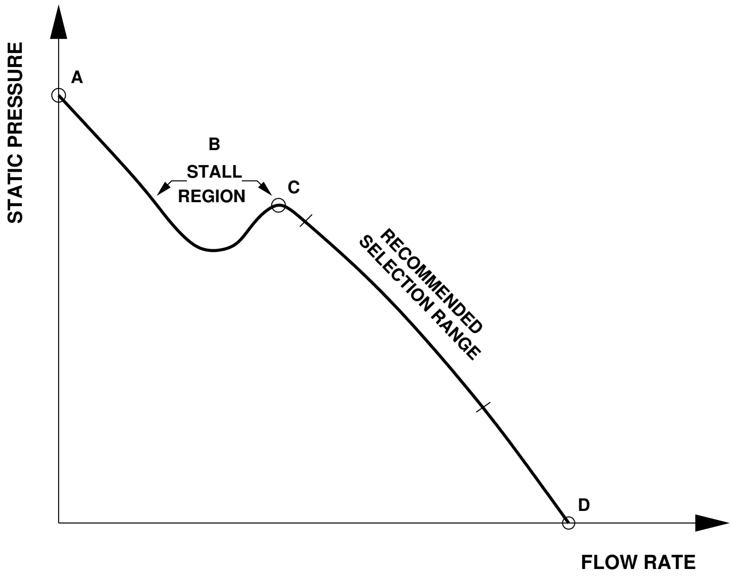

Figure 1.2: Static Pressure Curve, Axial Blower

Point A represents the point of zero airflow on the static pressure curve. It is frequently referred to as "block off", "shut off", "no flow" or "static no delivery". The region denoted by B is the stall region of the static pressure curve. Operation in this region is discouraged because of erratic airflow that generates excessive noise and vibration, thus resulting in instability and poor overall efficiency. Point C depicts what is referred to as the peak of the static pressure curve, and point D is the point of maximum airflow. Point D is also referred to as "free delivery", "free air", "wide open performance" or "wide open volume." Curve segment CD is often referred to as the right side of the fan curve. This is the stable portion of the fan curve and is where the fan is selected to operate. It then follows that curve segment AC is the left side of the fan curve and is considered to be the unstable portion of the curve.

Most densely packaged electronic systems use a fan or blower for forced-air cooling. Smaller systems usually use axial cooling fans and are best under low-pressure or low system impedance conditions [93]. Larger systems may require axial-blowers to deliver adequate airflow in high static pressure situations. Axial blowers are typically used in telecommunications and high-end servers because these systems operate under high system impedance.

The flows in turbomachines, and in particular in axial blowers, are of a very great complexity. They are characterised by their three-dimensional aspects, viscous and strongly dependant on geometrical characteristics as well as on the operating conditions [53].

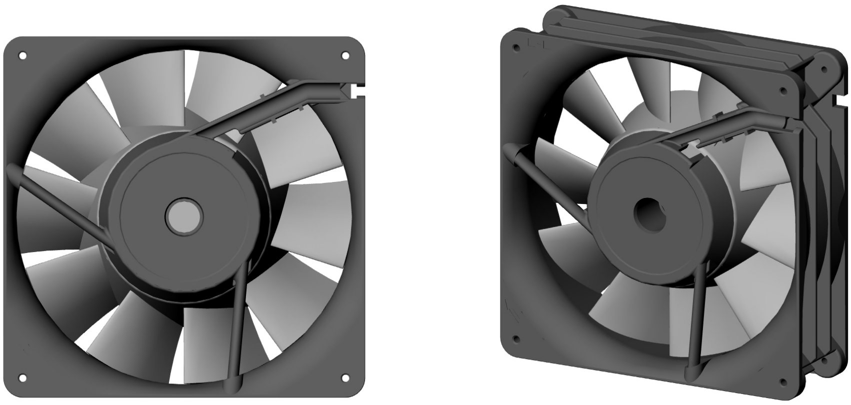

Figure 1.3: Axial Blower, PMDM

In this research work, the axial blower selected for the validation and verification studies is MF 127 made by PMDM as shown in Figure 1.3.

1.3 State of the Art

An axial flow fan or blower is simply a single-stage compressor of low pressure (and temperature) rise, so that much of the compressor theory is valid for this class of machine. The idea of using a form of *reversed turbine* as an axial compressor is as old as the reaction turbine itself. It is recorded by *Stoney* (1937) that *Sir Charles Parsons* obtained a patent for such an arrangement as early as 1884. The efficiency attained by these early, low pressure compressors was about 55%; the reason for low efficiency is now attributed to blade stall [21].

Griffith (1926) outlined the basic principles of his aerofoil theory of compressor and turbine design. The subsequent history of the axial compressor is closely linked with that of the aircraft gas turbine and has been recorded by *Cox* (1946) and *Constant* (1945). Since about 1970 a significant and special change occurred with respect to one design feature of the axial compressor and that was the introduction of low aspect ratio blading. The flow within an axial-flow compressor is exceedingly complex which is one reason why research and development on compressors has proliferated over the years [21].

Van Niekerk (1958) has investigated the theory and design of axial fans and was able to formulate expressions for calculating the optimum size and fan speeds using blade element theory. *Wallis* (1961) has extended both blade element theory and cascade data analysis to the design of complete fans [21].

The experiments performed by *Hawthorne* and *Horlock* (1962) illustrated the appreciable redistribution of flow in regions outside of the blade row and that radial velocities must exist in these regions [21].

Lichtfuss [49] has discussed the general problems and the dramatic developments taking place within the process of profile design in turbomachinery especially due to computers taking over totally the calculation process. During the last few years, manufacturers faced several unique design challenges for fans and blowers that no commercial software has been capable of addressing. To resolve current demands for designing better machines in less time, a workable approach often consists of a combination of commercial software plus scratch codes and hand calculations. While meeting these challenges, it is learnt that many of the design processes and tools used for other classes of turbomachines are also applicable to fans and blowers [3].

Reviews of numerical methods used to analyse the flow in turbomachines have been given by *Gostelow et al.* (1969), *Japikse* (1976), *Macchi* (1985), and *Whitfield* and *Baines* (1990) among many others. The literature on computer-aided methods of solving flow problems is now extremely extensive. According to *Dixon* (1998) [21], the real flow in a turbomachine is three-dimensional, unsteady, viscous and is usually compressible, if not transonic or even supersonic. He quoted *Macchi* that the solution of the full equations of motion with the actual boundary conditions of the turbomachine is still beyond the capabilities of the most powerful modern computers. *Meyer* and *Kröger* (2001) [56] pointed out that although there are quite a number of commercial CFD codes available having special features to accommodate rotating blades, etc., there is a penalty to be paid in terms of computer processing power, computational grid complexity, and the time required to obtain a solution. *Zhu et al.* (2005) [97] mentioned that with the development of computer technology in the past two decades, CFD has become popular even in the modeling of a detailed flow field of the tip clearance region.

Vad and *Bencze* [83] have studied the structure of secondary flows due to non-free vortex operation in detail and proposed a linear relationship to estimate the pitch-averaged radial velocities at the rotor exit.

Benner and *Sjolander* [9] have studied the influence of leading edge (LE) geometry on secondary losses. The results suggest that the strength of the passage vortex plays an important role in the downstream flow field and loss behaviour. The aerofoil loading distribution has more significant influence on the strength of this vortex than the LE geometry.

CFD probably plays a greater part in the aerodynamic design of turbomachinery than it does in any other engineering application. For many years the design of a modern turbine or compressor has been unthinkable without the help of CFD and this dependence has increased as more of the flow becomes amenable to numerical prediction. The benefits of CFD range from shorter design cycles to better performance and reduced costs and weight. The application of numerical methods to turbomachinery dates back to the 1940s, in fact methods were even formulated before the advent of the digital computers that were necessary to implement them [18].

Throughflow calculations remain the most important tool of the turbomachinery designer. At the very outset of the design process, after the annulus shape and mean blade angles have been determined by a one-dimensional calculation, the throughflow calculation is used to obtain the spanwise variations in flow angle at inlet and outlet to the blade rows. A review of throughflow calculation methods, covering both theory and application, was carried out by *Hirsch* and *Denton* in 1981. According to *Denton* and *Dawes* [18], the use of optimisation techniques in design seems to represent a practical way forward. Optimisation simply seeks to produce a better design than a datum subject to design constraints. This process has been increasingly adopted by the airframe industry.

Traditionally, CFD has been used in an analysis mode for cut-and-try approaches to design, in which the design process is guided by the designer's expertise, with eventually a large scattering of the results. The recent progress of the CFD code performance in terms of accuracy, sensitivity and efficiency, enables to reduce the design cycle by coupling CFD codes with optimisation tools. This can be applied with a Q3D and more recently with a fully 3D approach, with various optimisation and blade deformation techniques. The optimisation work done by *Burguburu et al.* [12], carried out with account of the tip clearance, has shown improved efficiency by more than 1 point with only low variations of the operating point.

As CFD codes have steadily evolved into everyday analysis tools, so attention is now focused on integrating the analysis codes with design tools paving the way to carry-out automatic optimisation. Automatic optimisation tools and methodologies have proved able to significantly reduce the manual design time and simultaneously improve the quality of the designs [12].

The blade sweep is one of the most usual three-dimensional blading design techniques applied in the axial fan and compressor design recently. It has been shown that sweep is effective at reducing the cross passage flow near the hub and interaction between the hub endwall and profile boundary layers in axial compressor rotors [27]. Experimental comparison of sweep and dihedral effects on compressor cascade performance clarifies that both have beneficial effects and negative effects at the same time and loss improvement depends on their balance [71]. The forward swept transonic rotor showed better results than unswept ones regarding efficiency and stall margin due to reduced shock/boundary layer interaction [89]. Significant effects on stall margin with forwards sweep producing a better stall margin and maintaining a high efficiency over a wider range have been observed in the aerodynamic studies of transonic fans [20]. *Wadia et al.* [89] showed that the forward sweep increased the stall margin of the fan, while it decreased the choke margin at the same time. On the contrary, experimental and computational studies also showed that the forward-swept bladed rotor has reduced total efficiency compared to unswept and backward swept rotors [86]. The detailed earlier experimental work on the role of forward sweep in low-speed turbomachines has been given by *Corsini* and *Rispoli* [15]. It is found recently that tip chordline sweep improves the stall margin of the compressor by modifying the suction surface boundary layer migration phenomenon [64].

The results from the numerical simulation of the flow field in the vicinity of an axial flow fan indicated that the radial forces are small compared with the axial and tangential forces exerted on the fluid stream by the fan blades [56].

Shin et al. [74] performed an experimental investigation study of the boundary layer flow on the blade suction surface of a multistage axial flow compressor. It is concluded that at the tip region of the blade, the boundary layer thickness increases steeply due to corner separation, whereas at the hub and midspan, there is no flow separation.

Henry and *Rizzi* [36] focused on the objective of getting a better insight of the flow in the rotor to improve the aerodynamic design of the fan equipment. It was concluded that the two-dimensional coupled viscous-inviscid approach is not only a prediction tool but is also appropriate for blade design and optimisation. However, the work was extended to a 3D test case and improved quality results were obtained.

Aerodynamic performance of rotor blades with different leading edge thicknesses and shapes were calculated by *Park* [62] and their effects to the performance were investigated especially in terms of total pressure loss. It was concluded that the change of total pressure loss from different leading edge thickness and shape is negligible especially in the inviscid calculation. But in viscous calculation, the change of leading edge thickness and shape can change the characteristic of boundary layer and make the analysis more complex.

The investigation by *Keskin et al.* [43] shows that an automated multi-objective optimisation process is able to solve the 2D-blade profile design problem. The numerically optimised blade is superior to the conventional design with respect to both blade performance at nominal flow conditions and at off-design conditions. The required computational time is acceptable especially since the solution contains more information than a single optimised design point. However, it is mentioned that the flow in a turbomachinery is too complicated and the 3D-CFD analysis, even on today's computers, is very much time consuming to be used in an iterative design environment.

1.4 Thesis Scope

Low to medium pressure rise axial blowers are widely used in industrial and commercial applications, with many of the installations and rotor designs being far from optimum [22]. Nowadays, the use of CFD in combination with the experimental cascade tests, the reduced scale tests and the empirical models has become a major tool for aerodynamic analysis and design of fans and blowers. Its capability of addressing the geometric complexities such as the twisting or sweeping of the blades, as well as the complex secondary and tip-clearance flows is quite helpful for a better understanding of the behaviour of the flow in the machine while saving time and costs; thus leading to better overall performance of a system.

In the recent past, experimental and numerical studies have shown some advantages of non-radial stacking (NRS) techniques in axial turbomachines. As most of the experimental results are combined with other features, it is difficult to determine the effect of individual parameters on the performance of such machines. Changing the sweep of a blade without redesigning the blade sections from baseline has been a subject of debate owing to the changes in inlet flow as well as to the pressure rise and efficiency.

The present numerical studies are aimed at understanding the effects of forward sweep incorporation on the performance and three-dimensional flow field of a single blade passage of an existing axial blower. Four forward swept blade (FSW) configurations (5°, 10°, 15° and 20°) are studied in comparison with the unswept blade (USW). The forward sweep has been incorporated to the rotor blade sections without redesigning them from baseline. All geometrical and flow features are typically preserved while incorporating the forward sweep to the blade sections for comparison purposes. The RANS steady state analyses have been carried out at different flow rates to obtain the characteristic curves of all the blowers. Unsteady simulations are run on two selected blowers (USW and 10° swept) for further understanding of the flow behaviour at near-stall condition. The research work is focused on the main objective of getting a better insight of the 3D flow of the unswept and forward swept rotors using advanced CAD and CFD tools, namely Rhinoceros®, ICEM CFD™ , GAMBIT® , FLUENT® and EnSight®.

The objectives of the present study are summarised as follows:

- Comparison of Static Pressure Curves (Δp vs. Q)
- Comparison of Total Pressure Efficiency Curves (Δp vs. η)
- Comparison of Pressure Distributions and Streamlines of Blade Surfaces
- Comparison and Discussion of 3D Flow Structures within the Blade Passage

These specific goals are achieved by following three main and standard steps. The first is the numerical modelling, verification and validation studies of the existing axial blower. The second is to modify the blower geometry to accommodate forward sweep thus introducing a new unswept (USW) reference blower (Section 5.3) and then incorporating forward sweep to it. Finally, the aerodynamic performance analyses and the 3D flow field visualisation to conclude the work.

In order to validate the numerical code, the numerical results are compared with the experimental results available from the vendor (PMDM). The simulations are performed with several appropriate assumptions and boundary conditions: incompressible, isothermal, Newtonian fluid with velocity-inlet and atmospheric outflow at main inlet and main outlet of the rotor numerical model, respectively. The technique of multiple reference frames (MRF) is adopted. The walls are considered hydraulically smooth with no-slip condition. Periodic conditions are applied on the side walls of the model. The flow in the axial blower is investigated comprehensively, especially focusing on static pressure rise, total pressure efficiency, tip leakage flow, vortices and load distribution.

Results indicated that the numerical code is validated well. An increase in pressure rise and wider stable operating range (SOR), consequently higher total pressure efficiency are obtained with higher forward sweep angles. Forward sweep changes the surface streamline pattern so that they are deflected away from the endwalls thus reducing the endwall losses. The flow visualisation showed that the tip leakage vortex (TLV) does not breakdown at design point but at near-stall, where it develops complex viscous flow structures inside the rotor passage. The corner vortex observed in case of USW at near-stall condition is not found in 10° swept blade which favours the forward sweep application. Flow separation and vortex breakdown at near-stall are the limiting factors for accurate numerical predictions in both the steady and unsteady cases.

These basic effects by forward sweeping the rotor blades can be used as references for improving the rotor-aerodynamics. The concept of forward sweep incorporation in the current study should contribute as a helpful basic tool for a better blower design with minimum effort and cost especially from industrial point of view where research investment on such appliances is not preferred.

Part I

Fundamentals

Chapter 2

Theoretical Aspects: Axial Blowers

2.1 Classification

Turbomachine is a machine that changes the energy level of a flowing fluid causing a momentum exchange. The prefix turbo- is a Latin word meaning “spin” or “whirl”, appropriate for rotating devices. A turbomachine has one or more annular blade rows (cascade) exchanging energy with the fluid crossing it and is usually connected to a rotating shaft, hence the name turbomachinery. The term “rotordynamic” is also used for this class of machines to distinguish them from positive displacement devices. The main principle of a turbomachine is that a moving blade/vane deflects a fluid jet and changes its momentum, thus forces are exerted between the vane and jet and work is done by the displacement of the vane.

The pump is the oldest fluid-energy-transfer device known. At least two designs date before Christ: (1) the undershot-bucket waterwheels, or norias, used in Asia and Africa (1000 B.C.) and (2) Archimedes’ screw pump (250 B.C.), still being manufactured today to handle solid-liquid mixtures. Paddle wheel turbines were used by the Romans in 70 B.C., and Babylonian windmills date back to 700 B.C.[91].

Turbomachines are generally known as Fans, Blowers, Compressors, Pumps and Turbines. Turbomachines are divided into two main categories which are further subdivided in several types:

1. Pumps, which add energy to the fluid
2. Turbines, which extract energy from the fluid

A pump-turbine hydraulic machine has also been developed. As the name shows, it can act as either a pump or turbine depending on the requirement.

Both, pumps and turbines, can further be classified in several types on the basis of different criteria. In the following sections, only the classification of pumps is discussed while confining within the main theme of the thesis.

The pumps are classified according to the operating principle, the fluid they are dealing with, direction of flow through the blades/cavities and the specific speed:

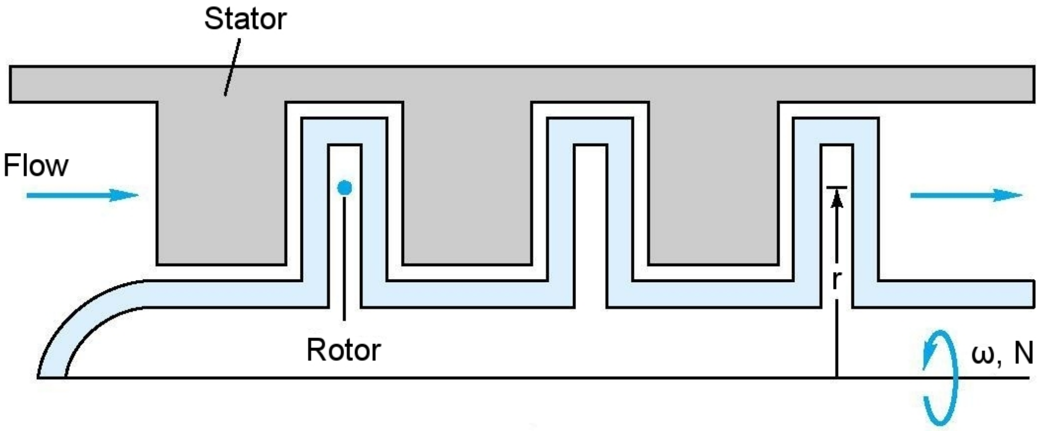

Figure 2.1: Flow in an Axial-Flow Machine

1. Operating Principle
    - Positive-Displacement Pumps (PDPs)

      Positive-displacement pumps force the fluid along by volume changes. A cavity opens and the fluid is admitted through an inlet. The cavity then closes, and the fluid is squeezed through an outlet. The mammalian heart is a good example, and many mechanical designs are in wide use.
    - Dynamic or Momentum-Change Pumps

      Dynamic pumps simply add momentum to the fluid by means of fast-moving blades or vanes or certain special designs. There is no closed volume: The fluid increases momentum while moving through open passages and then converts its high velocity to a pressure increase by exiting into a diffuser section.
2. Fluid in Contact

   Pumps can be distinguished according to fluid type they are dealing with. Machines which deliver liquids are called hydraulic pumps or simply pumps, but if gases are involved three different terms are in use, depending upon the pressure rise achieved:
    - Fan, if the pressure rise is very small (a few millibars)
    - Blower, if the pressure rise is up to 1 bar, and
    - Compressor, for above 1 bar.
3. Direction of Flow through Rotor
    - Axial Flow, the path of throughflow is totally or mainly parallel to the axis of rotation.
    - Radial Flow (Centrifugal), the throughflow path is totally or mainly in a plane perpendicular to the rotation axis.

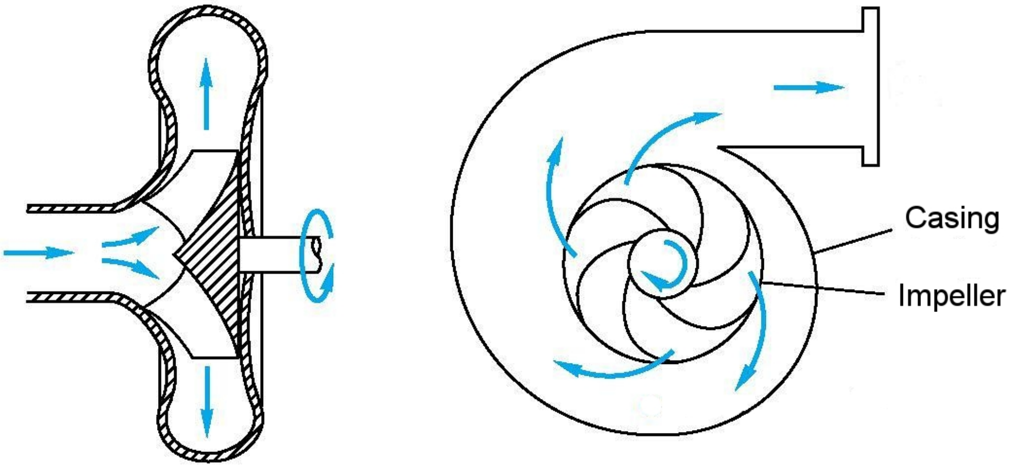

Figure 2.2: Flow in a Radial (Centrifugal) Fluid-Flow Machine

- Mixed Flow, the throughflow path having significant radial and axial velocity components.

  Figures 2.1 and 2.2 show the flow directions through the impeller of an axial pump and that of a radial pump, respectively.

4. Specific Speed
   - Low Specific Speed
   - Medium Specific Speed
   - High Specific Speed

2.2 Types of Axial Flow Fans/Blowers

Axial fans/blowers move air axially from the inlet side through to the outlet side of the fans. The individual blades of the fan/blower operate in a similar manner to that of a wing of a plane. As the blade moves through the air, negative pressure on top of the blade sucks air in and positive pressure under the blade pushes the air out. The air exits the fan/blower with a spiral swirl.

Axial fans/blowers are best used within a tube or duct, or with a wall plate to guide the air through the impeller. Mounting arms or guards are used to support the impeller within the tube or wall plate. Axial blowers are available as integral motor and impeller units, with different types of mounting arms or guards or as complete assembled blowers including the wall plate.

Axial flow fans/blowers come in many variations but all have one thing in common that they rotate about their axis and move a column of air parallel to that axis. All of the variations of axial flow fans/blowers have performance characteristics of the three basic

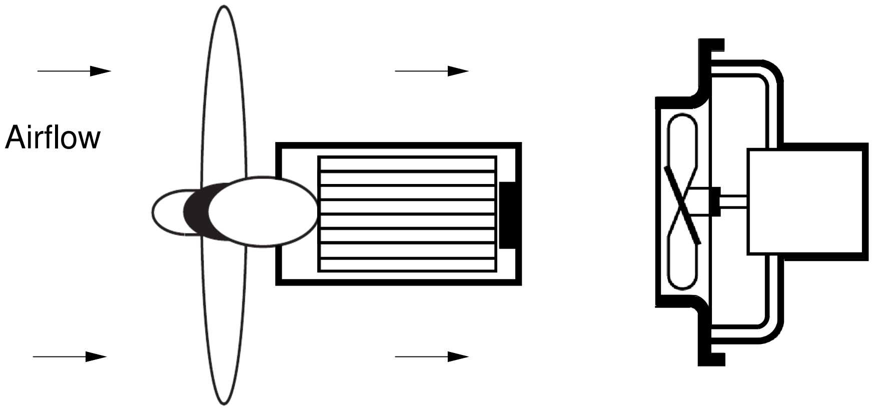

(a) (b)

Figure 2.3: Propeller Fans

types: propeller fans, tubeaxial fans and vaneaxial blowers. Multi-stage axial blower is a modified type of axial devices; but all are distinguished by the fact that pressure is proportional to lift produced by the rotating airfoils of the impeller.

1. Propeller Fans

   Propeller fans are the simplest, most economical, and least efficient axial flow devices. They can be placed in two categories:

   - Air Circulation or Free Fans:

     A free fan is one that rotates in a common unrestricted air space. Examples of free fans include ceiling fans, desk fans, pedestal fans, and wind fans. With the exception of the wind fans, most of these fans are more decorative than functional. Low tech, low cost designs function to move and stir the air, but are not necessarily the most efficient of designs.

   - Orifice Panel or Orifice Ring Fans:

     These are the fans most associated with applications referred to as ventilating fans. There are many variations of these arrangements, some with long shaft extensions, direct connection to a motor, arranged with bearings and sheaves for belt drive and close coupled belted arrangements. These fans are designed to transfer air from one large space to another. Figure 2.3 shows the schematics of both categories of propeller fans.

2. Tubaxial Fans

   The tubeaxial fan (Figure 2.4) is a propeller fan mounted in a cylindrical tube or duct and is often called a duct fan. It consists of an impeller rotating within a full cylindrical housing, which also provides motor support struts. The term tubeaxial implies more efficient airfoil blades, closer tip clearance, and generally cleaner flow patterns than the propeller fan. This results in greater pressure capability and higher

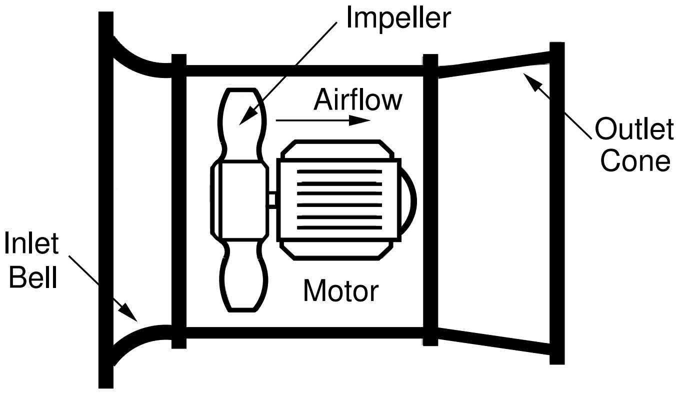

Figure 2.4: Direct Drive Tubeaxial Fan

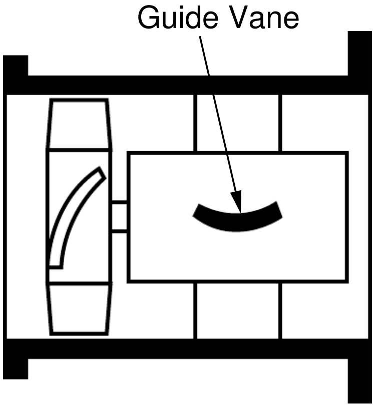

Figure 2.5: Vaneaxial Blower

efficiency. The tubeaxial fans are designed for use in ductwork systems, i.e. in the applications where there is resistance to flow.

3. Vaneaxial Blowers

   Vaneaxial Blower is the sophisticated variation of the tubeaxial fan, just as the tubeaxial represents an improvement over the propeller fan. Guide vanes are inclined on either the inlet or outlet side of the propeller. The blades are either fixed, adjustable or controllable (variable pitch-in-motion). The vanes reduce the rotational or "whirl" pattern of the air stream which results in higher pressure before stall and increased efficiency. Vaneaxial blowers are typically used in medium- to high-pressure applications, such as induced draft service for a boiler exhaust. Like tubeaxial fans, vaneaxial blowers tend to have a low rotating mass, which allows them to achieve operating speed relatively quickly. Figure 2.5 gives a general view of a vaneaxial blower.

4. Multi-Stage Axial Blowers

   Multi-Stage Axial Blower (Figure 2.6) is essentially two or more vaneaxial fans

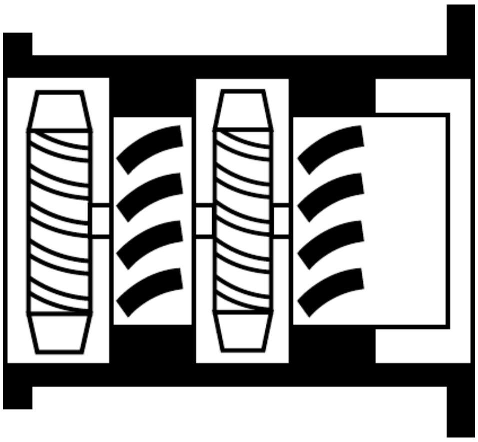

Figure 2.6: Multi-Stage Axial Blower

mounted on a common shaft and housing in series. The first vaneaxial fan, or stage, feeds the second stage with axial flow at the design point. Static pressure available is roughly the product of the number of stages and stall pressure of a single stage. Multi-stage units are capable of the highest pressures attainable by an axial device for a given size and speed. They are necessarily somewhat heavier and more expensive than the other axial units.

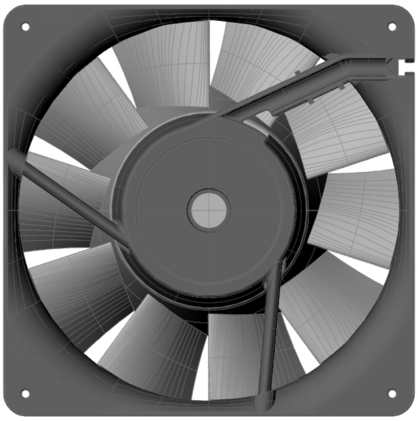

Figure 2.7: CAD-Geometry of Blower

For the current work, the axial blower chosen for the flow simulation and design improvement is MF 127 made by PMDM (Figure 2.7). The blower can be placed in tubeaxial category having a wide range of uses. Such blowers are very commonly used for the cooling and air circulation in the casings of network servers and also in the telecommunication industry. Due to their extensive use in such systems, new design challenges demand further improvements in the primary objectives which typically include aerodynamic performance, cost, durability, acoustics and size.

The selected blower has external dimensions of 127 mm × 127 mm × 38 mm. The maximum flow rate and static pressure specified by the manufacturer is 0.082 m^3/s (294 m^3/hr) and 173.3 Pa respectively. The fan's nominal rotational speed is 287 rad/s (3700 rpm) while its specific speed is 198 rpm.

2.3 Reynold's Equations

Understanding fluid dynamics has been one of the major advances of physics, applied mathematics and engineering over the last hundred years. Various mathematical methods have been established to describe the flow of fluids leading to the fundamental governing equations of fluid dynamics. These equations represent the mathematical statements of the three fundamental conservation laws of physics upon which all of fluid dynamics is based [61, 7]. The laws are known as conservation of mass, momentum, and energy. The equations derived from these laws are respectively named as continuity equation, momentum equation and the energy equation.

In a typical 3D flow field, the velocities are everywhere different in magnitude and direction. Also, the velocity at any point in the field may change with time. The flow of a fluid can be described by determining the position of every fluid particle at every point in time. A particle's change of position in time then yields its velocity and acceleration [17, 60]. Most flow problems require the analysis of an arbitrary state of variable fluid motion defined by the geometry, the boundary conditions, and the laws of mechanics. There are three basic approaches to the analysis of arbitrary flow problems [91]:

- Control-volume, or large-scale analysis
- Differential, or small-scale analysis
- Experimental, or dimensional analysis

Fluids are aggregations of molecules, widely spaced for a gas, closely spaced for a liquid. However, in general, when mathematical models are established, it is assumed that the fluid is a continuous medium—a continuum. For the analysis of fluid flows at macroscopic length scales (1 μm and larger), the molecular structure of matter and molecular motions are ignored. Instead the behaviour of the fluid is described in terms of macroscopic properties, such as velocity, pressure, density and temperature, and their space and time derivatives. In continuum approach, all fluid properties are considered to be uniformly varying functions of time and position, and can be represented as $\rho = \rho(x, y, z, t)$. The continuum field approach essentially arrives at a series of non-linear partial differential equations for each of the laws of mechanics whose solutions give the point-by-point variation in the variables.

The conservation laws are applicable to a fixed quantity of matter (system) which maintains its identity as it undergoes a change in conditions. The system is considered to have a definite position in the the space coordinates $\vec{\boldsymbol{x}} = (x, y, z)$ and is time (t) dependant. All the basic differential equations can be derived by considering either an elemental system or an infinitesimal fixed control volume $\mathrm{d}V = \mathrm{d}x \cdot \mathrm{d}y \cdot \mathrm{d}z$ having sides $\mathrm{d}x, \mathrm{d}y, \mathrm{d}z$. The governing equations are then solved for the unknown variables, namely the three velocity components u, v, w of the velocity vector $\vec{\boldsymbol{v}}$, density ρ, pressure p, and temperature T.

2.3.1 Continuity Equation

The conservation of mass or continuity equation is of fundamental importance as it must hold in every flow field no matter what type of simplifying assumptions have been made. In general, the conservation of mass at a volume element may be expressed as follows:

The rate of change of mass in a volume element
$= \sum$ *the mass fluxes into the volume element*
$- \sum$ *the mass fluxes out of the volume element.*

The mass balance gives the general form of continuity equation;

$$\frac{\partial \rho}{\partial t} + \frac{\partial(\rho \cdot u)}{\partial x} + \frac{\partial(\rho \cdot v)}{\partial y} + \frac{\partial(\rho \cdot w)}{\partial z} = 0. \tag{2.1}$$

where,

- ρ : density of fluid $[\frac{kg}{m^3}]$
- t : time $[s]$
- u, v, w : components of the velocity vector $\vec{\boldsymbol{v}}$ $[\frac{m}{s}]$

For an incompressible laminar flow, the equation simplifies to:

$$\frac{\partial u}{\partial x} + \frac{\partial v}{\partial y} + \frac{\partial w}{\partial z} = 0. \tag{2.2}$$

For a general coordinate system, the equation in vector notation is:

$$\nabla \cdot \vec{\boldsymbol{v}} = 0 \tag{2.3}$$

where the operator ∇ denotes the divergence of the vector and has the following components:

$$\nabla = \left(\frac{\partial}{\partial x}, \frac{\partial}{\partial y}, \frac{\partial}{\partial z} \right)^T .$$

Substituting the Reynolds ansatz (Section 2.3.2) in equation 2.2, the continuity equation for incompressible turbulent flows reads:

$$\frac{\partial(\overline{u})}{\partial x} + \frac{\partial(\overline{v})}{\partial y} + \frac{\partial(\overline{w})}{\partial z} = 0, \qquad \nabla \cdot \overline{\vec{\boldsymbol{v}}} = 0 \tag{2.4}$$

where $\overline{u}, \overline{v}, \overline{w}$ are the time-averaged quantities of the velocity components.

2.3.2 Momentum Equation

The conservation of momentum for a volume element can be generally stated in similar form as for mass conservation:

The rate of change of momentum in a volume element

$= \sum$ *the momentum fluxes entering the volume element*

$- \sum$ *the momentum fluxes exiting the volume element*

$+ \sum$ *the shear and normal stresses acting on the volume element*

$+ \sum$ *the forces acting on the mass of the volume element.*

The momentum of a body is defined as the product of its mass m and velocity $\vec{\boldsymbol{v}}$. It can be written in vector form as:

$$\vec{I} = m \cdot \vec{\boldsymbol{v}} \tag{2.5}$$

Balancing the momentum fluxes, shear and normal stresses, and the volume forces acting on the control volume leads to the formation of three components of the momentum equation for the x, y, and z directions. Equation 2.6 is the equation of conservation of momentum in x-direction.

$$\frac{\partial(\rho \cdot u)}{\partial t} + \frac{\partial(\rho \cdot u \cdot u)}{\partial x} + \frac{\partial(\rho \cdot u \cdot v)}{\partial y} + \frac{\partial(\rho \cdot u \cdot w)}{\partial z} = f_x + \frac{\partial \tau_{xx}}{\partial x} + \frac{\partial \tau_{yx}}{\partial y} + \frac{\partial \tau_{zx}}{\partial z} \tag{2.6}$$

where,

- ρ : density of fluid $[\frac{kg}{m^3}]$
- t : time $[s]$
- u, v, w : components of the velocity vector $\vec{\boldsymbol{v}}$ $[\frac{m}{s}]$
- τ_{xx} : normal stress in x-direction $[\frac{N}{m^2}]$
- τ_{yx}, τ_{zx} : shear stresses in x-direction $[\frac{N}{m^2}]$
- f_x : volume forces (gravity, electric, magnetic forces) in x-direction $[\frac{N}{m^3}]$

Similar equations can be written down for the y- and z-directions. The pressure p can be written as the trace of the stress tensor:

$$p = -\frac{\tau_{xx} + \tau_{yy} + \tau_{zz}}{3}. \tag{2.7}$$

The negative sign takes into account the fact that the pressure acts as a negative normal stress [60].

The three normal stresses τ_{xx}, τ_{yy}, and τ_{zz} can each be split up into two parts, the pressure p and the contributions due to the friction of the fluid, σ_{xx}, σ_{yy}, and σ_{zz}:

$$\tau_{xx} = \sigma_{xx} - p, \qquad \tau_{yy} = \sigma_{yy} - p, \qquad \tau_{zz} = \sigma_{zz} - p. \tag{2.8}$$

For the Newtonian fluids, the normal- and shear stresses can be expressed in terms of molecular viscosity μ as the following relations [60]:

$$\begin{aligned}\sigma_{xx} &= 2\cdot\mu\cdot\frac{\partial u}{\partial x}-\frac{2}{3}\cdot\mu\cdot\left(\frac{\partial u}{\partial x}+\frac{\partial v}{\partial y}+\frac{\partial w}{\partial z}\right),\\ \tau_{yx} &= \tau_{xy}=\mu\cdot\left(\frac{\partial v}{\partial x}+\frac{\partial u}{\partial y}\right),\\ \tau_{zx} &= \tau_{xz}=\mu\cdot\left(\frac{\partial u}{\partial z}+\frac{\partial w}{\partial x}\right),\end{aligned} \tag{2.9}$$

with the symmetry condition

$$\tau_{yx}=\tau_{xy},\qquad \tau_{yz}=\tau_{zy},\qquad \tau_{zx}=\tau_{xz}. \tag{2.10}$$

Inserting the normal- and shear stresses (Eq. 2.9) and the continuity equation (Eq. 2.3) into the momentum conservation equation (Eq. 2.6) gives the *Navier-Stokes equation* for incompressible laminar flows in x-direction. Equation 2.11 is the non-conservative form of Navier-Stokes equations in x, y, z coordinates for constant viscosity.

$$\begin{aligned}\rho\cdot\left(\frac{\partial u}{\partial t}+u\cdot\frac{\partial u}{\partial x}+v\cdot\frac{\partial u}{\partial y}+w\cdot\frac{\partial u}{\partial z}\right) &= f_x-\frac{\partial p}{\partial x}+\mu\cdot\left(\frac{\partial^2 u}{\partial x^2}+\frac{\partial^2 u}{\partial y^2}+\frac{\partial^2 u}{\partial z^2}\right),\\ \rho\cdot\left(\frac{\partial v}{\partial t}+u\cdot\frac{\partial v}{\partial x}+v\cdot\frac{\partial v}{\partial y}+w\cdot\frac{\partial v}{\partial z}\right) &= f_y-\frac{\partial p}{\partial y}+\mu\cdot\left(\frac{\partial^2 v}{\partial x^2}+\frac{\partial^2 v}{\partial y^2}+\frac{\partial^2 v}{\partial z^2}\right),\\ \rho\cdot\left(\frac{\partial w}{\partial t}+u\cdot\frac{\partial w}{\partial x}+v\cdot\frac{\partial w}{\partial y}+w\cdot\frac{\partial w}{\partial z}\right) &= f_z-\frac{\partial p}{\partial z}+\mu\cdot\left(\frac{\partial^2 w}{\partial x^2}+\frac{\partial^2 w}{\partial y^2}+\frac{\partial^2 w}{\partial z^2}\right).\end{aligned} \tag{2.11}$$

These equations can be summarized using vector notation as follows:

$$\rho\cdot\left(\frac{\partial\vec{\boldsymbol{v}}}{\partial t}+(\vec{\boldsymbol{v}}\cdot\nabla)\vec{\boldsymbol{v}}\right)=\vec{\boldsymbol{f}}-\nabla p+\mu\cdot\Delta\vec{\boldsymbol{v}}, \tag{2.12}$$

where ∇p is the gradient of p while $(\vec{\boldsymbol{v}}\cdot\nabla)$ is the scalar product of the velocity vector and the Nabla operator. This is a convection operator that can be applied to each component of the velocity vector $\vec{\boldsymbol{v}}$. Here $\Delta\vec{\boldsymbol{v}}$ denotes the Laplace operator applied to $\vec{\boldsymbol{v}}$:

$$\begin{aligned}\nabla p &= \left(\frac{\partial p}{\partial x},\frac{\partial p}{\partial y},\frac{\partial p}{\partial z}\right)^T,\qquad \vec{\boldsymbol{v}}\cdot\nabla=u\cdot\frac{\partial}{\partial x}+v\cdot\frac{\partial}{\partial y}+w\cdot\frac{\partial}{\partial z},\\ \Delta\vec{\boldsymbol{v}} &= \frac{\partial^2\vec{\boldsymbol{v}}}{\partial x^2}+\frac{\partial^2\vec{\boldsymbol{v}}}{\partial y^2}+\frac{\partial^2\vec{\boldsymbol{v}}}{\partial z^2}.\end{aligned} \tag{2.13}$$

Together with the continuity equation (2.2), equations (2.11) form a system of *four non-linear second-order partial differential equations* for the *four unknowns u, v, w, and p*. This system has to be solved for given initial and boundary conditions.

For turbulent flows, the time-dependent three-dimensional Navier-Stokes equations are averaged in such a manner that unsteady structures of small sizes in space and time are eliminated and are expressed by their mean effects on the flow through the so-called Reynolds or turbulent stresses. This is done by using Reynolds ansatz (incompressible flows) and the Favre averaging technique (compressible flows). The resulting equations are generally known as Reynolds Averaged Navier-Stokes (RANS) equations or simply the Reynolds equations. The Reynolds ansatz and the Favre averaging technique are applied with some standard computational rules to obtain the time-averaged continuity and Navier-Stokes equations. The Reynolds ansatz for an incompressible flow are:

$$p = \overline{p} + p', \qquad u = \overline{u} + u', \qquad v = \overline{v} + v', \qquad w = \overline{w} + w' \tag{2.14}$$

where $\overline{p}, \overline{u}, \overline{v}, \overline{w}$ are the time-averaged quantities and p', u', v', w' represent the additional fluctuations of the respective quantities.

The time averaged quantities can be expressed as:

$$\overline{u} = \frac{1}{T} \cdot \int\limits_0^T u \cdot \mathrm{d}t, \tag{2.15}$$

Thus, the Reynolds Averaged Navier-Stokes equations in x, y and z directions for an incompressible flow are:

$$\begin{aligned}
&\rho \cdot \left(\frac{\partial(\overline{u})}{\partial t} + \frac{\partial(\overline{u}^2)}{\partial x} + \frac{\partial(\overline{u} \cdot \overline{v})}{\partial y} + \frac{\partial(\overline{u} \cdot \overline{w})}{\partial z} \right) = f_x - \frac{\partial \overline{p}}{\partial x} + \\
&\frac{\partial \overline{\sigma}_{xx}}{\partial x} + \frac{\partial \overline{\tau}_{yx}}{\partial y} + \frac{\partial \overline{\tau}_{zx}}{\partial z} - \left(\frac{\partial(\rho \cdot \overline{u'^2})}{\partial x} + \frac{\partial(\rho \cdot \overline{u' \cdot v'})}{\partial y} + \frac{\partial(\rho \cdot \overline{u' \cdot w'})}{\partial z} \right),
\end{aligned} \tag{2.16}$$

$$\begin{aligned}
&\rho \cdot \left(\frac{\partial(\overline{v})}{\partial t} + \frac{\partial(\overline{v} \cdot \overline{u})}{\partial x} + \frac{\partial(\overline{v}^2)}{\partial y} + \frac{\partial(\overline{v} \cdot \overline{w})}{\partial z} \right) = f_y - \frac{\partial \overline{p}}{\partial y} + \\
&\frac{\partial \overline{\tau}_{xy}}{\partial x} + \frac{\partial \overline{\sigma}_{yy}}{\partial y} + \frac{\partial \overline{\tau}_{zy}}{\partial z} - \left(\frac{\partial(\rho \cdot \overline{v' \cdot u'})}{\partial x} + \frac{\partial(\rho \cdot \overline{v'^2})}{\partial y} + \frac{\partial(\rho \cdot \overline{v' \cdot w'})}{\partial z} \right),
\end{aligned} \tag{2.17}$$

$$\begin{aligned}
&\rho \cdot \left(\frac{\partial(\overline{w})}{\partial t} + \frac{\partial(\overline{w} \cdot \overline{u})}{\partial x} + \frac{\partial(\overline{w} \cdot \overline{v})}{\partial y} + \frac{\partial(\overline{w}^2)}{\partial z} \right) = f_z - \frac{\partial \overline{p}}{\partial z} + \\
&\frac{\partial \overline{\tau}_{xz}}{\partial x} + \frac{\partial \overline{\tau}_{yz}}{\partial y} + \frac{\partial \overline{\sigma}_{zz}}{\partial z} - \left(\frac{\partial(\rho \cdot \overline{w' \cdot u'})}{\partial x} + \frac{\partial(\rho \cdot \overline{w' \cdot v'})}{\partial y} + \frac{\partial(\rho \cdot \overline{w'^2})}{\partial z} \right)
\end{aligned} \tag{2.18}$$

In the above time-averaged Navier-Stokes equations, additional terms known as the Reynolds or turbulent stresses $\overline{u_i' \cdot u_j'}$ make the number of unknowns larger than the available equations. Additional closure relations for turbulence characteristics may have to be introduced. The Reynolds stresses must be interpreted in terms of averaged variables in order to close the system of equations which requires the construction of a turbulence model (Section 2.4).

2.4 Turbulence Modeling

Most flows of practical engineering interest are turbulent, and turbulent mixing then usually dominates the behaviour of the flow. Turbulence plays a crucial part in the determination of many relevant engineering parameters, such as frictional drag, heat transfer, flow separation, transition from laminar to turbulent flow, thickness of boundary layers, extent of secondary flows, and separating of jets and wakes.

The turbulent states which can be encountered across industrially relevant flows are rich, complex and varied. After a century of intensive theoretical and experimental research, it is now accepted that no single turbulence model can span these states and that there is no generally valid universal model of turbulence [13]. For most engineering purposes it is unnecessary to resolve the details of the turbulent fluctuations. Engineers are more interested to know the mean effect of turbulence quantities on the flow. Thus, a more practical engineering approach to describe turbulent flow is to model the averaged turbulence quantities [59, 88].

Turbulence model is a mathematical/analytical approach which is implied in the computational solution of the main flow equations, i.e. the continuity equation and the RANS equations, by making several assumptions for turbulent quantities. The purpose is to establish proper approximations for the unknown correlations in terms of known flow properties so that a sufficient number of equations exists, in other words, to close the system of equations which thus leads to the prediction of flow characteristics.

A variety of turbulence models have appeared over the years, as different developers have tried to introduce improvements to the models that are available. The available turbulence models can be roughly divided into three main categories, with the following subdivisions [59, 13]:

1. Linear eddy viscosity models
    - Algebraic (or zero-equation) models, such as mixing length models of Prandtl and Von Karman. The model uses only the partial differential equation for the mean velocity field. No partial differential equation is used for turbulent transport quantities.
    - One-equation models (with ordinary and/or partial differential equations), such as Kolmogorov (1942) or Prandtl (1945) uses one partial differential equation to model a turbulence quantity, typically the turbulent kinetic energy.
    - Two-equation models, such as k-ε or k-ω models, solve two transport equations for the turbulence quantities namely the turbulent kinetic energy k and the rate of turbulent kinetic energy dissipation ε or the specific dissipation rate ω (turbulent frequency).
2. Reynolds stress or second moment closure models
    - Full Reynolds-Stress-Transport (RST) models, they differ from the two-equation models as they model all turbulent transport quantities including all components of the turbulent stress tensor, with partial differential equations.

  - Algebraic Reynolds stress models, is a much simplified form of second moment closure in which the number of coupled differential equations is reduced to two while retaining the the subtle interaction between stress and strain

3. Non-linear eddy viscosity models (NLEVM)
    - These can be subdivided in the same way as linear eddy viscosity models but are usually implemented as two-equation models. These models retain the idea that the turbulent stresses can be algebraically related to the rate of strain however, in a non-linear relationship (i.e. time averaged velocity gradients).
    - A certain sub-class of NLEVM are equivalent to algebraic Reynolds stress models

Turbulence modeling, being an active area of research, results in the development of many other models, but they are not referred here. In the section 2.6, k-ω SST model is described briefly due to its implementation in the thesis.

2.5 Initial- and Boundary Conditions

The governing equations of fluid dynamics, discussed in section 2.3, govern the flow of a fluid and remain always the same. However, the flow fields, where these equations are applied, are quite different from each other. Moreover, the equations are build up of a system of non-linear partial differential equations of first order and second order in time and space coordinates respectively. The solution of these equations is very much difficult without some physical inputs. The initial- and boundary conditions actually dictate the particular solutions to be obtained from these governing equations.

Initial Conditions

Initial conditions are defined for a system at time, $t = 0$. The values of known variables are given as an input for starting the calculations. Mathematically the initial conditions can be written as:

$$\vec{\boldsymbol{v}}(\vec{x}, t = 0) = \vec{v}_0, \qquad p(\vec{x}, t = 0) = p_0 \tag{2.19}$$

Boundary Conditions

For a particular physical configuration, boundary conditions are defined which represent the friction, heat transfer, air flow etc. Flow and thermal variables are specified on the boundary regions of a physical model, thus acting as the constraints for the model.

Two types of boundary conditions and combinations of them are most commonly encountered.

- Dirichlet condition

  It specifies the distribution of a physical quantity over a boundary at a given time step. Applying this condition simplifies the corresponding differential equations into a solvable boundary value problem.

- Neumann condition

  It defines the distribution of the first derivative of a physical quantity over the boundary at a given time step. Applying such boundary condition results in a second order boundary value problem.

2.6 Numerical Modeling of Axial Blower

One of the main problems in turbulence modelling is the accurate prediction of flow separation from a smooth surface. Standard two-equation turbulence models often fail to predict the onset and the amount of flow separation under adverse pressure gradient conditions. This is an important phenomenon in many technical applications including the one being studied for this thesis. In general, turbulence models based on the ε- equation predict the onset of separation too late and under-predict the amount of separation later on. The prediction is therefore not on the conservative side from an engineering point of view. Separation prediction is important in many technical applications both for internal and external flows. Currently, the most prominent two-equation models in this area are the k-ω based models of Menter. The k-ω based Shear-Stress-Transport (SST) model was designed to give a highly accurate predictions of the onset and the amount of flow separation under adverse pressure gradients by the inclusion of transport effects into the formulation of the eddy-viscosity. This results in a major improvement in terms of flow separation predictions.

2.6.1 Transport Equations (SST $k - \omega$ Model)

For the present study, the physics involved in the fluid dynamics of incompressible 3D turbulent flows in rotating frame of reference is modelled by means of k-ω model, here used in its SST variant with wall function treatment. The k-ω models assume that the turbulent viscosity is linked to the turbulence kinetic energy and turbulent frequency via the relation:

$$\mu_t = \rho \cdot \frac{k}{\omega} \tag{2.20}$$

where k, the turbulent kinetic energy is the kinetic energy of the turbulent fluctuations per unit mass. It determines the energy in the turbulence while the specific dissipation rate ω determines the scale of the turbulence and is expressed as the ratio of ϵ to k, i.e., the rate of dissipation per unit turbulence kinetic energy [92]. By definition:

$$k = \frac{1}{2} \cdot \overline{u_i' \cdot u_i'} = \frac{1}{2} \cdot \left(\overline{u_1'^2} + \overline{u_2'^2} + \overline{u_3'^2} \right) \tag{2.21}$$

$$\omega = \frac{\epsilon}{k} \tag{2.22}$$

All the two equation models use Boussinesq hypothesis for the modeling of Reynolds stresses present in the RANS. The hypothesis can be written mathematically as:

$$-\rho \cdot \overline{u_i' \cdot u_j'} = \mu_t \cdot \left(\frac{\partial \overline{u}_i}{\partial x_j} + \frac{\partial \overline{u}_j}{\partial x_i} \right) - \frac{2}{3} \cdot \rho \cdot k \cdot \delta_{ij} \tag{2.23}$$

Finally, the differential transport equation for k reads:

$$\begin{aligned} \rho \cdot \frac{\partial k}{\partial t} + \rho \cdot \overline{u}_j \cdot \frac{\partial k}{\partial x_j} = \mu_t \cdot \frac{\partial \overline{u}_i}{\partial x_j} \cdot \left(\frac{\partial \overline{u}_i}{\partial x_j} + \frac{\partial \overline{u}_j}{\partial x_i} \right) + \\ \frac{\partial}{\partial x_j} \cdot \left(\mu \cdot \frac{\partial k}{\partial x_j} + \frac{\mu_t}{\sigma_k} \cdot \frac{\partial k}{\partial x_j} \right) - \beta^* \cdot \rho \cdot k \cdot \omega, \end{aligned} \tag{2.24}$$

and the differential transport equation for ω:

$$\begin{aligned} \rho \cdot \frac{\partial \omega}{\partial t} + \rho \cdot \overline{u}_j \cdot \frac{\partial \omega}{\partial x_j} = \alpha \cdot \frac{\omega}{k} \cdot \mu_t \cdot \frac{\partial \overline{u}_i}{\partial x_j} \cdot \left(\frac{\partial \overline{u}_i}{\partial x_j} + \frac{\partial \overline{u}_j}{\partial x_i} \right) + \\ \frac{\partial}{\partial x_j} \cdot \left(\mu \cdot \frac{\partial \omega}{\partial x_j} + \frac{\mu_t}{\sigma_\omega} \cdot \frac{\partial \omega}{\partial x_j} \right) - \beta \cdot \rho \cdot \omega^2 + D_\omega \end{aligned} \tag{2.25}$$

where σ_k and σ_ω are the turbulent Prandtl numbers for k and ω, respectively [4].

The SST k- ω model is based on both the standard k- ω model and the standard k- ϵ model. To blend these two models together, the standard k- ϵ model has been transformed into equations based on k and ω, which leads to the introduction of a cross-diffusion term, D_ω (Eq. 2.25). It is defined as:

$$D_\omega = 2 \cdot (1 - F_1) \cdot \rho \cdot \sigma_{\omega,2} \cdot \frac{1}{\omega} \cdot \frac{\partial k}{\partial x_j} \cdot \frac{\partial \omega}{\partial x_j} \tag{2.26}$$

where F_1 is the blending function and $\sigma_{\omega,2}$ is the closure coefficient (model constant).

2.6.2 Elementary Axial-Blower Theory

To actually predict the head, power, efficiency, and flow rate of a fan/blower, two theoretical approaches are possible:

- Simple one-dimensional-flow formulae,
- Complex computational models including viscosity and three-dimensionality.

To construct an elementary theory of blower, one-dimensional flow is assumed. The idealised fluid-velocity vectors, generally known as the velocity diagrams, through the impeller are combined with the angular-momentum theorem for a control volume. The idealised velocity diagrams at the inlet and exit of a blower rotor are shown in Figure 2.8. The simplified vector-diagram analysis assumes that the flow leaves the blade row at a relative velocity exactly parallel to the exit blade angle.

There are three different velocities in the velocity diagrams, namely:

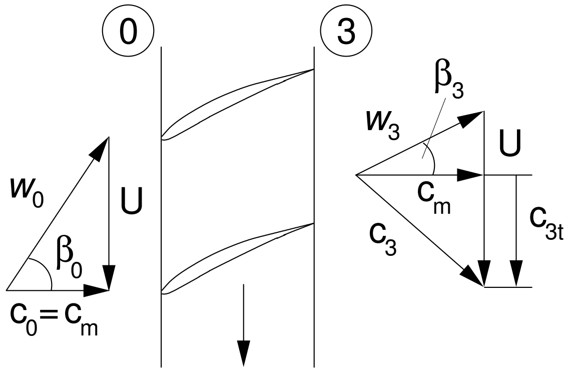

Figure 2.8: Inlet and exit velocity diagrams

- Absolute velocity c $[\frac{m}{s}]$
- Circumferential/Rotor speed U $[\frac{m}{s}]$
- Relative velocity w $[\frac{m}{s}]$

The main equation for a turbomachine is obtained by applying the angular momentum theorem on the rotor and is known as the Euler turbomachine equation:

$$M_{rotor} = \dot{m} \cdot (r_3 \cdot c_{3t} - r_0 \cdot c_{0t}) \tag{2.27}$$

where,

- M_{rotor} : rate of change of angular momentum (force moment) $[N \cdot m]$
- $\dot{m}$: mass flow rate $[\frac{kg}{s}]$
- r : cross-sectional radius $[m]$

The subscript t stands for the tangential or the peripheral component of the flow velocity.

From the geometry of the velocity diagrams, since there is no radial flow, the inlet c_0 and exit rotor velocities c_m are equal; one-dimensional continuity requires that the axial-velocity component remain constant. Thus at inlet:

$$c_0 = c_m = \frac{Q}{\pi \cdot (r_{0c}^2 - r_{0h}^2)} = \text{constant} \tag{2.28}$$

The indices $0h$ and $0c$ correspond to the hub and casing at the inlet, respectively.

$$U(r) = 2 \cdot \pi \cdot N \cdot r \tag{2.29}$$

$$tan(\beta_0) = \frac{U}{c_m} \tag{2.30}$$

Similarly at outlet, for a non-swirling flow, the velocity diagram gives the relation:

$$c_{3t} = \frac{g \cdot H}{U \cdot \eta_H} \tag{2.31}$$

Here,

- Q : volumetric flow rate $[\frac{m^3}{s}]$
- N : rotational speed $[rpm]$
- β_0 : inlet velocity angle $[°]$
- g : gravitational acceleration $[\frac{m}{s^2}]$
- η_H : hydraulic efficiency
- H : hydraulic head$[m]$

The angle between the axial and relative velocity at outlet can be calculated from:

$$tan(\beta_3) = \frac{U - c_{3t}}{c_m} \tag{2.32}$$

2.7 Dimensionless Characteristics

Performance of a turbomachine can be described by several independent variables:

- Volumetric flowrate (Q)
- Pressure head (Energy per unit weight, H)
- Characteristic dimension (D)
- Power (P)
- Density and viscosity of the working fluid (ρ, μ)
- Rotational speed of the impeller (N)

These parameters are interrelated with each other in terms of non-dimensional terms. For similar turbomachines, these non-dimensional terms are constant for different operating conditions. The commonly defined dimensionless numbers include flow coefficient (ϕ), pressure rise coefficient (Ψ), power coefficient (ξ), efficiency (η) and Reynolds number (Re). Mathematically;

$$\text{Flow Coefficient, } \phi = \frac{\text{Actual Volumetric Flowrate}}{\text{Theoretical Volumetric Flowrate}} = \frac{Q}{\pi \cdot U \cdot r^2} \tag{2.33}$$

$$\text{Pressure Rise Coefficient, } \Psi = \frac{\text{Pressure Force}}{\text{Inertial Force}} = \frac{\Delta P_s}{\frac{1}{2} \cdot \rho \cdot U^2} \tag{2.34}$$

$$\text{Power Coefficient, } \xi = \frac{\text{Shaft Power}}{\text{Available Power}} = \frac{P}{\frac{1}{2} \cdot \rho \cdot A \cdot U^3} \tag{2.35}$$

2.7.1 Reynold's Number

In the flow of a fluid through a completely filled conduit, gravity does not affect the flow pattern. It is also obvious that capillarity is of no practical importance, and hence the significant forces are inertia and fluid friction due to viscosity. Considering the ratio of inertia forces to viscosity forces, the parameter obtained is called the *Reynolds number*, *Re*. It is generally accepted as the most important parameter in fluid mechanics and is named after Osborne Reynolds, who first proposed it.

$$Re = \frac{\text{Inertial Force}}{\text{Viscous Force}} = \frac{\rho \cdot U_{char} \cdot L_{char}}{\mu} \tag{2.36}$$

where,

- U_{char} : characteristic speed $[\frac{m}{s}]$
- L_{char} : characteristic length $[m]$
- μ : dynamic viscosity of fluid $[\frac{kg}{m \cdot s}]$
- ρ : density of fluid $[\frac{kg}{m^3}]$

For any consistent system of units, *Re* is a dimensionless number. The Reynolds number is always important, with or without a free surface, and can be neglected only in flow regions away from high-velocity gradients, e.g., away from solid surfaces, jets, or wakes.

2.7.2 Dimensionless Fundamental Equations

For a viscous incompressible fluid moving under the influence of gravity, the differential form of the continuity equation and the RANS equations in a Cartesian coordinate system can be cast, using tensor notation, in the form,

$$\frac{\partial \overline{u}_i}{\partial x_i} = 0, \tag{2.37}$$

$$\rho \cdot \left(\frac{\partial \overline{u}_i}{\partial t} + \overline{u}_j \cdot \frac{\partial \overline{u}_i}{\partial x_j} \right) = -\frac{\partial \overline{p}}{\partial x_i} + \frac{\partial}{\partial x_j} \left(\mu \cdot \frac{\partial \overline{u}_i}{\partial x_j} - \rho \cdot \overline{u'_i \cdot u'_j} \right) \tag{2.38}$$

for $i = 1, 2, 3$ and $j = 1, 2, 3$.

For the implementation in a computer code to perform numerical simulations, it is more convenient to use a dimensionless form of the equation which is obtained by dividing all lengths by the characteristic length L_{char} and all velocities by the free stream characteristic velocity U_{char}. Thus the dimensionless form of the RANS becomes:

$$\left(\frac{\partial \overline{u}_i}{\partial t} + \overline{u}_j \cdot \frac{\partial \overline{u}_i}{\partial x_j} \right) = -\frac{\partial \overline{p}}{\partial x_i} + \frac{1}{Re_{L_{char}}} \cdot \frac{\partial^2 \overline{u}_i}{\partial x_j \partial x_j} - \frac{\partial \overline{u'_i \cdot u'_j}^{\,*}}{\partial x_j} \tag{2.39}$$

where $\overline{u'_i \cdot u'_j}^{\,*}$ is a dimensionless form of the Reynolds stress.

Chapter 3

Numerical Fundamentals

The numerical flow field simulation for the axial blower is carried out using a commercial CFD software package FLUENT®, a product of ANSYS®, Inc.

Analytical solutions to the Navier Stokes equations exist for only the simplest of flows under ideal conditions. The fundamental equations of fluid mechanics (Eqs. 2.2, 2.16-2.18) mentioned in section 2.3 represent a system of partial differential equations of first order linear and second order nonlinear in time and space coordinates respectively. These governing equations are quite complicated and cannot be solved analytically for an exact solution. To obtain solutions for such system of equations, a numerical approach has to be adopted.

FLUENT® offers the users to choose one of the two numerical methods:

- Pressure-Based Solver
- Density-Based-Solver

In both methods the velocity field is obtained from the momentum equations. In the density-based approach, the continuity equation is used to obtain the density field while the pressure field is determined from the equation of state. On the other hand, in the pressure-based approach, the pressure field is extracted by solving a pressure or pressure correction equation which is obtained by manipulating continuity and momentum equations. For the current work, Pressure-Based-Solver is adopted.

In both solvers, numerical computational techniques are used to replace the governing partial differential equations with system of algebraic equations that can be solved using a computer. The technique of converting the continuous governing partial differential equations into a system of algebraic equations is known as *discretisation* [45]. Analytical solutions of partial differential equations involve closed-form expressions which give the variation of the dependent variables *continuously* throughout the domain. In contrast, numerical solutions can give answers at only *discrete points* in the domain, called *grid points* [7, 37]. Thus the accuracy of a CFD solution is governed by the number of cells in the grid. In general, the larger the number of cells, the better will be the solution accuracy. The algebraic equations are solved through suitable algorithms and the approximate values for the dependent flow field variables are obtained at discrete points in time and/or space. The success or failure of such algorithms can be determined by observing the properties like; *stability*, *convergence* and *consistency*.

3.1 Discretisation Methods

There are different methods of numerical solution techniques to discretise the complex partial differential equations. Some of the well-known and most important discretisation methods being used are:

- Finite Difference Method (FDM),
- Finite Volume Method (FVM),
- Finite Element Method (FEM).

Other methods, like spectral schemes, boundary element methods, and cellular automata are used in CFD but their use is limited to special classes of problems [25]. Each type of method yields the same solution if the grid is very fine. However, some methods are more suitable to some classes of problems than others.

FLUENT® uses a control-volume-based technique to convert a general scalar transport equation to an algebraic equation that can be solved numerically. This control volume technique consists of integrating the transport equation (Eq. 3.1) about each control volume, yielding a discrete equation that expresses the conservation law on a control-volume basis. The approach has the merit, amongst others, of ensuring that the discretised forms preserve the conservation properties of the parent differential equations. The FVM can accommodate any type of grid, so it is suitable for complex geometries. The transport equation for a general variable ϕ can be written in the following form:

$$\frac{\partial(\rho\phi)}{\partial t} + div(\rho\phi\vec{\boldsymbol{v}}) = div(\Gamma_\phi \; grad \; \phi) + S_\phi \tag{3.1}$$

where,

- ϕ : any of the dependent variables as u, v, w etc.
- $\vec{\boldsymbol{v}}$: fluid velocity vector
- Γ_ϕ : diffusion coefficient
- S_ϕ : total source term, source of ϕ per unit volume

The equation 3.1 is used as the starting point for computational procedures in the finite volume method. The key step of FVM is the integration of Eq. 3.1 over a three-dimensional control volume $\boldsymbol{V}$ which yields into the following equation:

$$\int\limits_V \frac{\partial(\rho\phi)}{\partial t} dV + \int\limits_V div(\rho\phi\vec{\boldsymbol{v}})dV = \int\limits_V div(\Gamma_\phi \; grad \; \phi)dV + \int\limits_V S_\phi dV \tag{3.2}$$

The volume integrals of the convective and diffusive terms can be re-written as integrals over the entire bounding surface of the control volume by using Gauss' divergence theorem [45]. The theorem states that for a vector $\vec{\boldsymbol{F}}$:

$$\int_V (div(\vec{\boldsymbol{F}})) \cdot dV = \int_A (\vec{\boldsymbol{F}} \cdot \vec{\boldsymbol{n}}) \cdot dA \tag{3.3}$$

For control volumes that do not deform in time, the time derivatives can be moved outside of the volume integrals. Applying Gauss' divergence theorem, equation 3.2 can be simplified as follows:

$$\frac{\partial}{\partial t}\int_V (\rho \cdot \phi)\, dV + \int_A (\rho \cdot \phi \cdot \vec{\boldsymbol{v}}) d\vec{\boldsymbol{A}} = \int_A (\Gamma_\phi \ grad\ \phi) d\vec{\boldsymbol{A}} + \int_V S_\phi dV \tag{3.4}$$

with $\vec{\boldsymbol{A}}$ being the surface area vector of the control volume $\boldsymbol{V}$.

Equation 3.4 is applied to each control volume, or cell, in the computational domain. For a computational cell of volume V with discrete faces $A_f (f = 1, N_f)$, the equation becomes:

$$\frac{d}{dt}\int_V (\rho \cdot \phi)\, dV + \sum_f \oint_{A_f} (\rho_f \cdot \phi_f \cdot \vec{\boldsymbol{v}}_f) d\vec{\boldsymbol{A}}_f = \sum_f \oint_{A_f} (\Gamma_\phi \ grad\ \phi_f) d\vec{\boldsymbol{A}}_f + \int_{V_f} S_\phi dV \tag{3.5}$$

where,

- $\vec{\boldsymbol{A}}_f$: surface area vector of face f
- ϕ_f: value of ϕ convected through f
- N_f: number of faces enclosing cell

Equation 3.5 is the general formulation of the finite volume method and states the conservation of a fluid property for a finite size (macroscopic) control volume. It indicates that the time variation of conserved quantities inside a control volume is equal to the sum of the fluxes (convective, diffusive) exchanged between neighbouring cells, thus guaranteeing global conservation.

The basic idea of a finite-volume method is to satisfy the integral form of the conservation law to some degree of approximation for each of many contiguous control volumes which cover the domain of interest. Thus the shape of cell volume is dependent on the nature of the grid. The variables are considered as spatially fixed for each cell volume, which leads 3.5 to a system of ordinary differential equations with respect to time, and ultimately through an integration scheme in time, an algebraic system for the unknowns at a given time level is achieved. The equations can be solved through different available methods. In order to evaluate gradients (and hence fluxes) at the control volume faces an approximate distribution of properties between nodal points is used. It is done by defining cell-averaged flow variable values for each control volume.

From here onwards, approximations for the surface and volume integral terms have to be considered so as to obtain an algebraic equation for a particular control volume. The major difference between the space and time coordinates lies in the direction of influence: whereas a force at any space location may influence the flow anywhere else, forcing at a given instant will affect the flow only in the future − there is no backward influence [25].

3.1.1 Time Discretisation

For physical time-dependent problems, such as those associated with transient flow behaviour or those connected to time-varying boundary conditions, a time-dependent mathematical model is to be used. Thus the governing equations must be discretised in both space and time. Temporal discretisation involves the integration of every term in the differential equations over a time step Δt. The time derivative term representing the rate of increase of *phi* in equation 3.5 is discretised to approximate the value of *phi* at discrete time steps.

An arbitrary point can be generalised in time coordinate as:

$$t^n = n \cdot \Delta t \tag{3.6}$$

where Δt represents the default time interval and n is the number of intervals.

The purpose of discretisation of time derivatives is to compute the unknown variable ϕ at a new time level, t^{n+1}. A generic expression for the time evolution of variable ϕ is given by:

$$\frac{\partial \phi}{\partial t} = F(\phi) \tag{3.7}$$

where the function F incorporates any spatial discretisation. If the time derivative is discretised using backward differences, the first-order accurate temporal discretisation results:

$$\frac{\phi^{n+1} - \phi^n}{\Delta t} = F(\phi) \tag{3.8}$$

and the second-order discretisation gives:

$$\frac{3\phi^{n+1} - 4\phi^n + \phi^{n-1}}{2\Delta t} = F(\phi) \tag{3.9}$$

where,

- ϕ^{n+1}: value at the next time level, $t + \Delta t$
- ϕ^n: value at the current time level, t
- ϕ^{n-1}: value at the previous time level, $t - \Delta t$

There are two very common methods of temporal discretisation in CFD applications, namely the *explicit* and *implicit* methods.

3.1.1.1 Explicit Euler Method

In an explicit temporal discretisation, each nodal value at the new (i.e. unknown) time-level is given explicitly in terms of known nodal values (i.e. those at previous time-levels and boundary conditions). Explicit methods (also known as Euler-Forward-Method) tend to be relatively cheaper per time-step since no matrix inversion is required and thus simple to program. However, these methods are not necessarily stable, which means that the time-step Δt cannot be chosen arbitrarily. The basic temporal discretisation can be expressed as:

$$\frac{\partial \phi}{\partial t} \approx \frac{\phi^{n+1} - \phi^{n}}{\Delta t} = F(\phi^{n}) \tag{3.10}$$

and is referred to as "explicit" integration since ϕ^{n+1} can be expressed explicitly in terms of the existing solution values, ϕ^{n}.

Explicit methods are conditionally stable in time. The use of explicit time stepping is fairly restrictive. In FLUENT®, the explicit time stepping formulation is available only with the coupled explicit solver.

3.1.1.2 Implicit Euler Method

In an implicit temporal discretisation, each nodal value at the new time-level depends implicitly on other (unknown) nodal values at the new time-level, as well as on known values from previous time-levels and boundary conditions (hence a matrix system must be solved to determine these implicit values). The method evaluates $F(\phi)$ at the future time level as:

$$\frac{\partial \phi}{\partial t} \approx \frac{\phi^{n+1} - \phi^{n}}{\Delta t} = F(\phi^{n+1}) \tag{3.11}$$

The method, also known as the Euler-Backward-Method, relates the ϕ^{n+1} in a given cell to ϕ^{n+1} in neighbouring cells through $F(\phi^{n+1})$. This implicit equation can be solved iteratively at each time level before moving to the next time step. The advantage of the fully implicit method is that it is unconditionally stable with respect to time step size.

3.1.2 Space Discretisation

Space discretisation involves the discretisation of surface and volume integrals of the flow governing equations in space coordinates, x, y and z at constant time level.

The approximations to the integrals require the values of variables at locations other than the computational nodes (control volume centres). To calculate the convective and diffusive fluxes, the value of ϕ and its gradient normal to the cell face at one or more locations on the control volume surface are needed. Volume integrals of the source terms may also require these values. They have to be expressed in terms of the nodal values by interpolation.

FLUENT® stores discrete values of the variable ϕ at the cell centres. However, as already described, face values ϕ_f are required for the convection terms in and must be interpolated from the cell centre values. This is accomplished using an upwind scheme. Upwinding means that the face value ϕ_f is derived from quantities in the cell upstream, or "upwind", relative to the direction of the normal velocity v_n. FLUENT® allows to choose from several upwind schemes: first-order upwind, second-order upwind, power law, and QUICK. The diffusion terms are central-differenced and are always second-order accurate [4].

For the current research work, the second order upwind scheme has been used to calculate the necessary flow variable values at cell boundaries from the known values at computational cell centres. The use of a particular interpolation scheme for a given computational grid is usually a compromise between numerical stability and accuracy.

3.1.2.1 Second-Order Upwind Scheme

The scheme is used to achieve the second-order accuracy. Quantities at cell faces are computed using a multidimensional linear reconstruction approach. In this approach, higher-order accuracy is achieved at cell faces through a Taylor series expansion of the cell-centred solution about the cell centroid. Thus when second-order upwinding is selected, the face value ϕ_f is computed using the following expression:

$$\phi_{f,SOU} = \phi + \nabla\phi \cdot \vec{r} \tag{3.12}$$

where ϕ and $\nabla\phi$ are the cell-centred value and its gradient in the upstream cell, and $\vec{r}$ is the displacement vector from the upstream cell centroid to the face centroid. This formulation requires the determination of the gradient $\nabla\phi$ in each cell. Green-Gauss Node-Based method is used in this work to compute the gradient. Finally, the gradient $\nabla\phi$ is limited so that no new maxima or minima are introduced.

The final form of the discrete finite volume equation is obtained by substituting the various approximated terms back into equation 3.5 and then invoking the discretised continuity equation, which can be written as:

$$\frac{(\rho \cdot V)^n - (\rho \cdot V)^{n-1}}{\delta t} + \sum_f J_f \cdot A_f = 0 \tag{3.13}$$

where J_f is the mass flux (ρv_n) through face f.

The ultimate result, in its most compact form, is:

$$a_P\phi_P = \sum_{nb} a_{nb}\phi_{nb} + S + b_P\phi_P \tag{3.14}$$

where the subscript nb refers to neighbour cells. Also,

- $a_P \equiv \sum\limits_{nb} a_{nb} + S_P + b_P$; linearised coefficient for ϕ_P
- a_{nb}: linearised coefficient for ϕ_{nb} representing the effects of convection and/or diffusion
- $b_P \equiv \dfrac{(\rho \cdot V)}{\delta t}$

The equation 3.14 or its suitably modified form, where necessary, exists for every computational cell. There are as many such equation sets as dependent variables, when the continuity equation is taken into account.

The solution strategy in FLUENT® involves iterative solution of these sets. The pressure-based solver uses an implicit discretisation of the transport equation 3.5. As a standard default approach; all convective, diffusive, and source terms are evaluated from the fields for time level ‘n+1’ [4].

3.2 Implementation of Boundary Conditions

The equations relating to fluid flow can be closed (numerically) by the specification of conditions on the external boundaries of a domain. It is the boundary conditions that produce different solutions for a given geometry and set of physical models. Hence boundary conditions determine to a large extent the desired characteristics of the solution. Therefore, it is important to set boundary conditions that accurately reflect the real situation to obtain accurate results.

The type of Boundary Conditions that can be set depends upon what sort of boundary or interface the Boundary Condition is placed on. FLUENT® has a wide range of boundary conditions that cover the majority of practical situations. The boundary conditions applied for this work will only be described briefly in the following sections:

Velocity Inlet Boundary Conditions

Velocity inlet boundary condition is used to define the flow velocity, along with all relevant scalar properties of the flow, at flow inlets. The total (or stagnation) properties of the flow are not fixed, so they will rise to whatever value is necessary to provide the prescribed velocity distribution. This boundary condition is intended for incompressible flows, and its use in compressible flows will lead to a non-physical result [4].

Several options exist for the specification of turbulence quantities at inlets. For fully-developed internal flows, flows downstream of turning vanes, etc., the Intensity and Hydraulic Diameter method is recommended. The turbulence intensity, I, is defined as the ratio of the root-mean-square of the velocity fluctuations, u', to the mean flow velocity, u_{avg}. Nominal turbulence intensities range from 1% to 5% but depends on the specific application. The turbulence intensity at the core of a fully-developed duct flow can be estimated from the following formula derived from an empirical correlation for pipe flows:

$$I \equiv \frac{u'}{u_{\text{avg}}} = 0.16(\text{Re}_{D_H})^{-1/8} \tag{3.15}$$

Outflow Boundary Condition

Outflow boundary conditions are used to model flow exits where the details of the flow velocity and pressure are not known prior to solution of the flow problem. FLUENT® extrapolates the required information from the interior. The outflow boundary condition is also intended for incompressible flows.

The boundary conditions used by FLUENT® at outflow boundaries are as follows:

- A zero diffusion flux for all flow variables
- An overall mass balance correction

Wall Boundary Condition

Walls are solid (impermeable) boundaries to fluid flow. Wall boundary conditions are used to bound fluid and solid regions. In viscous flows, the no-slip boundary condition is enforced at walls by default. The no-slip condition indicates that the fluid sticks to the wall and moves with the same velocity as the wall, if it is moving, i.e. $u_i = u_{i,wall}$. A tangential velocity component in terms of the translational or rotational motion of the wall boundary can also be specified, which is also the case in this work.

Fluid Condition

A fluid zone is a group of cells for which all active equations are solved. The only required input for a fluid zone is the type of fluid material. The motion for the fluid zone can also be defined alongwith the direction of rotation axis.

3.3 Solution Algorithm

Discretisation yields a large system of non-linear coupled algebraic equations. The method of solution depends on the problem. Steady problems are usually solved by iteration schemes. These methods use successive linearisation of the equations and the resulting linear systems are almost always solved by iterative techniques. Two pressure-based solver algorithms are available in FLUENT®:

- **The Pressure-Based Coupled Solver**
  It solves a coupled system of equations comprising the momentum equations and the pressure-based continuity equation. However, the remaining equations (for additional scalars such as turbulent quantities) are solved in a decoupled fashion. There is a significant improvement in the rate of solution convergence but the memory requirement increases by 1.5-2 times than that required by the segregated algorithm.

- **The Pressure-Based Segregated Solver**
  The pressure-based solver uses a solution algorithm where the governing equations are solved sequentially (i.e., segregated from one another). As the governing equations are non-linear and coupled, the solution loop must be carried out iteratively in order to obtain a converged numerical solution. In the segregated algorithm, the individual governing equations for the solution variables (e.g., u, v, w, p, k, ω, etc.) are solved one after another. The method is applied in this current work.

Solution of the Navier-Stokes equations (Section 2.3.2) is complicated by the lack of an independent equation for the pressure, whose gradient contributes to each of three momentum equations. Furthermore, the continuity equation does not have a dominant variable in incompressible flows. Mass conservation is a kinematic constraint on the velocity field rather than a dynamic equation [25]. It is important to note that the absolute pressure is of no significance in an incompressible flow; only the gradient of the pressure (pressure difference) affects the flow.

In compressible flows the continuity equation can be used to determine the density and the pressure is calculated from an equation of state. The approach is not appropriate for incompressible or low Mach number flows. In such cases coupling between pressure and velocity introduces a constraint on the solution of the flow field: if the correct pressure field is applied in the momentum equations the resulting velocity field should satisfy continuity [88].

The problems associated with the non-linearities in the equations set and the pressure-velocity linkage can be resolved by adopting an iterative solution strategy. FLUENT® provides the option to choose among five pressure-velocity coupling algorithms, namely SIMPLE, SIMPLEC, PISO, Coupled, and for unsteady flows, Fractional Step (FSM). SIMPLE, SIMPLEC, PISO, and Fractional Step use the pressure-based segregated algorithm and are based on predictor-corrector approach, while “Coupled” algorithm uses the pressure-based coupled solver. For the current work, SIMPLE-Algorithm (Semi-Implicit Method for Pressure-Linked Equations) is adopted.

3.3.1 SIMPLE-Algorithm

The SIMPLE algorithm uses a relationship between velocity and pressure corrections to enforce mass conservation and to obtain the pressure field. To initiate the SIMPLE calculation process, the discretised momentum equations are solved with a guessed pressure field p^* to yield velocity components u^*, v^* and w^*. However, the resulting face flux, J_f^*, does not satisfy the continuity equation. Consequently, the corrections p' and J_f' are added to the guessed pressure field p^* and face flux J_f^*, respectively, so that the corrected face flux, J_f, satisfies the continuity equation:

$$p = p^* + p', \qquad J_f = J_f^* + J_f' \tag{3.16}$$

The discrete pressure-correction equation (3.17) may be solved using the algebraic multi-grid (AMG) method.

$$a_P \; p' = \sum_{\text{nb}} a_{\text{nb}} \; p'_{\text{nb}} + b \tag{3.17}$$

The corrected face flux, J_f, satisfies the discrete continuity equation identically during each iteration. Once a solution is obtained, the cell pressure is corrected using:

$$p = p^* + \alpha_p \; p' \tag{3.18}$$

Here α_p is the under-relaxation factor for pressure. The pressure correcting equation is susceptible to divergence unless this under-relaxation factor is used during the iterative process. A correct choice of under-relaxation factor α is essential for cost- effective simulations. The optimum values of under-relaxation factors are flow dependent.

Part II

Numerical Modelling

Chapter 4

Verification and Validation

Computational fluid dynamics makes use of computer simulations to obtain an approximate solution of the governing equations of fluid flow. The solution is always approximate because only discretised versions of the continuum transport equations for fluid flow and energy transfer can be solved numerically. Moreover, in turbulent flows, the effects of turbulence cannot be represented in a mathematically accurate sense, but are modelled by approximate theories [13].

Verification and validation are the two main principles that are necessary for assessing the credibility of modeling and simulation in computational fluid dynamics. It is very useful to make some clear distinctions between the meanings of these terms as both contribute to the overall accuracy of a numerical simulation.

4.1 Verification

Verification is the first step of the validation process. It is the process of determining that a computational simulation accurately represents the conceptual model without taking the real conditions into account. Thus it is a procedure to ensure only that the program solves the equations correctly.

In essence, verification provides evidence that the model is solved correctly but it does not address whether the model has any relationship to the real world. Verification activities only evaluate whether the CFD model, the mathematical and computer code representation of the physical system, is solved accurately [2].

4.2 Validation

Validation addresses the question of the accuracy of the model to specific conditions of the real world [2]. It is achieved by systematically comparing the results of computational solution with experimental data. In other words, validation is the procedure to test the suitability of the numerical and physical models for the particular computational simulation or analysis.

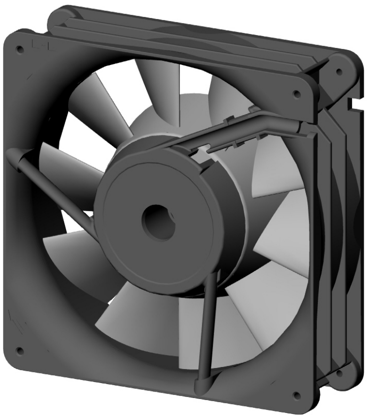

Figure 4.1: Original Axial Flow Blower

Flow Rate **Q, m^3/hr**	**Static Pressure** **P_s, Pa**	**Efficiency** **η, %**
0.00	173.30	0.00
29.81	149.90	7.12
68.16	124.50	13.70
100.60	96.28	16.84
128.00	91.61	20.27
161.60	93.54	24.45
198.20	87.24	27.49
231.00	62.96	23.14
264.40	27.58	11.99
294.10	0.00	0.00

Table 4.1: Experimental Data

4.3 Validation Case

In this research work, the validation of a single stage axial blower is carried out. The axial blower under consideration is MF 127 made by PMDM, shown in Figure 4.1. The blower is being used for the cooling of the main casings of network servers and in the telecommunication industry.

The experimental data (Δ p vs. Q curve) for the validation of this axial blower is available from the vendor and is given in Table 4.1. The efficiency η is defined in Section 6.2.1 as Equation 6.1.

The operating point at maximum efficiency i.e. the best efficiency point (BEP) is used as the reference for validation. Figure 4.2 shows the experimentally obtained performance curves of the axial blower and the best efficiency point marked on it.

The uncertainty in the experimental data cannot be given, as the exact experimental

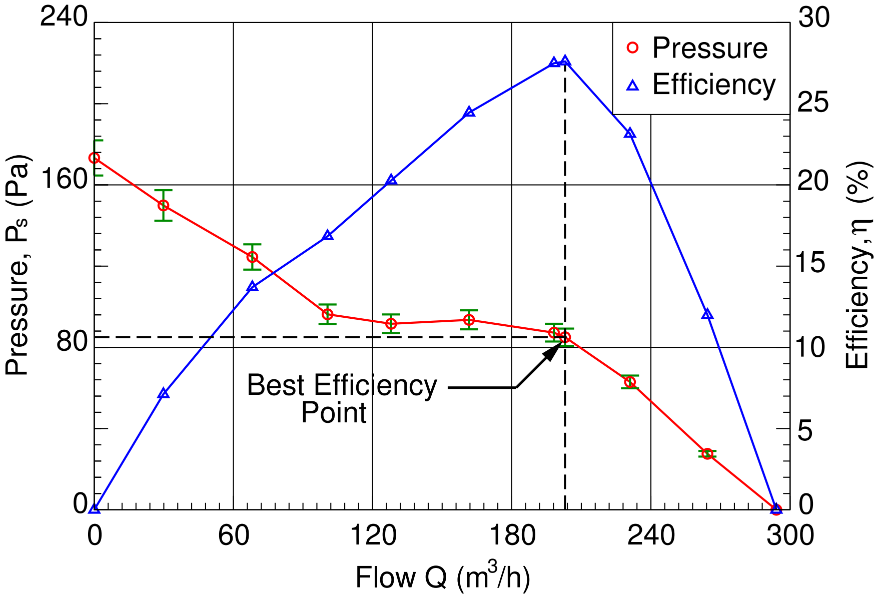

Figure 4.2: Performance Curves, Experimental Data (*Courtesy PMDM*)

details are not available from PMDM. The error in the experimental data is therefore estimated on the basis of literature for such standard experiments. BS Standard 848 quotes an uncertainty of ±2% for all measurements of fan flow carried out in accordance with the standard. The overall error for pressure measurement in such fan performance experiments is observed to be 3 to 4% [51, 58, 85]. Thus an error of ±5% has been estimated for the available experimental data.

4.4 Numerical Model

The preliminary work for the sweep study of an axial blower is started with the validation process. The numerical flow field is validated using a 3D flow solver (FLUENT®) by comparing the numerical and experimental data. It is ensured that the proposed model represents the actual flow field.

The grid generation and computational simulation for the validation is carried out by creating a validation model setup. The setup is based on a typical "test facility". The facility is used for testing and analysing the performance of axial blowers at different pressures and flow rates. A schematic of such a test facility is shown in Figure 4.3.

Keeping the test facility in view, a computational setup is required as shown in Figure 4.4. The main idea is to achieve the constant pressure conditions on the inlet and outlet of the control volume during the flow simulation. The sizes assumed for the control volume should be large enough so that the influence of surroundings on the flow is minimised.

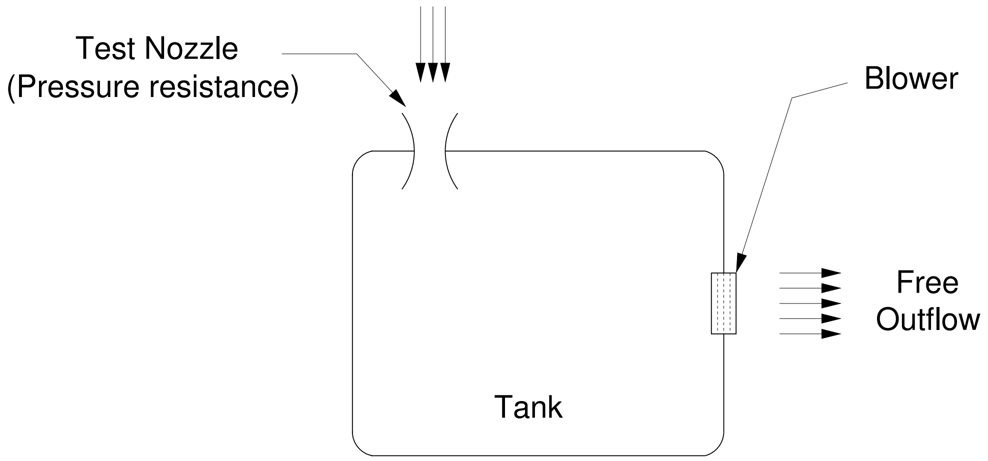

Figure 4.3: Typical Blower Test Facility

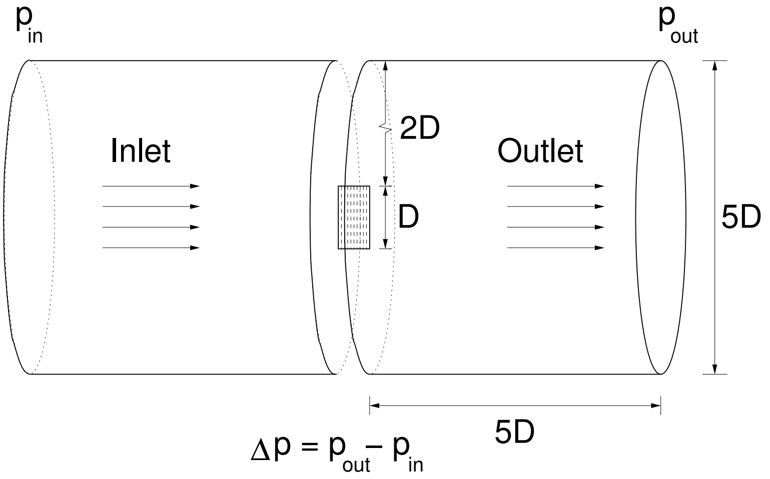

Figure 4.4: Validation Setup

4.4.1 CAD Model Setup

The setup of the model for the validation process is initiated by modifying the available non-assembled CAD drawings of the axial blower. The original drawings from the vendor consist of the rotor assembly and the housing of the blower. The drawings are in IGES/STEP format and are shown in Figure 4.5. The CAD geometries are imported to a CAD software, Rhinoceros®. They are then simplified by removing some of the extra parts like mounting fixtures, hub inner supports and cable structures. The geometry simplification is done to avoid complications in the grid generation and thus to save computational time while running flow simulations.

The simplified geometries are then combined and aligned, Figure 4.6. A control volume is built around the simplified geometry of the axial blower, approximately as per the dimensional ratios shown in the validation setup (Figure 4.4). Here 'D' is the average

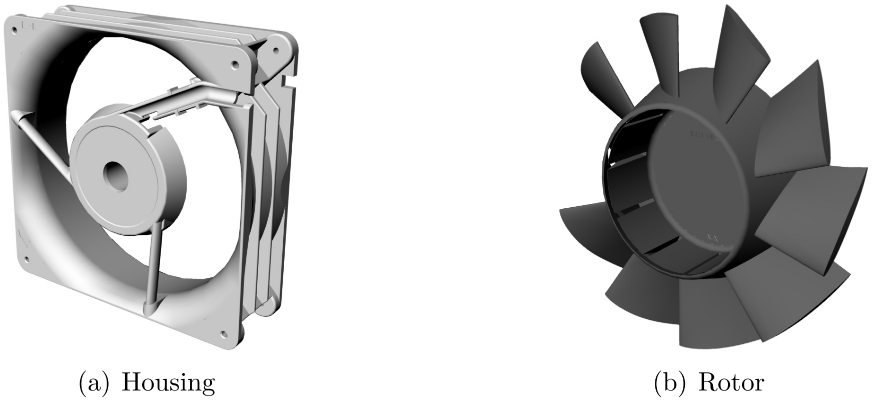
(a) Housing (b) Rotor

Figure 4.5: Original Geometry of Axial Blower

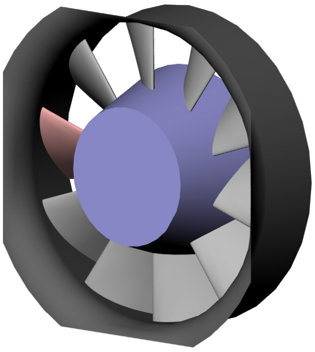
Figure 4.6: Simplified Geometry: Blower Assembly

diameter of the casing and measures 117.88 mm. The whole assembly is made *water-tight* fluid volume by making minor changes without effecting the main blower assembly.

4.5 Grid Generation

Two different approaches are used for the grid generation and thus for the numerical simulation of the validation model. Initially a full assembly setup, Figure 4.7(a), is taken as the validation case. The results obtained from this setup using unstructured hybrid mesh were not satisfactory and thus led to the second approach of passage to passage setup with single blade, Figure 4.7(b), using unstructured hexahedral mesh.

4.5.1 Full-Assembly Setup

The finalised full CAD model is imported in ANSYS® ICEM CFD™ software as an IGES/STEP file for grid generation. The geometry is first checked for any type of errors and leaks. The geometry is then subdivided into different parts so as to assign suitable mesh parameters for each part. Initially a series of attempts were made to generate the

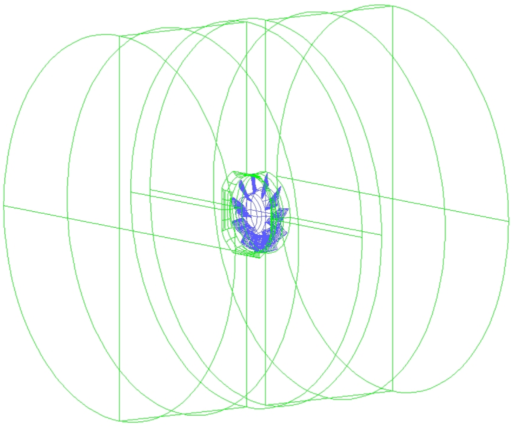

(a) Full-Assembly CAD Model

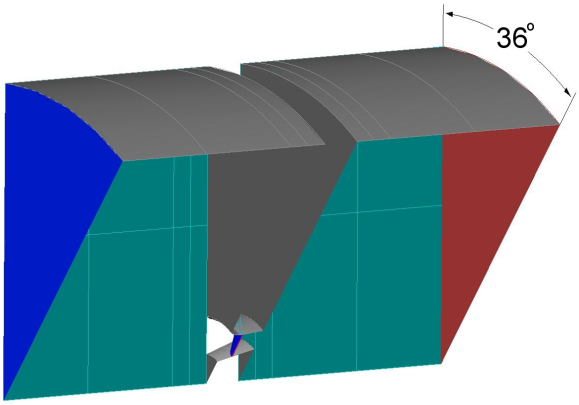

(b) Single Blade: Passage-to-Passage Setup

Figure 4.7: CAD Model Setups

grid for rotor and housing portion being the critical and most concerned area. Material body 'LIVE' is created for this portion.

Unstructured tetrahedral meshing technique is chosen for this region as it is suitable for complex geometries like rotor and housing in this case. The mesh can be directly generated from CAD or STL surfaces. Curvature/Proximity Based Refinement characteristic automatically determines tetrahedral size for individual geometry features. The tetra mesh can be merged with another tetra-, hexa- or hybrid mesh and then can be smoothed. Extrusion of Prism layers from the surface mesh for boundary layer calculations is possible in this technique.

Prism layers are used close to the wall regions of housing and also for all the rotating parts. The grid is optimised so that there is a sufficient number of grid cells for flow simulation, keeping the grid quality in acceptable range.

The grid generation for the remaining volume is carried out after achieving a good quality grid for rotor and housing. The grid is divided in three fluid domains, one LIVE and two FLUID zones. These domains will serve in the flow solver as different frames of reference

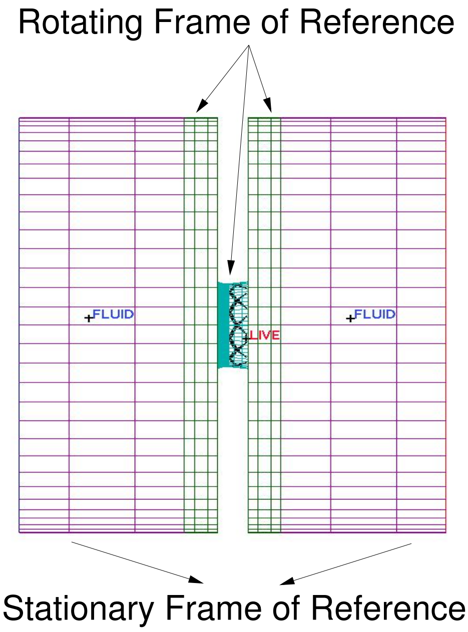

Figure 4.8: Fluid Domains and Multiple Frames of Reference

so that the technique of multiple reference frames can be applied in the CFD solver for the simulation. Figure 4.8 shows the three fluid domains and the frames of reference defined for the solver setup. The LIVE region consists of both tetrahedral and prism cells while O-grid (Hexahedral) is generated in the outer cylindrical areas of both sides of the validation model. The body-fitted internal O-grids are useful for creating good quality meshes. The tetra/prism mesh is then merged with the hexa mesh and checked for any errors. The combined hybrid mesh is smoothed to achieve the best possible quality. The hybrid grid and its sectioned view are given in Figure 4.9.

4.5.1.1 Mesh Data

Several attempts are made to attain a better grid for the simulation. The general tetra/prism mesh parameters and the mesh sizes finally defined for different parts are given below:

General Parameters

• Scale Factor:	15
• Maximum Tetra Size:	08
• Refinement for the gaps:	0.01
• Prism Layer Parameters:	
Boundary Layer Thickness (Estimated):	0.90 mm
Viscous Sub-layer Thickness (Estimated):	0.10 mm
Prism Layer Thickness for blade:	0.07 mm
• Number of Prism Layers:	03

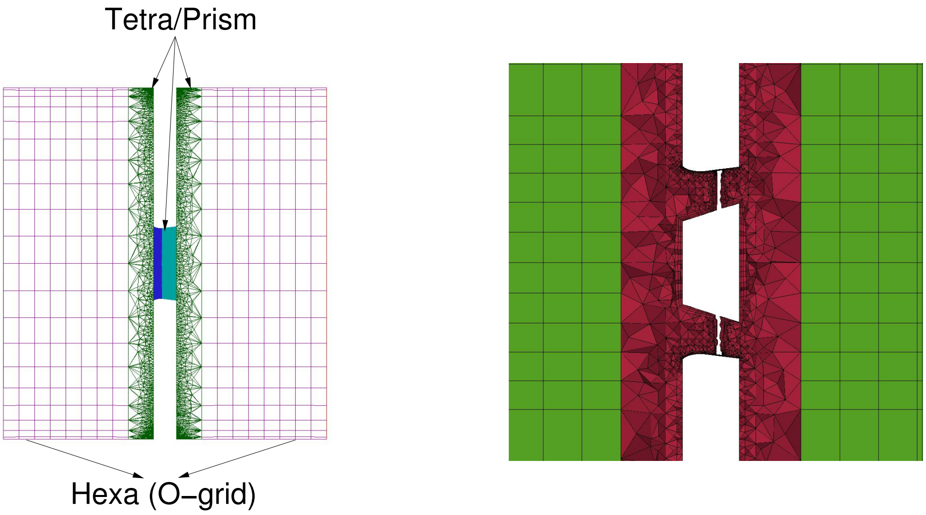

Figure 4.9: Hybrid Grid and Cut-Plane Section

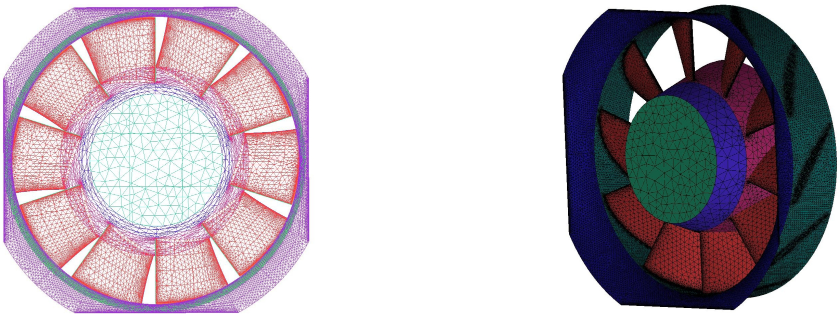

Figure 4.10: Surface Mesh, Rotor/Casing Assembly

The number of prism layers are subject to vary for grid independence and for fulfilling the requirements of different turbulence models. Figure 4.10 shows the surface mesh of the rotor/casing assembly while hub and blade prism layers are shown in Figure 4.11.

The total number of cells in the finally achieved hybrid grid is 2.38 Million. The worst tetra cells have the minimum quality of 0.87, which is within an acceptable range of standard flow solvers. The mesh quality can be viewed in Figure 4.12.

4.5.2 Passage-to-Passage Setup

Passage-to-Passage single blade setup is adopted as a second approach for the numerical computation. The mesh is created using GAMBIT® turbo operations which allows to model flow scenarios that involve turbomachinery components such as fans or turbochargers. The purpose of such operations is to create and mesh a turbo volume — that is, a model composed of one or more real volumes that together represent the flow environment in the region surrounding an individual turbomachinery blade. The turbo volume includes boundaries that represent the hub, casing, inlet, outlet, and blade.

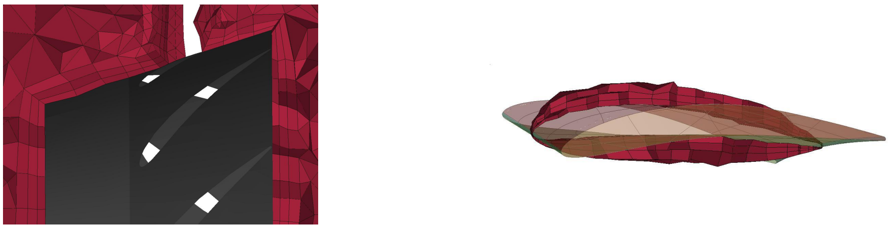

Figure 4.11: Hub and Blade Prism Layers

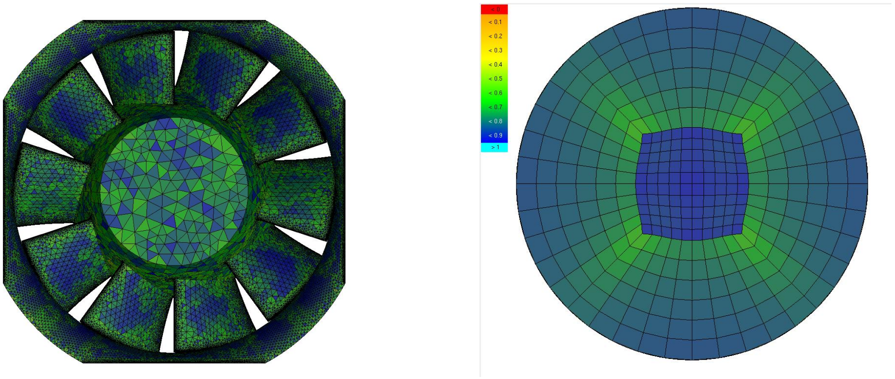

(a) Tetrahedral Cells (b) O-Grid, Hexahedral Cells

Figure 4.12: Hybrid Mesh Quality

The main advantages for using the passage-to-passage setup are the structured or unstructured hexahedral mesh and the reduced computational time. Hexahedral cells are known as a good choice for achieving better mesh quality and thus more accurate numerical analysis as compared to tetrahedral cells. A passage-to-passage turbo volume represents a section of the flow region that completely encompasses a single turbo blade, thus reducing the computational time by a factor of total number of blades. The blade is represented by a blade-shaped void in the centre of the volume (Figure 4.13). The shapes of the periodic (side) faces of the turbo volume represent projections of the turbo profile medial edges.

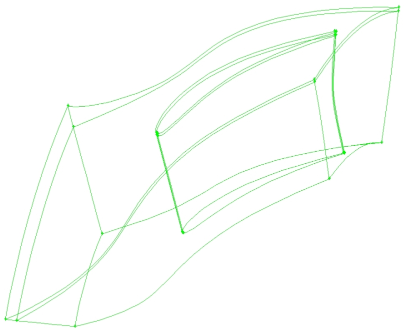

Figure 4.13: Passage-to-Passage Turbo Volume

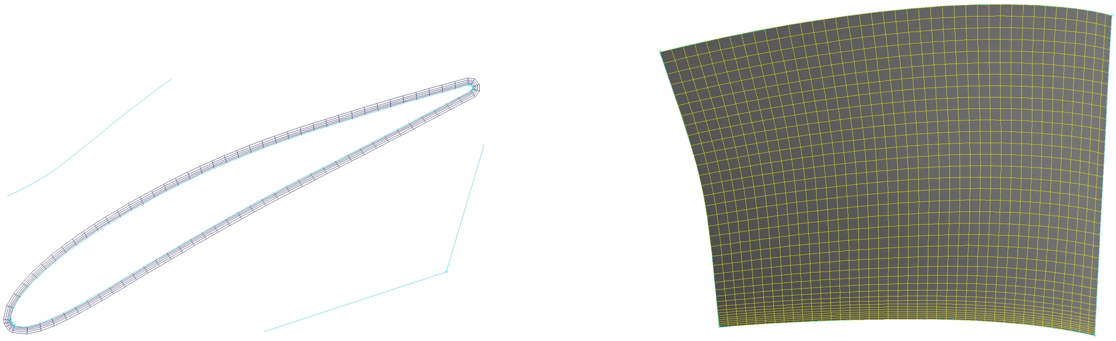

Figure 4.14: Boundary Layers and Size Function on Blade Surfaces

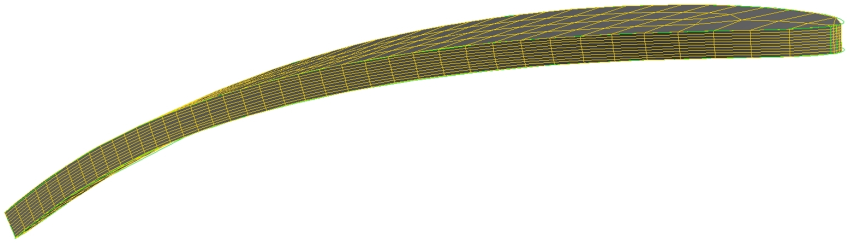

Figure 4.15: Tip Clearance Resolution

As a first step, the grid for passage turbo volume is generated. Boundary layers are introduced at all of the blade surfaces. A size function is applied for the distribution of cells from the hub surface up to the tip of the blade. The boundary layers and the size function for the turbo volume are shown in Figure 4.14.

A very fine mesh is generated in the tip clearance region to capture the flow behaviour in this region, Figure 4.15. After generating the good quality grid for the turbo volume, the remaining sectioned volume of the surrounding region is meshed. The final passage-to-passage unstructured hexa- mesh is shown in Figure 4.16.

4.5.2.1 Mesh Data

The size of cells for the blade surfaces and the boundary layer parameters are given as under:

Number of Boundary Layer Rows:	05
Wall Cell Thickness:	0.06 mm
Total Number of Cells:	140000
Maximum Skewness:	0.70

The mesh quality of the turbo volume region is shown in Figure 4.17.

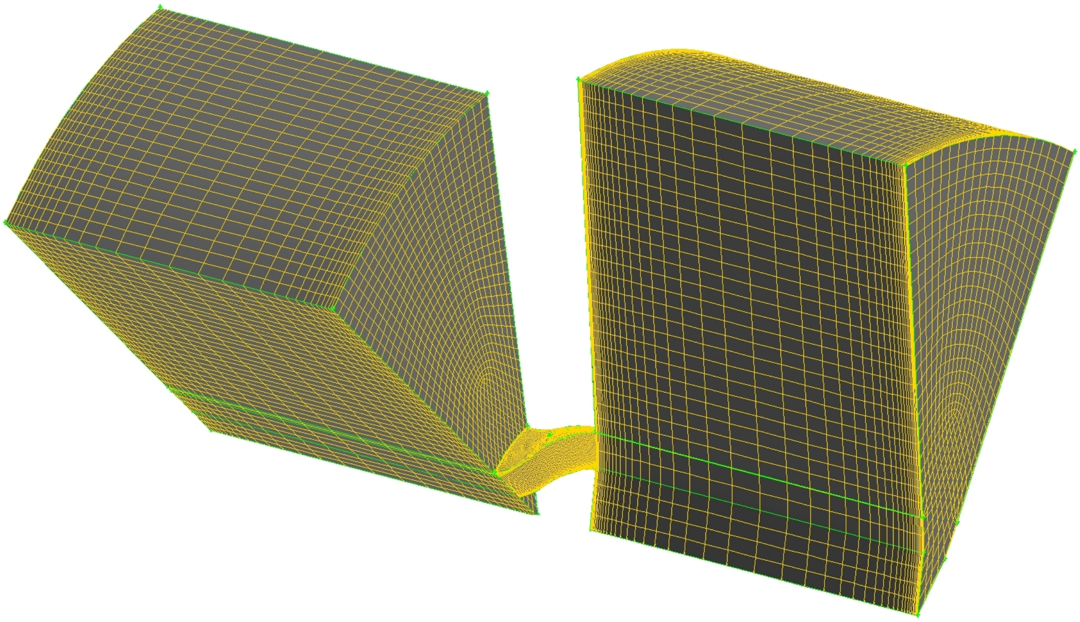

Figure 4.16: Final Hexahedral Unstructured Mesh

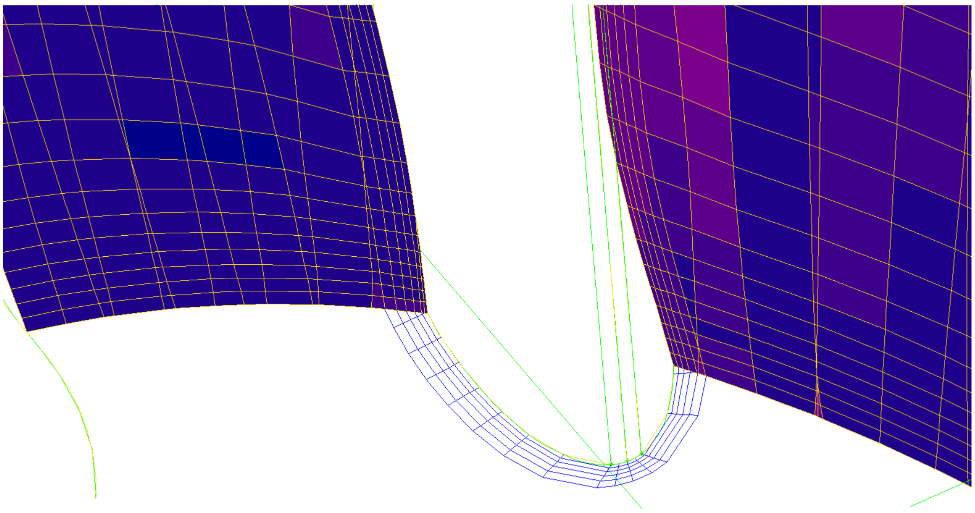

Figure 4.17: Turbo Volume Cut Plane showing Better Mesh Quality

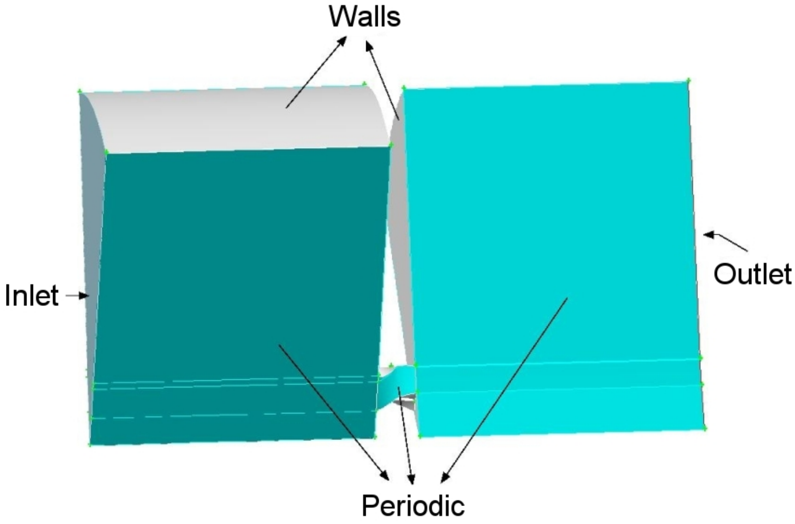

Figure 4.18: Boundary Conditions for Passage-to-Passage Setup

4.6 Turbulence Model

The two computational grids generated in ANSYS® ICEM CFD™ and GAMBIT® for the axial blower assembly are imported to the flow solver, FLUENT® V.6. The software is capable of solving diverse and complex multi-dimensional fluid flow fields.

4.6.1 Overview FLUENT Program

FLUENT® is a state-of-the-art computer program for modeling fluid flow and heat transfer in simple and complex geometries, using Finite Volume Method (FVM). The program provides complete mesh flexibility, solving the flow problems with structured/unstructured meshes. The solver supports 2D triangular/quadrilateral, 3D tetrahedral/hexahedral/pyramid/wedge, and hybrid meshes.

For full assembly hybrid grid, the operations of defining the flow model, initial and boundary conditions, fluid properties, solution controls are done completely in FLUENT®. However boundary conditions for the passage-to-passage mesh setup are partially defined in both GAMBIT® and FLUENT® packages. The boundary conditions for this setup are shown in Figure 4.18.

4.6.2 Boundary Conditions

A steady, 3D incompressible flow field simulation is performed associated with the axial blower operating at rotor speed of 3700 rpm (BEP). To capture the actual physical phenomena, several appropriate assumptions and boundary conditions are made to simulate the flow field inside the axial blower:

1. Incompressible flow, as the fluid velocity is quite low for a typical axial blower.
2. The influences of radiation heat (isothermal flow) and other properties are neglected.
3. The body force is ignored and the fluid is treated as Newtonian fluid
4. The velocity-inlet and the atmosphere outflow are set as the boundary conditions at main inlet and main outlet of blower, respectively.

Atmospheric pressure is set as the reference operating pressure. The Reynold's number based on the mid-span chord length C_m is $Re = 49200$. Uniform and constant values for the axial velocity field, the turbulent intensity and the hydraulic diameter are specified at the inlet boundary. Outflow boundary conditions are used to model flow outlets where the details of the flow velocity and pressure are not known prior to solution of the flow problem. They are appropriate where the exit flow is close to a fully developed condition, as the outflow boundary condition assumes a zero normal gradient for all flow variables except pressure [4].

The casing wall of the axial blower is absolutely stationary, while the hub and the blade surfaces are rotating. The MRF technique is adopted for the computational simulation of validation model, thus allowing for a steady-state treatment of the problem. The rotor fluid zone is rotated at 3700 rpm (BEP). The blade and hub surfaces are defined as stationary walls relative to rotor fluid zone, i.e. they are rotating at the same speed and in the same direction. The casing surrounding the rotor zone is defined to be stationary in absolute frame of reference. The walls are considered as hydraulically smooth and no-slip condition is applied to them.

In the passage-to-passage setup, grid interfaces are defined at the rotor inlet and outlet. Fluxes across the grid interfaces are computed using the faces resulting from the intersection of the two interface zones, one on each side of rotor turbo volume. The side walls of the complete setup are defined as rotationally periodic. Periodic boundary conditions are used when the physical geometry of interest and the expected pattern of the flow solution have a periodically repeating nature. It is assumed that there is no pressure drop across the periodic planes [4].

4.6.3 Numerical Scheme and Solution Control

The solution is obtained using pressure based segregated solver option with absolute velocity formulation, three dimensions in space, steady in time, and green-Gauss node based gradient. The standard k-ε turbulence model (Launder and Spalding) with a standard wall function was initially employed in the modeling. The comparison of data showed the failure of k-ε model to predict the onset and the amount of flow separation under adverse pressure gradient conditions. As a second attempt, Shear Stress Transport (SST) version of Menter's near wall resolved k-ω turbulence model is employed in the modeling.

The k-ω model performs very well close to walls in boundary layer flows, particularly under strong adverse pressure gradients (hence its popularity in aerospace applications). However

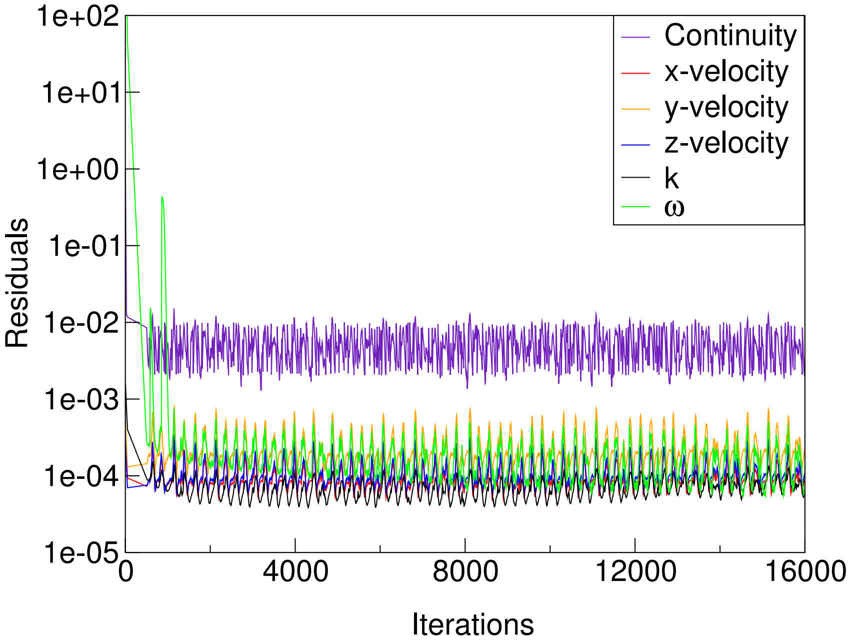

Figure 4.19: Convergence Curves

it is very sensitive to the free stream value of ω and great care is to be taken in setting this value to avoid unreal results. The SST model works by solving a turbulence/frequency-based model (k-ω) at the wall and k-ε in the bulk flow. A blending function ensures the smooth transition between the two models.

Second order upwind discretisation scheme is selected for the numerical solution of momentum, turbulence kinetic energy, and turbulence and specific dissipation rate equations. As the flow across the blower has high rates of swirl and turbulence and also it is not aligned with the grid due to the construction of unstructured mesh in the solution domain, second order discretisation is preferred for higher accuracy. Second order option is selected for the pressure interpolation scheme to obtain face pressure values while SIMPLE algorithm is opted for the pressure field. Under-relaxation factors are modified to achieve convergence. The fully converged solution is assumed for the residuals of the discretised continuity and momentum equations fall below 10^{-5}. A pressure monitor at the main outlet of the numerical model has also been set for the convergence check. The convergence behaviour is shown in Figure 4.19. Unsteady effects are quite visible thus restricting a better convergence.

4.7 Verification Assessment

Verification assessment examines that whether the computational models are the correct implementation of the conceptual models, and whether the resulting code can be properly used for an analysis. The strategy is to identify and quantify the errors in the model implementation and the solution. Verification is intended to concern itself more with mathematics rather than engineering.

There are two fundamental aspects to verification: *code verification* and *solution verification.* Code verification is the process of ensuring, to the degree possible, that there are no mistakes (bugs) in a computer code or inconsistencies in the solution algorithm. Solution verification is the process of quantifying the numerical errors that occur in every numerical simulation. Examples of these numerical errors include round-off error, iterative error, and discretisation error. While code verification is generally performed once and for all for a given set of coding options (at least for smooth problems), solution verification must be performed for each and every simulation that is significantly different than previous simulations[70, 14].

Solution verification deals with the assessment of the numerical errors which always exist when partial differential equations are solved numerically. The most general approach for estimating the discretisation error is based on Richardson extrapolation (also referred to as h-extrapolation) and requires numerical solutions on two or more meshes with different levels of refinement [70].

In this work, the solution verification is carried out by performing the simulations on four successively coarser grids . All the simulations are run for the flow rate value of 128 m^3/hr for being the critical (stall dip) region in the experimentally obtained blower performance curve (Fig. 4.2).

4.7.1 Richardson Extrapolation

Richardson extrapolation (RE) is the a posteriori error estimator that is independent of the numerical method used to obtain the numerical solutions. It is a method for obtaining a higher-order estimate of the continuum value (value at zero grid spacing) from a series of lower-order discrete values. This estimate of the exact solution can then be used to estimate the error in the numerical solutions [70]. The method can be applied to the local flow variables as well as to derived integral quantities. It can be used for the spatial discretisation as well as for the temporal discretisation. Here it is introduced for the spatial discretisation as: [5, 70]

$$f_k = f_e + g_p \cdot h_k^p + g_{p+1} \cdot h_k^{p+1} + g_{p+2} \cdot h_k^{p+2} + ... \tag{4.1}$$

where,

- f_k = computed quantity from the simulation of k^{th} mesh
- f_e = smooth exact solution value
- h = linear measure of grid
- g_p = coefficient of the leading error term
- p = observed order of convergence/accuracy
- k = mesh index, $k = 1, 2, 3, ...$

Richardson extrapolation requires three different meshes to estimate the value f_e. If $k = 1$ denotes the fine, $k = 2$ the medium and $k = 3$ the coarse grid, the order of accuracy can be calculated by solving the transcendental equation [67, 5]:

$$p = \frac{\ln[(f_3 - f_2)/(f_2 - f_1)]}{\ln(r_{21})} - \frac{1}{\ln(r_{21})} \cdot [\ln(r_{32}^p - 1) - \ln(r_{21}^p - 1)] \tag{4.2}$$

where r is the grid refinement ratio and can be defined for any two grids as:

$$r_{21} = h_2/h_1 = (N_1/N_2)^{\frac{1}{D}}, \quad r_{32} = h_3/h_2 = (N_2/N_3)^{\frac{1}{D}} \tag{4.3}$$

Here N_k represents the number of grid cells in the blade-passage area of the mesh and D is the dimension of the flow domain.

The estimate of the exact solution is obtained from:

$$f_e = f_1 + \frac{f_1 - f_2}{r_{21}^p - 1} \tag{4.4}$$

The second term on the right hand side of Eq. 4.4 defines a correction to the fine grid solution f_1.

The most common approach with generalised Richardson extrapolation in grid convergence studies is to calculate the relative error or an error band. This is in general done for the solution on the fine grid. The method is based on Grid Convergence Index, or GCI which is defined as [70]:

$$\text{GCI} = \frac{F_s}{r_{21}^p - 1} \cdot \left| \frac{f_2 - f_1}{f_1} \right| \tag{4.5}$$

where F_s is a factor of safety and is set to 1.25 when the order of accuracy is calculated from solutions of three meshes [67]. The GCI combines the often reported relative difference between solutions with the $(r_p - 1)$ factor of the Richardson extrapolation-based relative discretisation error (RDE) estimator (Eq. 4.6).

$$\text{Rel. Diff.} = \frac{f_2 - f_1}{f_1}, \qquad \text{RDE} = \frac{f_1 - f_e}{f_e} = \frac{f_2 - f_1}{f_e \cdot (r_{21}^p - 1)} \tag{4.6}$$

The RDE is simply the difference between the numerical solution and the exact solution, normalised by the exact solution, here given for the fine grid (k = 1).

The GCI provides an error band and not an error estimate. Most importantly, it correctly accounts for the assumed order of accuracy p and the grid refinement factor r [70].

4.7.2 Verification Results

In order to verify the numerical solutions obtained, a post-processing procedure based on the generalised Richardson extrapolation for *h-refinement* studies and on the Grid Convergence Index (GCI) is applied. It has been used in order to establish a criteria about the sensitivity of the simulation to the computational model parameters that account for the discretisation: the mesh spacing and the order of accuracy of the numerical solution p and the error band where the independent grid solution is expected to be contained.

Mesh Index $\boldsymbol{k}$	**Number of Cells** $\boldsymbol{N_k}$	**Pressure Rise** $\mathbf{P_s}$, Pa
1	84500	92.65
2	66000	92.30
3	55500	91.30
4	49600	87.50
5	27600	80.30

Table 4.2: Pressure Rise Data for Different Grids

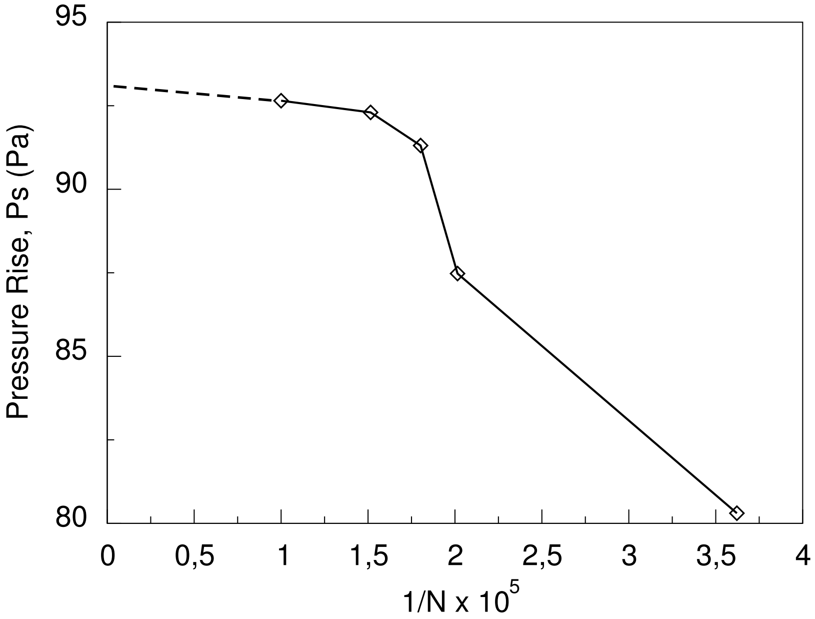

Figure 4.20: Pressure Rise vs. Inversed Number of Grid Cells

Table 4.2 indicates the grids' information and the resulting pressure rise obtained from the properly converged numerical simulations.

The plot of pressure difference with varying grid cells is shown in Figure 4.20. The reciprocal of number of cells in each grid is normalised by the reciprocal of the number of cells in the finest grid ($k = 1$). The figure shows that as the number of grid cells increases (mesh: 1, 2 and 3), the pressure rise follows an asymptotic behaviour i.e. approaching zero-grid spacing. The meshes $k = 4$ and $k = 5$ have not presented the asymptotic behaviour thus showing the increase in discretisation errors due to coarser grids.

The estimates of the pressure rise are obtained after determining the order of convergence for different mesh combinations and then applying the Richardson extrapolation. The results and the computed GCI for the fine grid solution in each combination are given in Table 4.3. The observed order of accuracy (p) for each mesh combination is found to be close enough to its theoretical value. Moreover, the uncertainty due to discretisation (GCI) decreases with grid refinement.

Mesh Combination	**Convergence Rate, p**	**Estimated Value, f_e (Pa)**	**GCI, %**
1, 2, 3	2.71	94.01	1.86
1, 2, 4	3.02	93.80	1.68
1, 2, 5	2.10	92.90	2.40
1, 3, 4	3.30	93.53	3.07
1, 3, 5	2.04	93.62	5.50
1, 4, 5	1.10	96.90	33.50
2, 3, 4	3.42	93.18	6.10
2, 3, 5	1.86	93.22	11.80

Table 4.3: Verification Results for Different Mesh Combinations

Based on this verification study it can be stated that the estimated pressure rise for the axial blower at 128 m^3/hr is 93.8 Pa with a minimum error band of 1.68% for the mesh combination $k = 1$, 2 and 4.

4.8 Comparison and Analysis

The flow simulations are run at eight different flow rates to obtain a pressure-volume flow curve. The simulation at zero-flow rate is not successful due to the flow solver limitation of having some inlet flow velocity. After simulation and post-processing, the computational results are compared and analysed with the experimental results. Figure 4.21 shows the results of the numerical simulation, for the full assembly setup mesh, obtained using k-ε and SST k-ω models.

For k-ε turbulence model, the curve shows that at peak efficiency the static pressure rise across the blower is in good agreement with the experimental measurements within the range of data uncertainty. However, the static pressure rise at higher volume flow rates is lower than that determined in experiment. Also the typical stall dip at low flow rates cannot be reproduced by the computational model.

It is concluded that the k-ε model has poorly predicted the flow separation process, which is actually one of the major weaknesses of this model. Standard two-equation turbulence models often fail to predict the onset and the amount of flow separation under adverse pressure gradient conditions, which is true for an axial blower. The real flow is likely to be much closer to separation (or more separated) than the calculations suggest.

A contour plot of the computed y-plus (y^+) distribution on the rotor surfaces is shown in Figure 4.22. The y^+ value is found to be within the range defined for k-ε turbulence model with a standard wall function, that is $y^+ > 30$.

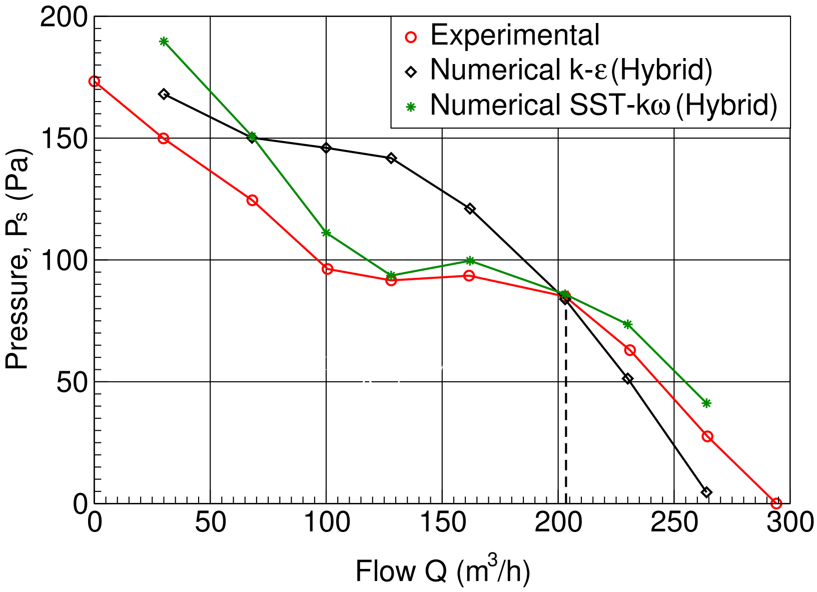

Figure 4.21: Comparison: Experimental and Numerical Δp vs. Q (Hybrid Grid)

For SST k-ω turbulence model, the curve shows that the static pressure rise across the blower is in better agreement with the experimental measurements for medium to high flow rates, as compared to k-ε model simulation results. Keeping the experimental errors in view, the typical stall dip at low flow rates seems to be reasonably reproduced by the SST k-ω computational model. However, the static pressure rise at lower volume flow rates is much higher than that determined in experiment and in the k-ε simulations.

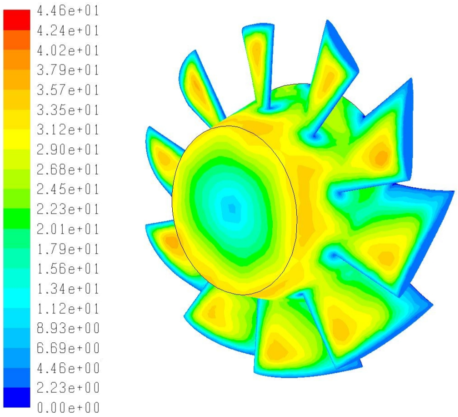
4.46e+01
4.24e+01
4.02e+01
3.79e+01
3.57e+01
3.35e+01
3.12e+01
2.90e+01
2.68e+01
2.45e+01
2.23e+01
2.01e+01
1.79e+01
1.56e+01
1.34e+01
1.12e+01
8.93e+00
6.69e+00
4.46e+00
2.23e+00
0.00e+00

Figure 4.22: Contours of Wall y-plus, k-ε Model

A contour plot of the y-plus (y^+) distribution obtained using SST k-ω turbulence model is shown in Figure 4.23. The value varies as $0 < y^+ < 10$ which is in the acceptable range.

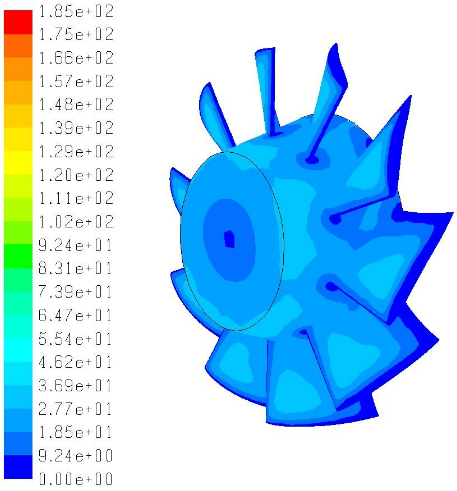
1.85e+02
1.75e+02
1.66e+02
1.57e+02
1.48e+02
1.39e+02
1.29e+02
1.20e+02
1.11e+02
1.02e+02
9.24e+01
8.31e+01
7.39e+01
6.47e+01
5.54e+01
4.62e+01
3.69e+01
2.77e+01
1.85e+01
9.24e+00
0.00e+00

Figure 4.23: Contours of Wall y-plus, SST k-ω Model

The simulation results after the modification from tetra-hybrid grid to hexa-grid passage to passage setup are given in Figure 4.24 as a comparison between the experimental and numerical values of Δp and Q. SST k-ω turbulence model is mainly employed for the numerical simulations.

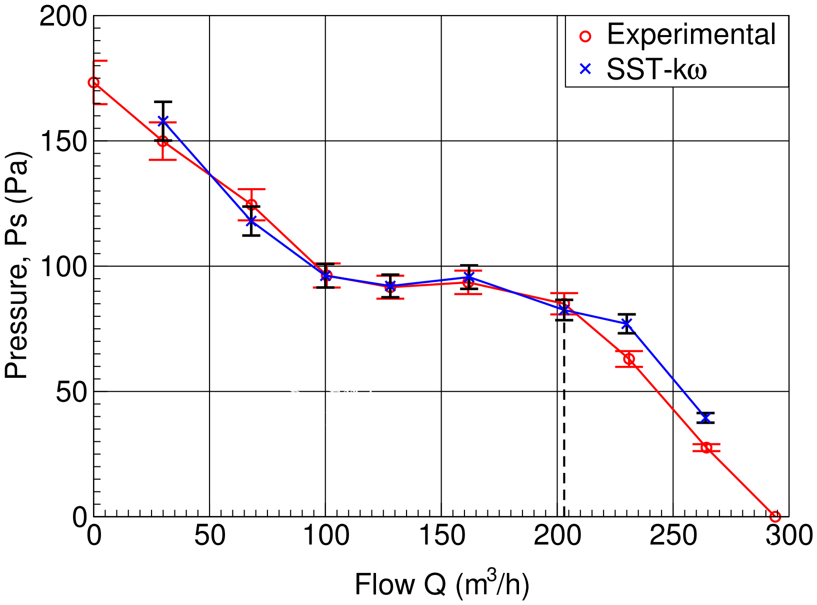

Figure 4.24: Comparison: Experimental and Numerical Δp vs. Q (Hexa- Grid)

The comparison shows better results than the values obtained from the hybrid grid. The representation of the stall dip is very much close to the actual curve. The static pressure rise at higher flow rates, beyond BEP, is higher than the experimental values but since it

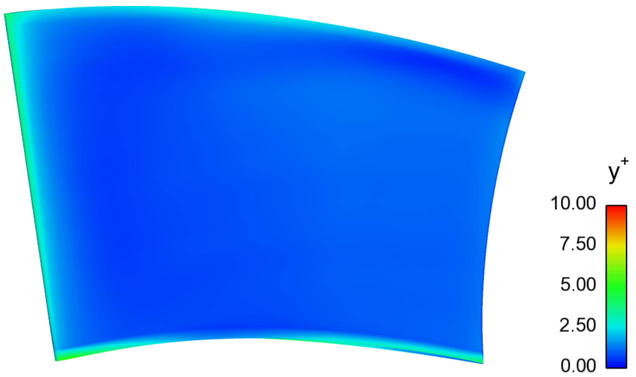

Figure 4.25: Contour of Wall y-plus, Passage-to-Passage (Hexa- Grid)

is not in the region of interest so can be ignored. The y-plus (y^+) contour (Figure 4.25) shows the variation of y^+ value from $0 - 3$, which is in the defined range for the SST k-ω model with hybrid wall function.

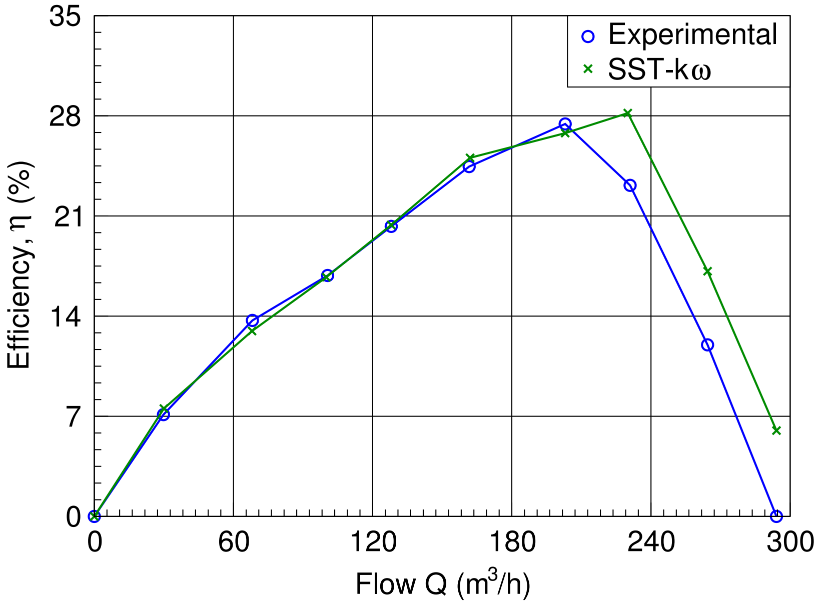

Figure 4.26: Efficiency Comparison (Hexa- Grid)

Figure 4.26 shows the comparison between the efficiency curves obtained from the experimental values and from the numerical simulation of the hexa-grid with SST k-ω model. The values have a very good match at lower flow rates, however slightly higher efficiency values are obtained beyond the design point in case of numerical simulation. The geometric simplifications like removal of fixtures from the actual geometry and extension of hub may have caused a slight increase in the efficiency beyond the BEP.

Figure 4.27 shows the overall comparison of results obtained from all simulations carried out on different types of grids. The characteristic curve from hexa- grid simulation with

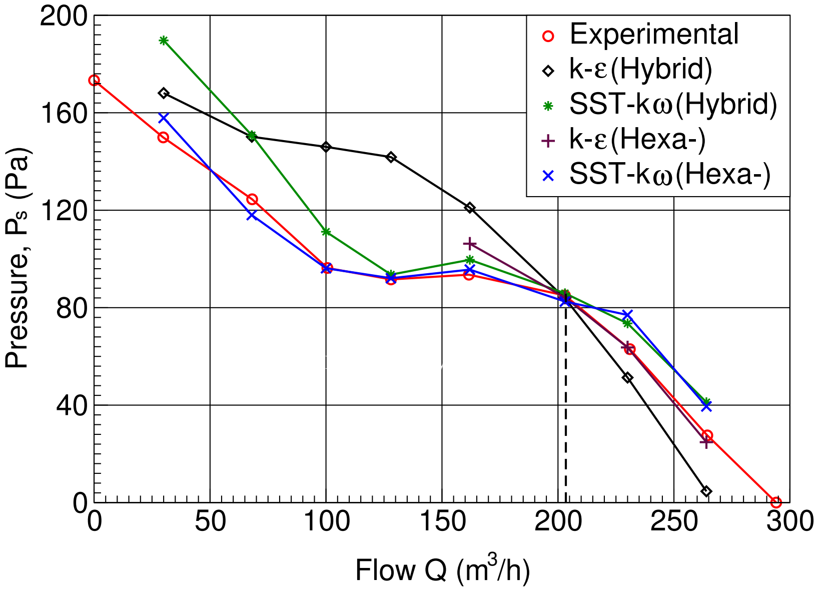

Figure 4.27: Overall Comparison: Δp vs. Q

standard k-ε model at flow rates close to BEP is also added here. It confirms the prediction inability of flow separation by the k-ε model under adverse pressure gradients. However, the model behaved very well at BEP and higher flow rates. An interesting feature observed in the overall comparison is that irrespective of computational grids and the turbulence models chosen, the Δp value is almost always the same at BEP in all the simulation results. This can be considered as grid independence but only at BEP. It can be concluded that the validation studies should not be limited to BEP and calculations must also be performed for other data points to have the real comparison.

The percent relative difference of the experimental and numerical data for both mesh types is given in Table 4.4.

Flow Rate, Q	**Pressure P_s (Exp)**	**SST-kω (Hybrid)**		**k-ε (Hybrid)**		**SST-kω (Hexa)**	
m^3/hr	**Pa**	**Pa**	**Diff. %**	**Pa**	**Diff. %**	**Pa**	**Diff. %**
30.00	149.90	168.11	12.14	189.70	26.54	157.92	5.31
68.00	124.50	150.21	20.64	150.81	21.09	118.03	5.21
100.00	96.30	146.00	51.64	111.21	15.46	96.24	0.10
128.00	91.60	141.80	54.79	93.63	2.14	92.14	0.52
162.00	93.50	121.04	29.36	99.72	6.55	95.62	2.23
203.00	85.00	83.90	1.29	85.92	1.08	83.00	2.35
230.00	62.90	51.32	18.44	73.54	16.93	77.02	22.42
264.00	27.50	4.61	83.27	41.24	49.79	39.50	43.52

Table 4.4: Relative Difference: Experimental and Numerical Data

Part III

Blade Design

Chapter 5

Design of Blade Profile

5.1 Background

The field of turbomachinery engineering has maintained a continuous research program on high performance axial flow fans. Several fan units of blades with different profile modifications have been designed and tested through global (characteristic curve and efficiency) measurements. Details of the flow fields developing upstream and downstream of selected rotors were usually measured using Laser Doppler Anemometry (LDA). Nowadays, this research has been supplemented with powerful CFD tools. The CFD technique offers a unique possibility for investigation of interblade flow phenomena, which were not accessible through the LDA tool.

The conventional design of axial flow fan and compressor rotor blades incorporates radial stacking (RS), i.e. the centres of gravity of the individual blade sections are stacked on a radial line. However, non-radial stacking (NRS) technique has been found to be more active in the turbomachine designs, nowadays. A comprehensive overview is given in [27] on NRS as a useful supplement to blade optimisation achievable with RS techniques. NRS offers increased capability for reduction of near-endwall and tip clearance losses as well as control of secondary flows and radial migration of high-loss fluid. On this basis, NRS is widely applied for performance and efficiency improvement, e.g.[8, 15, 16, 27, 55, 57]. Simultaneously, NRS provides a unique means for rotor noise reduction as well [27, 94].

Blade sweep, dihedral, and skew are known as NRS techniques for blade rows of axial flow turbomachinery [82]. Recently, the leaned, swept, and skewed blade has become a matter of interest in the design of turbomachinery blades [39]. Skewed and swept blade technique is originated from the research achievements of aircraft airfoil. Since the time this technique was introduced to turbomachinery field, it has played a very important role in the performance improvement of turbomachinery. So far, many research results have proved that the skewed and/or swept technique would promote aerodynamic efficiency, reduce throughflow losses, enhance stable range, as well as decrease the aerodynamic noise of turbomachinery [96].

The NRS design technique applied in this work is the forward sweeping of rotor blades whose effects on rotor flow field are investigated by means of advanced CFD tools.

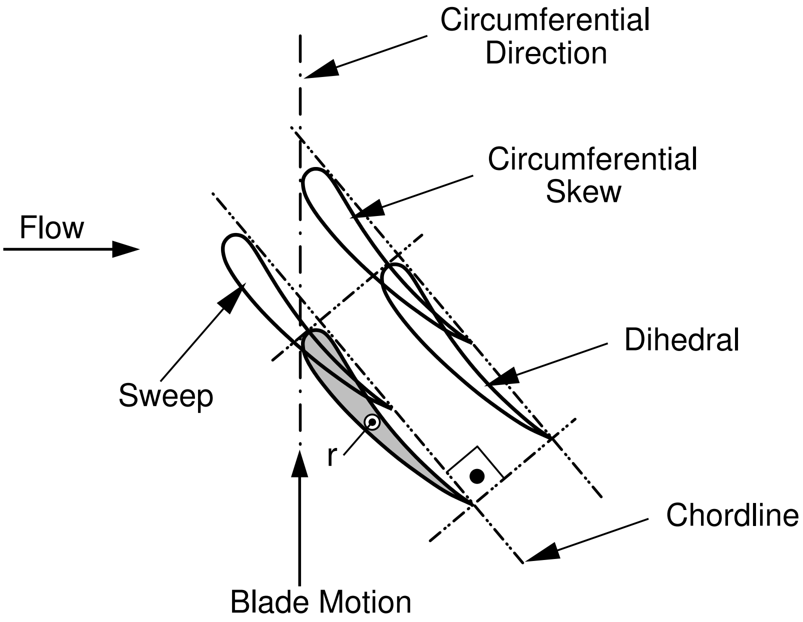

Figure 5.1: Sweep, Dihedral, and Circumferential Skew

5.2 Basic Definitions

The basic definitions of the NRS techniques are geometrically demonstrated in Figure 5.1.

5.2.1 Blade Sweep

The use of aerodynamic sweep is one of the most significant design trends to improve the performance and stability of the rotor blades. An axial flow turbomachinery blade is swept when each blade section of a datum blade with a radial stacking line is displaced parallel to its chord line in a prescribed manner. Thus, turbomachinery blades are said to have sweep when the flow direction is not perpendicular to the spanwise direction [77].

A blade has forward/backward sweep (FSW/BSW) if the sections of a RS datum blade are shifted parallel to their chord in such a way that a blade section under consideration is upstream/downstream of the adjacent blade section at lower radius (Figure 5.2) [16]. Sweep is said to be positive/negative [(+)SW/(-)SW] near the endwall when a blade section under consideration is upstream/downstream of the adjacent inboard section [82], as explained in Figure 5.3.

5.2.2 Dihedral

A blade is dihedral if the sections of a datum blade of RS line are displaced normal to the chord (Figure 5.1). Dihedral is said to be positive/negative [(+)DH/(-)DH] when the endwall makes an obtuse/acute angle with the suction side (SS) respectively [27].

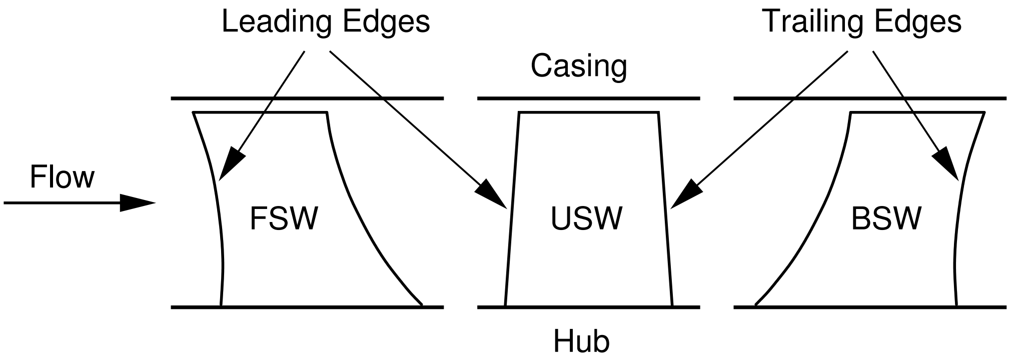

Figure 5.2: Forward and Backward Sweep

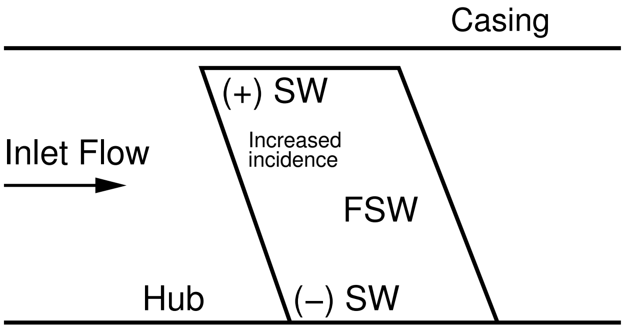

Figure 5.3: Positive and Negative Sweep, Forward Swept Blade

5.2.3 Blade Skewness

So far, there is no unified definition of a skewed blade in the turbomachinery field [96]. Circumferential-skewed blade is defined as a special combination of sweep and dihedral, for which the datum blade sections are shifted in the circumferential direction, towards/against the direction of rotation [82]. Forward skewness and backward skewness can thus be distinguished on the basis of positive and negative skew angle (δ_{sk}), respectively (Figure 5.4).

5.3 Unswept (USW) Rotor: New Reference

The unswept (USW) blade used in the validation studies has been approximately regarded as a radial blade because of the very small angle between the Leading Edge (LE) and the radial line from hub surface. The rotor has tapered hub and the unique casing with bell shaped inlet and conical outlet. This conical outlet has appeared to be a geometrical constraint for the incorporation of forward sweep, as the blades intersected with the casing at higher sweep angles. Also, the conical shape of casing does not allow to keep the tip clearance constant throughout the length of blade when swept forward. The problem has been overcome by creating a new unswept reference blade by converting the conical

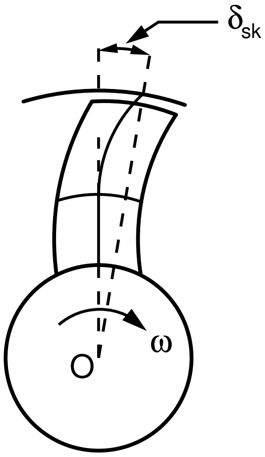

Figure 5.4: Forward Skewed Fan Blade

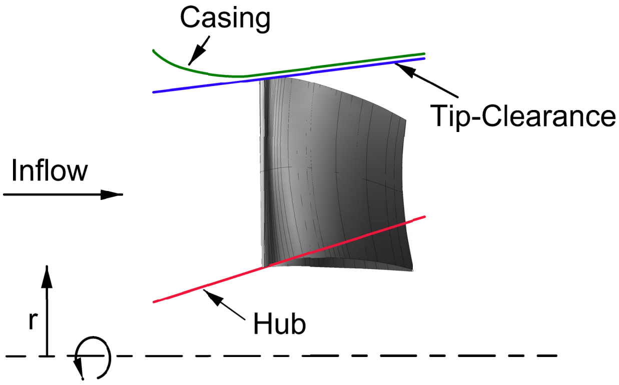
Casing
Tip-Clearance
Inflow
r
Hub

(a) Unswept Rotor, Conical Casing

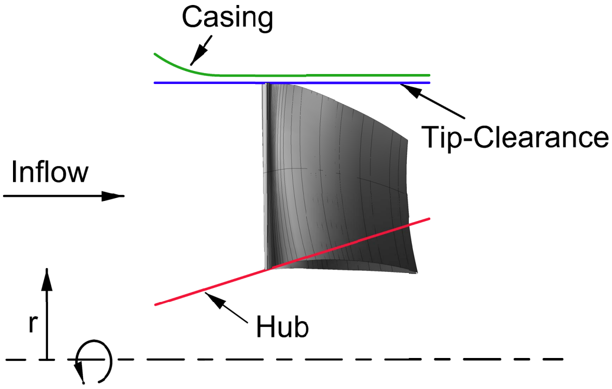
Casing
Tip-Clearance
Inflow
r
Hub

(b) Unswept Rotor, Cylindrical Casing

Figure 5.5: Unswept Old and New Reference Rotors

casing of the old reference blade into a cylindrical casing. This modification has reduced the downstream span of the blade and at the same time narrowed the outlet of the rotor (Figure 5.5). Although the nozzle effect at the outlet will surely have a negative effect on the performance of the blower, as can be seen in Figures 5.6(a) and 5.6(b), but the main idea behind this modification is to improve the already "low performing blower" by applying forward sweep. In this way a better comparison environment has been created.

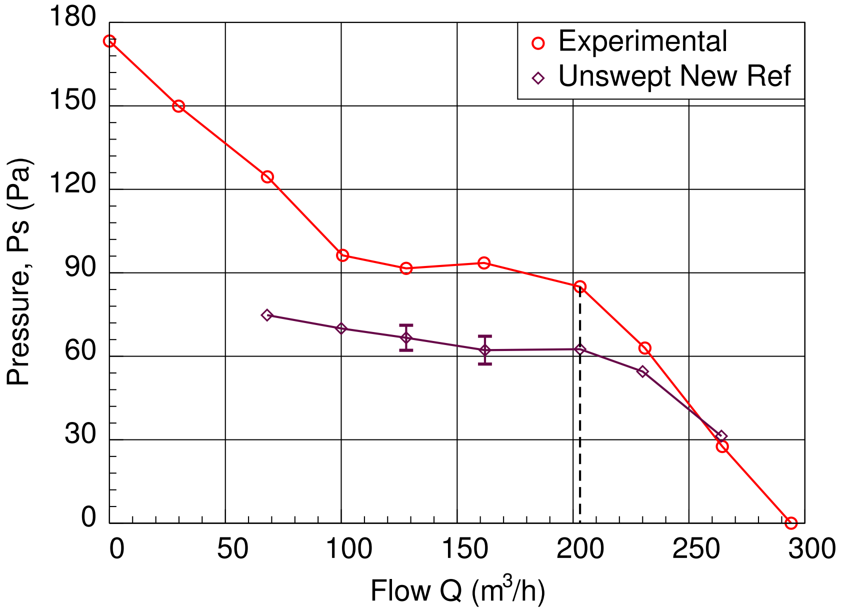

(a) Static Pressure Curve, New USW Rotor

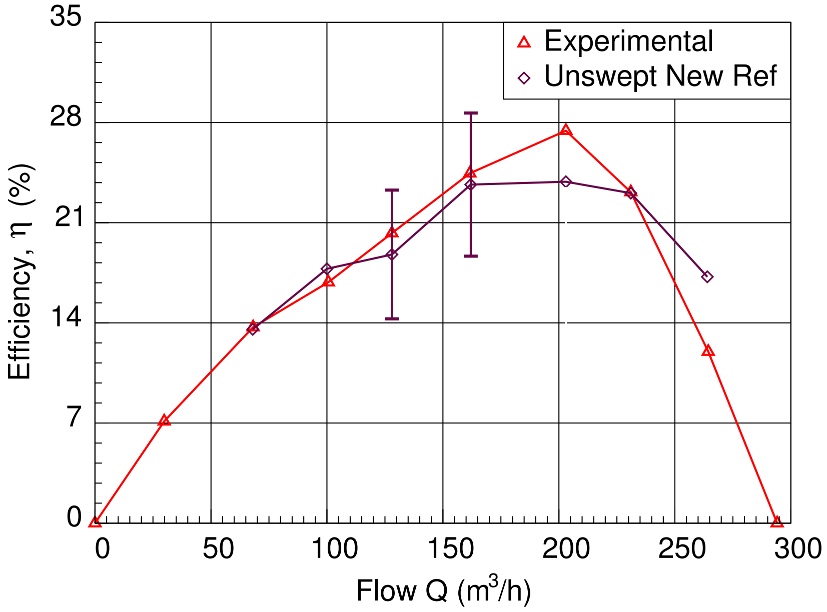

(b) Efficiency Curve, New USW Rotor

Figure 5.6: Performance Comparison, New USW Rotor

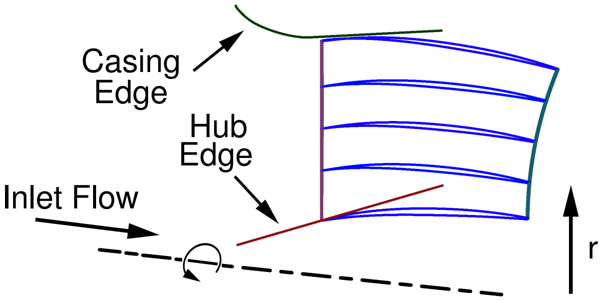

Figure 5.7: Blade Profile Sections and Main Edges of USW Rotor

External Dimensions, mm^3	$127 \times 127 \times 38$
Rotor Speed, N (rpm)	3700
Specific Speed, N_s (rpm)	198
Tip Radius (Inlet), r_t (mm)	58.00
Hub Taper Angle, θ (deg)	17.5
Chord Length (Mid Span), C_m (mm)	32.74
Hub-Tip Ratio (Inlet), χ_{in}	0.55
Number of Blade, Z	10
Blade Pitch (Mid Span), s_m (mm)	28.60
Blade Solidity, C_m/s_m	1.14
Blade Stagger Angle (Mid Span), γ_m (deg)	53.5
Reynold's Number, Re (mid-span chord length)	49200

Table 5.1: Main Geometrical and Operational Characteristics of USW Rotor

The key geometrical, design and flow parameters of USW datum rotor are summarised in Table 5.1. The hub/casing edges and blade sections are shown in Figure 5.7.

5.4 New Design of Profile

The literature reflects a consensus that forward sweep gives potential for the following advantages in the part load operational range (flow rates lower than design) [8, 15, 16, 27, 55, 57, 85, 86, 87, 89, 94]:

- improvement of performance and efficiency,
- increase of total pressure peak, and
- extension of stall-free operating range by improving the stall margin

However, the research results are rather diversified from the aspect of performance and loss modifying effects due to forward sweep at the design flow rate [82].

NRS is usually confined to only a portion of span e.g. to the near-endwall regions – in the case of compressor blades [55, 82] for mechanical reasons, and may even be confined to the leading/trailing edge (LE/TE), but can be extended even to the entire span for ventilating fans [8, 15, 16, 46, 57, 94]. The open literature also shows that mostly a single swept blade case study is compared with an unswept datum blade [87].

Forward sweep is chosen in this study for the advantages like improved performance at lower flow rate region and wider stall margin [90]. The main part of the current research work is to modify the existing blade by introducing forward sweep to its entire blade LE span. Four (04) design modifications are made on the theoretically identical blades to analyse the effects on their performance. The flow structure within the blades and behind the rotors, as well as the loss distributions, will be investigated for swept and unswept rotors. The expected goal is to obtain efficiency gain by applying forward sweep not only at the part-load operating range but also near the design point and at the overload range (flow rates higher than the design flow rate). Moreover, the performance of the FSW rotor should not fall below the prescribed total pressure rise representing the user demand.

5.4.1 Design Basis and Assumptions

The literature study shows that usually some of the parameters (one or the other) are varied as a part of incorporating aerodynamic sweep into the blading geometry [15, 39, 89]. These may include blade count, hub/tip ratio, stagger angle, camber angle, chord length and the related solidity etc.

The new design study is carried out on 04 sets of rotor blades with different forward sweep angles, λ. These studies are to be harmonised with the previous work carried out so far on the unswept rotor in this thesis. This means that the basic geometrical and design flow parameters of the unswept bladed rotor and the swept bladed rotor must be identical. As a consequence, a reasonable comparison can be carried out between the unswept and swept rotors in order to explore the effects of blade sweep on rotor fluid dynamics.

No attempt has been made to modify the stagger angle or airfoil parameters so as to take into account the altered flow field that had been caused by the varied sweep angles. The blade element profile geometry at different sections for the swept blade rotor on each cylindrical position are identical to those of the unswept rotor. The tested rotors are designed with same geometric features (i.e. the blade count, hub-to-tip ratio, chord length and the related solidity etc).

The sweep angle λ is computed according to the sketch shown in Figure 5.8. Thus it is defined as the angle between the leading edges of the USW and FSW blades. The classic sign convention [77] is applied here, i.e. the sweep angle is negative for forward sweep.

The swept rotors will be numerically simulated for comparison at the same volume flow and rotor speed as that of the reference rotor.

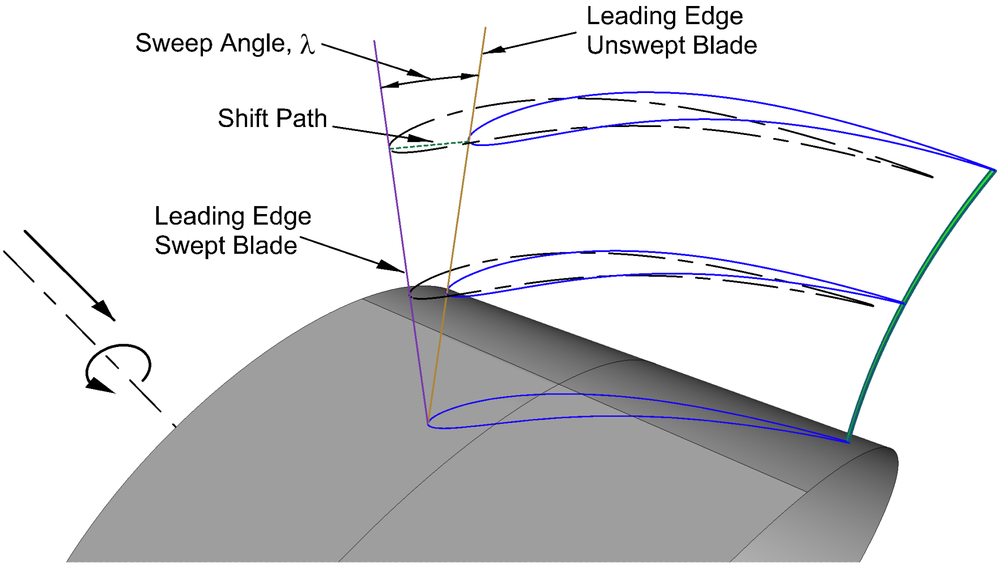
Sweep Angle, λ
Leading Edge
Unswept Blade
Shift Path
Leading Edge
Swept Blade

Figure 5.8: Sweep Angle Description

5.4.2 Design Technique and Procedure

Several approaches can be found in the literature to incorporate the forward sweep. The main emphasis while applying sweep is to keep the basic geometrical features the same. Another aspect is to shape the blade in a way that it has sweep but no dihedral, thus eliminating the radial component of the force representing blade action and consequently simplifies the matter.

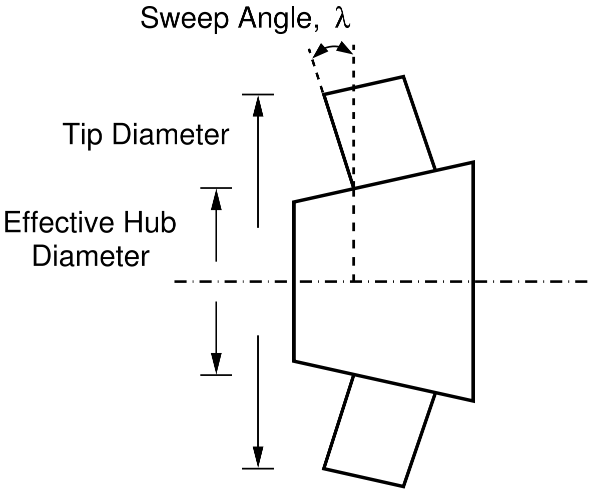
Sweep Angle, λ
Tip Diameter
Effective Hub
Diameter

Figure 5.9: Simplified Forward Sweep Technique

Four sets of rotor blades are made with varying degrees of sweep. The forward-swept rotors (FSW) have been derived from USW by simply moving forward the radial blade profiles (Figure 5.9). Starting at the hub and moving incrementally in the radial direction

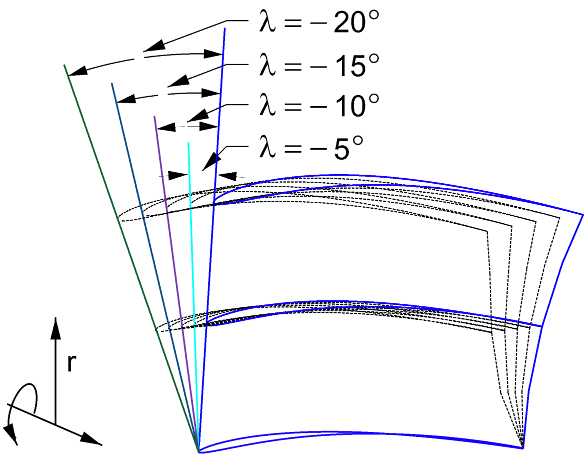

Figure 5.10: Moved Sections of Modified Rotors, Forward Sweep

towards the casing, the blade sections are shifted in the direction of the respective blade chords (relative design flow direction) on coaxial cylindrical planes. The distance through which the blade sections are moved vary linearly from zero at the hub to the maximum at the tip. This was done in such a way that the blade axis assumes the specified sweep angle at each radial position. Spanwise constant sweep angles of $\lambda = 5$, 10, 15 and 20 degrees have been adjusted for the four FSW Rotors I, II, III, and IV, respectively.

The side view of tip and mid span profiles of swept blades is shown in Figure 5.10. Despite the recommendations in the literature for sweep correction in order to retain the performance of the unswept blading [77, 86], the swept blades have deliberately been left uncorrected since no information was available whether the correction recommendations are valid for such low aspect ratio bladings.

Figure 5.11 shows the comparative view of the unswept rotor and the modified forward swept rotors I, II, III and IV.

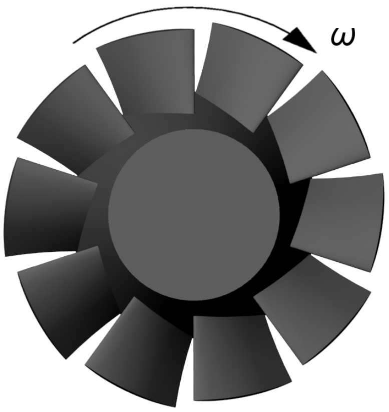

(a) Unswept Rotor

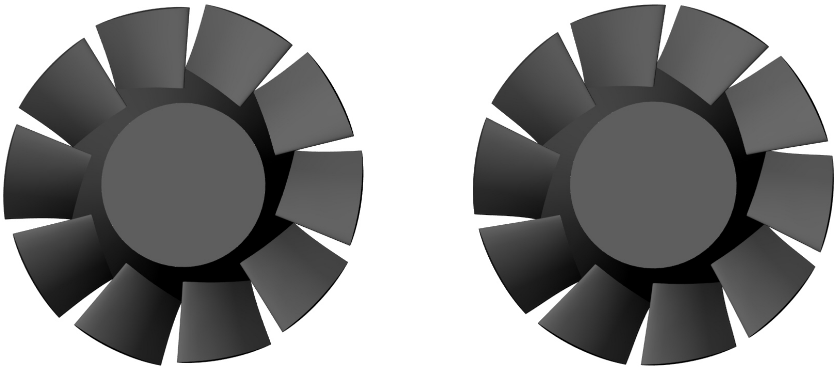

(b) Rotor I, $\lambda = 5°$

(c) Rotor II, $\lambda = 10°$

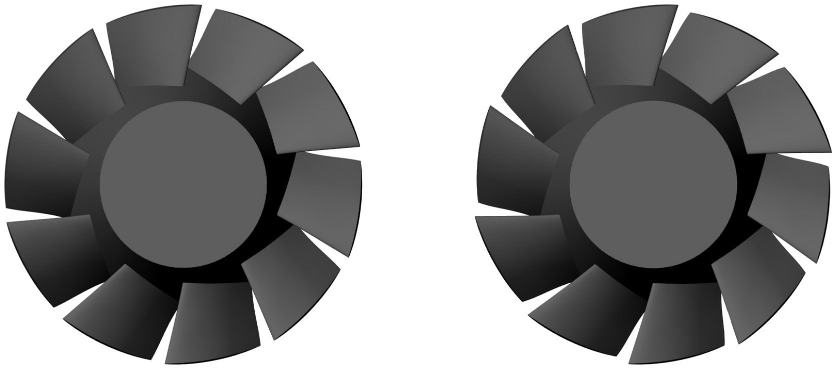

(d) Rotor III, $\lambda = 15°$

(e) Rotor IV, $\lambda = 20°$

Figure 5.11: View of Unswept and Swept Rotors

Part IV

Results and Conclusions

Chapter 6

Results and Discussion

6.1 Computational Mesh

The flow field in the new Unswept (USW) rotor is simulated. A new optimized grid has to be generated for these simulations because of two main reasons. Firstly, the actual Unswept rotor has been replaced by a new Unswept rotor having a modified geometry (as discussed in Section 5.3). Secondly, some of the critical desired 3D flow effects could not be resolved and obtained from the simulations of previous meshes. The meshes for the test rotors are generated with optimum number of grid cells of maximum possible good quality on the basis of grid convergence studies of the new USW reference blade.

6.1.1 Grid Independence

Six different discretisation grid levels are used for the numerical computation to study the grid independence. The already generated “coarse” mesh consisting of about 0.25 Million unstructured hexahedral cells is chosen as a base. The mesh is refined mainly in the blade vicinity and single-blade passage to obtain new grids with 0.7 Million, 1.0 Million, 1.2 Million, 1.4 Million and 1.8 Million cells. The numerical and visualisation results obtained

Mesh Index $\boldsymbol{k}$	**Number of Cells** $\boldsymbol{N_k}$**, (Millions)**	**Pressure Rise** $\mathbf{P_s}$**, Pa**
1	1.80	66.76
2	1.40	66.73
3	1.20	66.70
4	1.00	66.67
5	0.70	59.58
6	0.25	49.60

Table 6.1: Pressure Rise Data for Different Grids, New Reference USW

from the simulation of these models are used to achieve the grid independence for the new USW reference rotor.

The static pressure rise data (Table 6.1) is one of the sensitive indicators of dependence of the numerical solution on discretisation. The quantitative integral values lie almost in the same range for the grids N_1, N_2 and N_3 having 1.8M, 1.4M and 1.2M cells, respectively.

In Figure 6.1, the streamlines on the Suction Side (SS) of the blade show very small changes with the grid refinement. The visual inspection of 3D flow structures (vortices) show the similar behaviour. The boundary flow and 3D effects are successfully resolved using the refined grids, as shown in Figure 6.2.

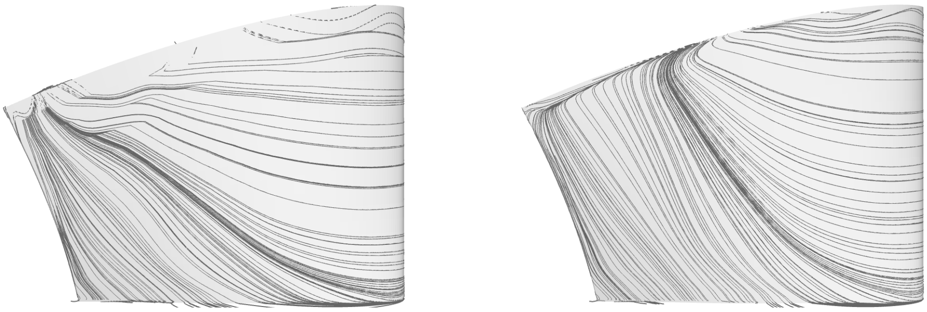

(a) 0.25M Grid Cells (b) 0.7M Grid Cells

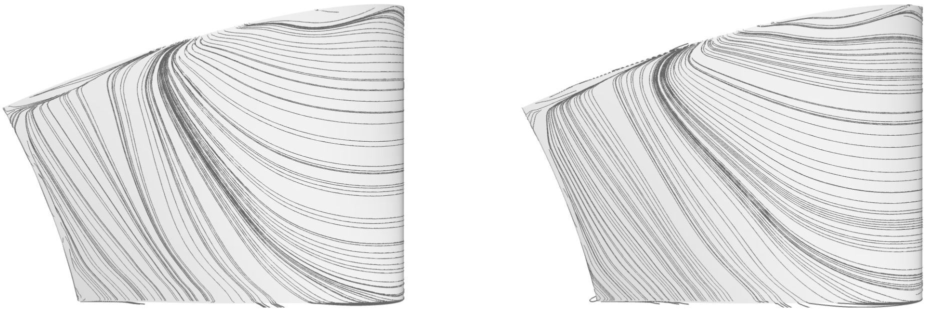

(c) 1M Grid Cells (d) 1.2M Grid Cells

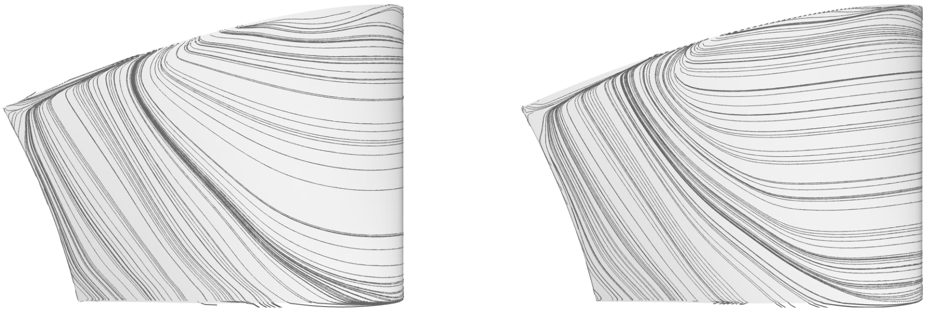

(e) 1.4M Grid Cells (f) 1.8M Grid Cells

Figure 6.1: Streamlines on Suction Side for Different Grid Sizes

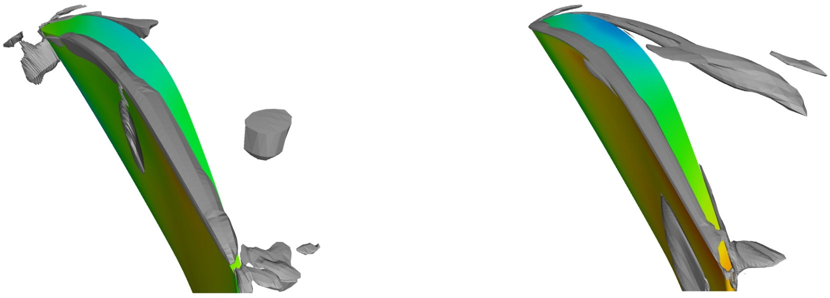

(a) 0.25M Grid Cells (b) 0.7M Grid Cells

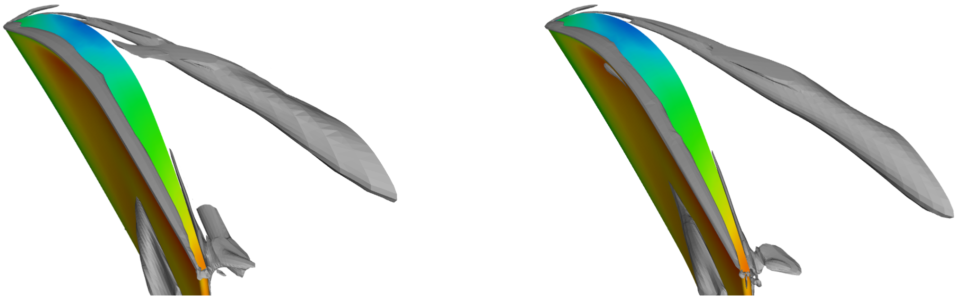

(c) 1M Grid Cells (d) 1.2M Grid Cells

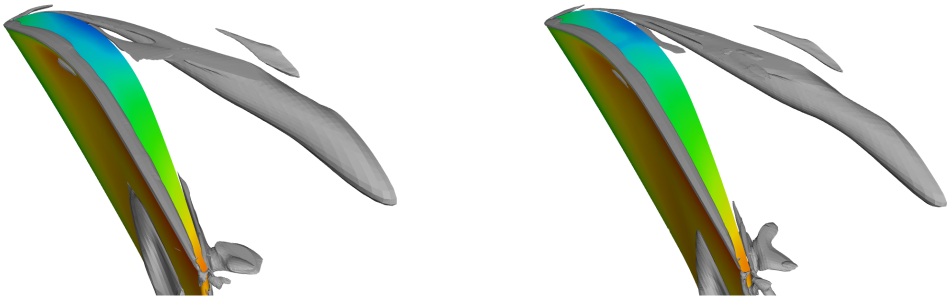

(e) 1.4M Grid Cells (f) 1.8M Grid Cells

Figure 6.2: Comparison of Vortex Generated with Variation in Grid Size

6.1.2 Solution Verification

The numerical solution verification for the new reference blade is done with the the Richardson extrapolation (RE) method which has already been described in Section 4.7.1.

The plot of pressure difference as a function of inversed number of grid cells is shown in Figure 6.3. The curve represents a good indication of the grids being in the asymptotic range. Table 6.2 illustrates the extrapolated static pressure rise with respective apparent order p, relative discretisation error (RDE) and grid convergence index (GCI) for two selected mesh combinations. The observed order of accuracy (p) for each mesh combination is found to be close enough to its theoretical value, however it a bit higher for mesh sequence N_1, N_2, N_3 which might be an indication of oscillatory convergence.

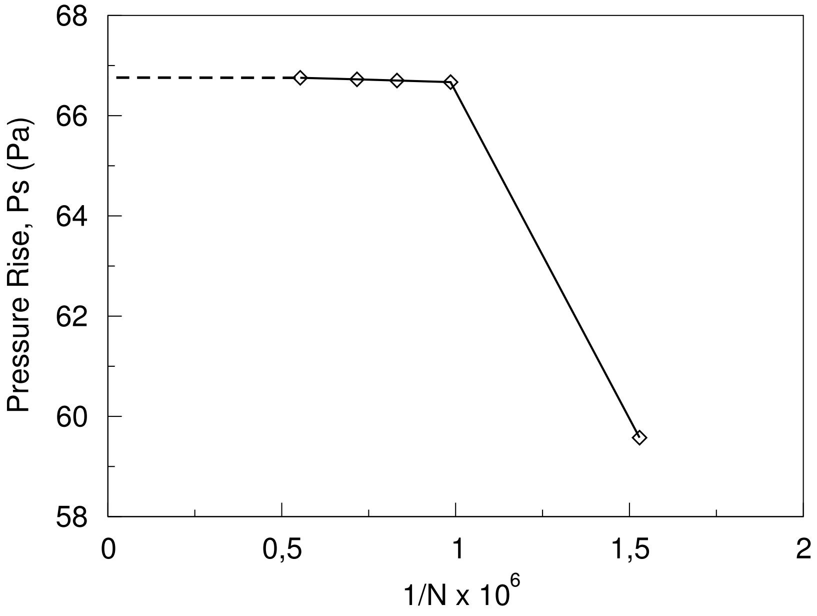

Figure 6.3: Pressure Rise as a function of Inversed Number of Grid Cells

The mesh N_2 (1.4M cells) is finalized as a reference mesh for the swept rotors, as further refinement seems needless for the accuracy of the numerical solution. Moreover, the convergence order for the mesh combination with N_2 being the finest mesh is much closer to the theoretical value. The grid-independency of results is achieved on an acceptable level from the aspect of present studies. Based on the error estimation calculations, the numerical uncertainty in the N_2-grid solution for the static pressure rise is 0.41%.

6.2 Overall Performance

6.2.1 Steady State Simulations

Numerical steady state simulations are run for the new USW reference rotor and the forward swept rotors. The flow rate values are kept same as per the experimental data.

Mesh Sequence	**Convergence Order, p**	**Estimated Value, f_e (Pa)**	**RDE, %**	**GCI, %**	
				Fine	**Coarse**
N1, N2, N3	2.64	66.89	0.21	0.27	0.33
N2, N3, N4	2.11	66.94	0.32	0.41	0.45

Table 6.2: Discretisation Error and Uncertainty Results

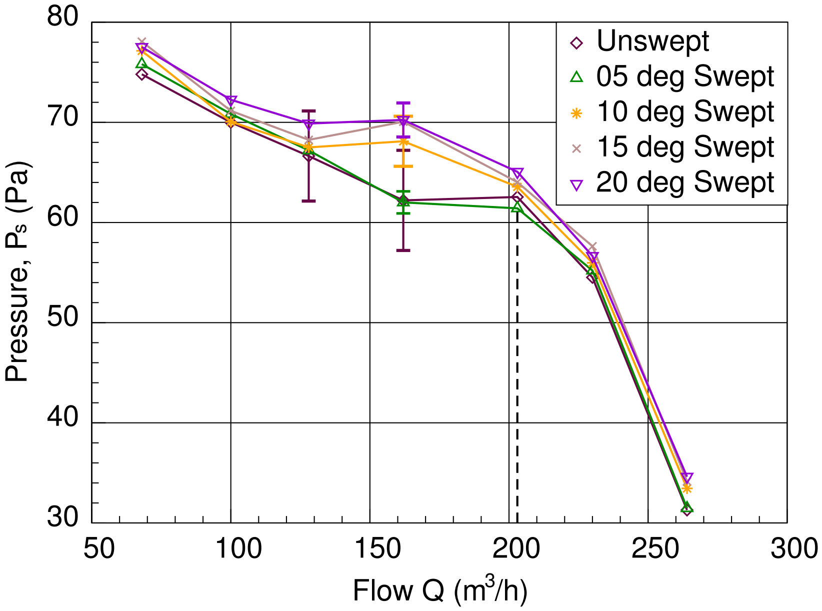

Figure 6.4: Static Pressure Rise vs. Flow Rate, Unswept and Swept Rotors

The characteristic curve and the numerical efficiency results obtained for the unswept and swept rotors are shown in Figure 6.4 and Figure 6.5 respectively.

Static pressure rise of the blower is one of the useful and important parameters for its overall performance evaluation. The characteristic curve shows shifting of pressure peak towards lower flow rate as the blade is swept forward in almost all cases which is in agreement with the results presented in [16] and [87]. The same is not true for the Rotor I (05 degree swept), which has shown similar behaviour as unswept rotor. However, it still has slightly higher static pressure values ($\sim 1\%$) than the unswept rotor at all flow rates except at BEP ($Q = 203$ m^3/hr). Considerable higher pressures are achieved for all the other swept blades as compared to unswept rotor.

The shifting of pressure peak means delay in flow separation, thus increase in the stable operating range of the rotor. The curve of the swept blades show relatively constant distribution in the steady working condition. It can be seen that at the off-design condition, when there is flow separation, the flow rates of unswept rotor and Rotor I are higher than those of other swept blades.

In case of Rotor III and Rotor IV, reduced pressure rise for Rotor IV has been observed at some flow rates. It can be supported by the fact that there occurs offloading at the swept rotor blade tip. The swept-bladed rotors generally realize reduced total pressure rise compared with unswept or less swept rotors, behaving as mentioned in [8] and [77]. The Rotors II and III, however, have not shown such kind of behaviour and generally have a smooth distribution of pressure values all over the range.

The total pressure efficiency (numerical efficiency) has been derived as the product of volume flow rate and area-averaged pressure rise in the testing chamber per power input.

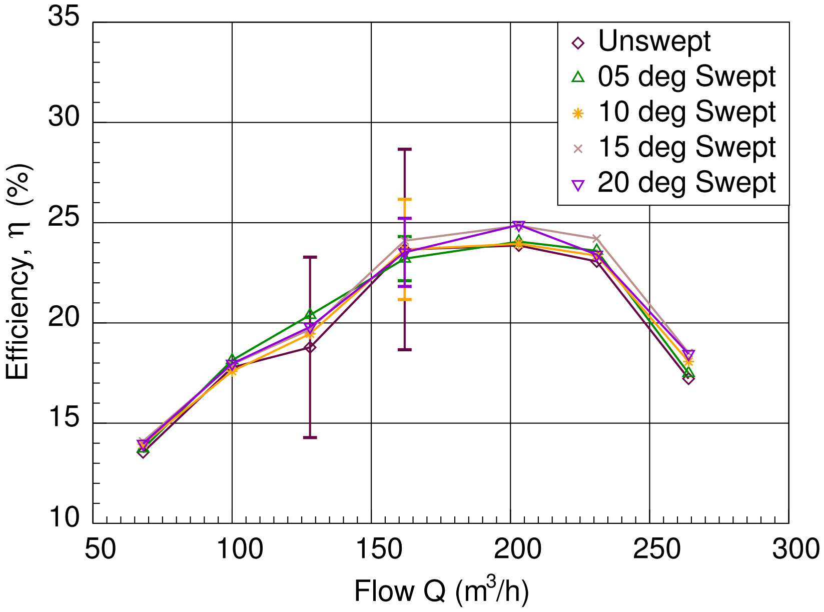

Figure 6.5: Total Pressure Efficiency, Unswept and Swept Rotors

Mathematically;

$$\eta = \frac{\Delta P \cdot Q}{M \cdot n} \cdot 100 \tag{6.1}$$

where,

- η : Total pressure efficiency $[\%]$
- M : Moment of rotor $[N \cdot m]$
- n : Rotational speed $[\frac{rev}{s}]$

The comparison of pressure efficiency for all combinations of blades (Figure 6.5) shows slightly higher efficiency trend. The advantage in the efficiency for the swept blade decreases near stall dip in case of Rotors II, III and IV. However, the maximum efficiency of Unswept rotor and Rotor I are comparable to the other rotors. This can be due to the fact that efficiency is based on total pressure characteristics of the blower and lower static pressure discourages the development of tip casing boundary layer, as described in [69].

6.2.2 Unsteady State Simulations

The characteristic curves for all the rotors show the unsteady effects at flow rates $Q = 128$ m^3/hr and $Q = 162$ m^3/hr. It seems that the flow is separated from most of the blade area at these points and thus caused unsteady effects. The numerical simulations are not properly converged due these unsteady effects, particularly at flow rate $Q = 162$ m^3/hr, in almost all cases, except for Rotor III. It is therefore decided to run unsteady simulations for these points only so as to get more realistic results and also to observe the possible 3D flow effects. The simulations are run for the unswept rotor and Rotor II as they have comparatively poor convergence. The results are obtained using unsteady Sliding Mesh

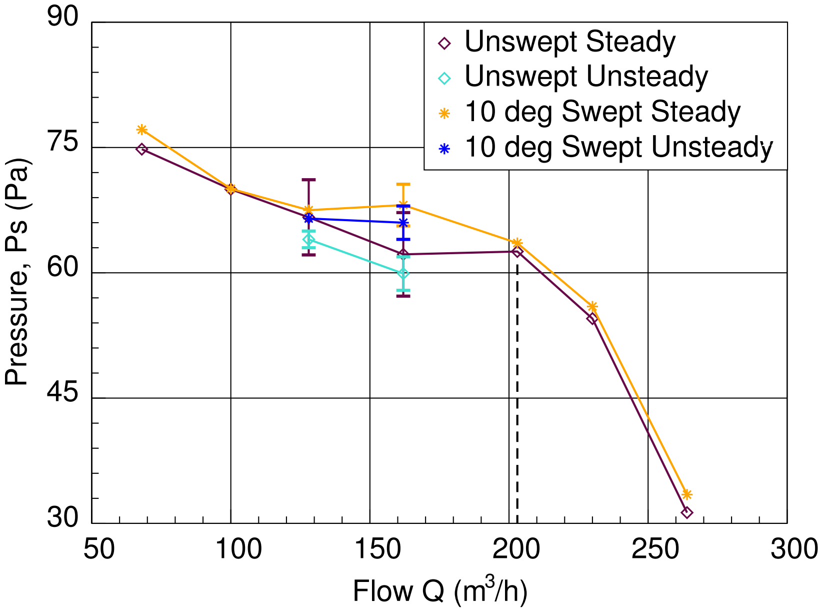

Figure 6.6: Comparison of USW and Rotor II: Unsteady Case

technique employing the same k-ω SST turbulence model. The results are shown as a comparison in Figure 6.6.

It is observed that there still exists the periodic convergence behaviour in the unsteady simulations. However, the results are better as there is less deviation of main outlet pressure values when compared with the steady state cases.

6.3 Flow Visualisation

The post-processing is carried out to get a better physical understanding of sweep effects on the flow field of all the rotors. The analysis starts with the description of steady state flow field within the rotors at the flow rate $Q = 203$ m^3/hr, as it turned out to be the BEP for all the test rotors. Flow behaviours of USW and rotor II are then compared for the flow rate $Q = 162$ m^3/hr as considerable change in the characteristic curve at this point is observed for 10 degree and higher sweep angles. The unsteady data is visualised for the same flow rate to capture the 3D flow effects undergoing through the flow field. The development of flow separation and stall formation on and inside the blade passage are resolved using EnSight® flow visualisation software. The observed effects of forward sweep are explained by pressure contours and discussed by comparing the relative velocity surface streamlines of the swept rotors with the unswept rotor. The analysis is focused on the streamlines of the suction and pressure sides of the blades and those at midspan and in the vicinity of the hub and casing. Radial velocity distributions are also analysed at the rotor outlet as well as at midspan, Near-tip and Near-hub sections.

6.3.1 Design Flow Rate: Steady State

6.3.1.1 Static Pressure Distribution

Static pressure distributions and contours for different surfaces and sections of all rotors are presented in Figures 6.7-6.14. They provide valuable information regarding the three dimensional nature of the blade boundary layer. The blade suction surface, where the sweep induces effects on the vorticity and static pressure field, has been recognised in a lot of previous studies as limiting the pressure rise and turning of the blade profiles [10, 15, 30, 32, 33, 48, 63, 66, 84].

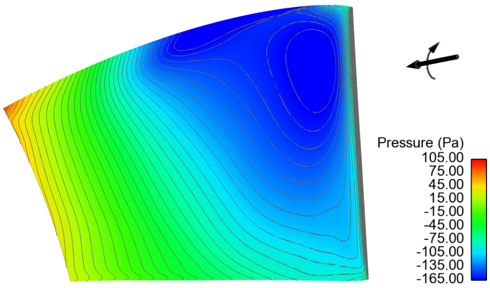

(a) USW

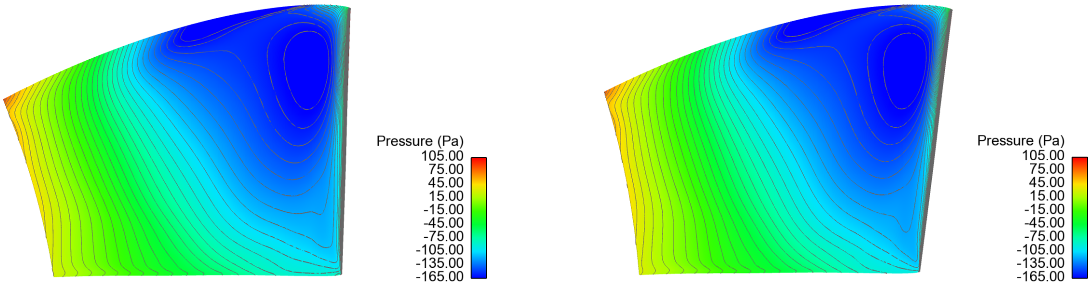

(b) Rotor I, $\lambda = 5°$

(c) Rotor II, $\lambda = 10°$

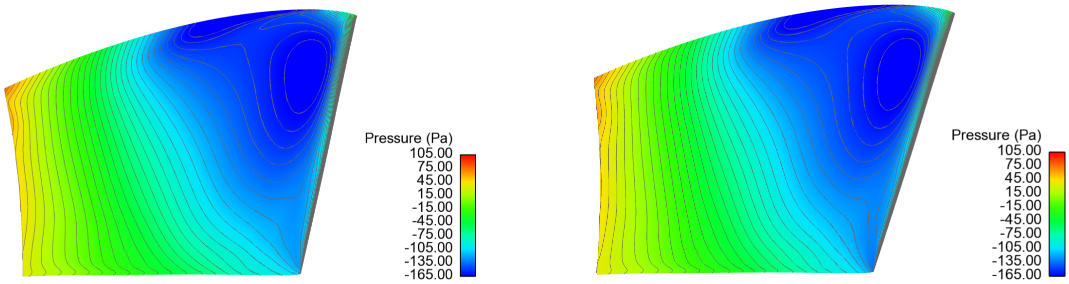

(d) Rotor III, $\lambda = 15°$

(e) Rotor IV, $\lambda = 20°$

Figure 6.7: Static Pressure Distribution: Suction Side

Figure 6.7 shows the isobars on the suction surface of the blades. The distribution of pressure is almost same for all the cases, implying that forward sweep has no significant effect on SS. The pressure contours on SS are inclined to the radial direction away from the leading edge. It indicates the tendency of the boundary layer (BL) flow towards the tip. For USW and Rotor I, the isobars near the trailing edge are parallel to trailing edge (Figs. 6.7(a) and 6.7(b)), which means relatively less BL flow towards tip. The contour lines are nearly radial for the other three blades close to the TE, indicating that the flow is in equilibrium with the radial pressure gradient. The isobars at the LE are found to be parallel to it showing a tendency of BL flow towards hub. It can be noticed that due to forward sweep, the isobars in this region are inclined more towards the upstream which shows the moderation of local radial outward flow with more inward guidance as compared to USW. A diffusion area exists near hub that starts just after the LE and extends in both directions (towards tip and TE) showing the separation of flow.

The isobars on the pressure surface of the blades are shown in Figure 6.8. High pressure gradient established close to the tip region extending from mid chord to the TE shows the existence of secondary flow in this portion. It attenuates the strength of the mechanism that primarily governs the leakage phenomena [80]. The pressure contours close to LE are parallel to the blade stacking lines thus leading to more radial flow moderation as the sweep angle increases. The isobars close to TE tend to be nearly radial with the forward sweep as a positive effect.

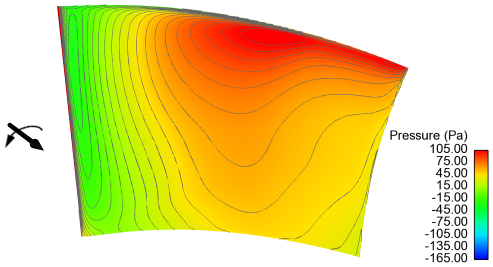

(a) USW

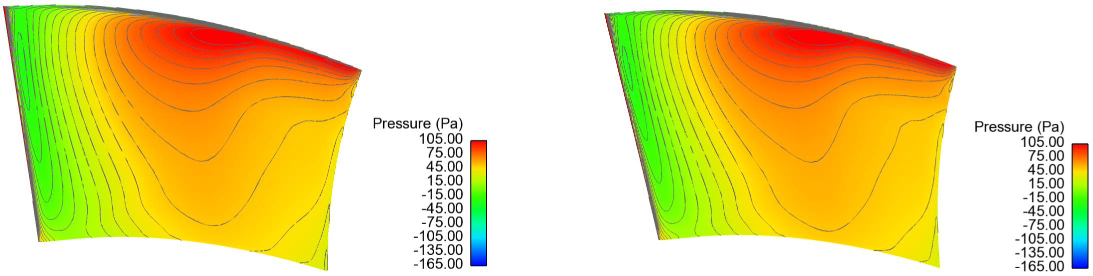

(b) Rotor I, $\lambda = 5°$ (c) Rotor II, $\lambda = 10°$

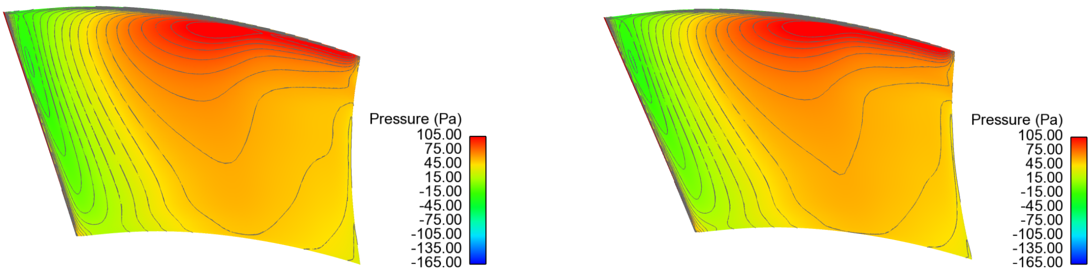

(d) Rotor III, $\lambda = 15°$ (e) Rotor IV, $\lambda = 20°$

Figure 6.8: Static Pressure Distribution: Pressure Side

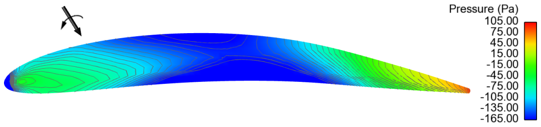

(a) USW

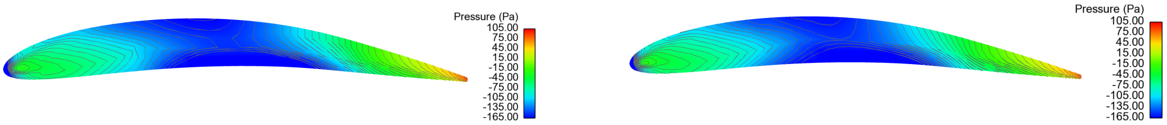

(b) Rotor I, $\lambda = 5°$ (c) Rotor II, $\lambda = 10°$

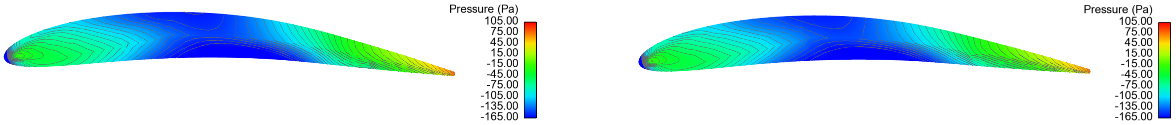

(d) Rotor III, $\lambda = 15°$ (e) Rotor IV, $\lambda = 20°$

Figure 6.9: Static Pressure Distribution: Tip

Rotor blade loading being a key feature deserves careful observation near and inside the tip gap. It is helpful in determining the onset of suction endwall flow separation and stall cell formation [47]. The local pressure difference between PS and SS near the tip also influences the extent of leakage and its velocity [66]. Tip surface static pressure distribution contours are plotted as in Figure 6.9.

The main common flow feature is the high skewing of the leakage flow trajectories, traced by the isobar trough and its decay after mid chord. It is worth noting that the leakage vortex develops close to the suction surface emerging with a small skew angle. The low static pressure trough seen on the rotor tip pressure distribution contours is caused by the leakage flow taking high curvature while entering the tip gap and forcibly spilling out to the other side through the gap. This is a "*thoroughfare zone*" for the tip leakage flow, at the end of which originates the leakage vortex [66]. From the tip gap entrance, the flow experiences contraction in the flow cross sectional area, hence the static pressure falls rapidly. This is related to vena-contracta. After this sudden contraction, the wall static pressure, going in-line with the tip surface static pressure distribution, started recovering from its minimum. Prior to the formation of leakage vortex (at the front portions of the chord), the pressures in either of the walls are deviating towards the tip gap exit. Sufficiently overlapped pressure distributions are observed towards the tip TE. All these phenomena are found to be qualitatively somewhat similar with swept rotors. The pressure troughs reduce in size for blades with higher sweep angles thus the loss due to mixing with the main flow after emerging out is reduced.

Figures 6.10 and 6.11 illustrate the computed distribution of static pressure and radial velocity at the outlet section of all the rotors. The general trend of higher pressure can be observed at higher radii. This is especially prominent above the midspan on suction side. Zone of low pressure is present adjacent to high pressure regions near the tip indicating the tip corner stall cells. A very low pressure zone can also be seen downstream of TE

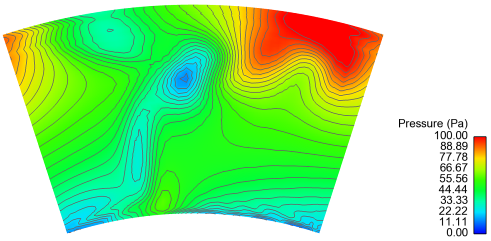

(a) USW

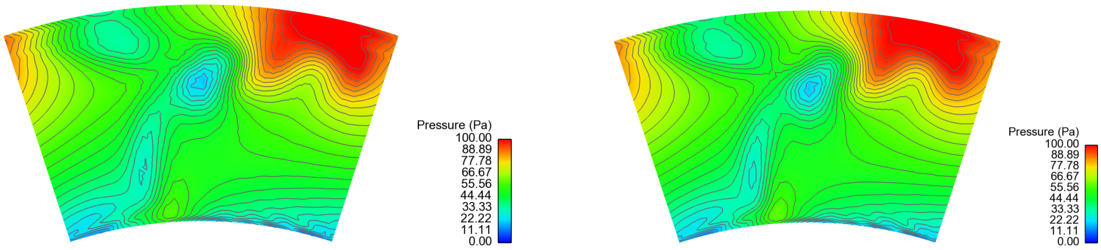

(b) Rotor I, $\lambda = 5°$ (c) Rotor II, $\lambda = 10°$

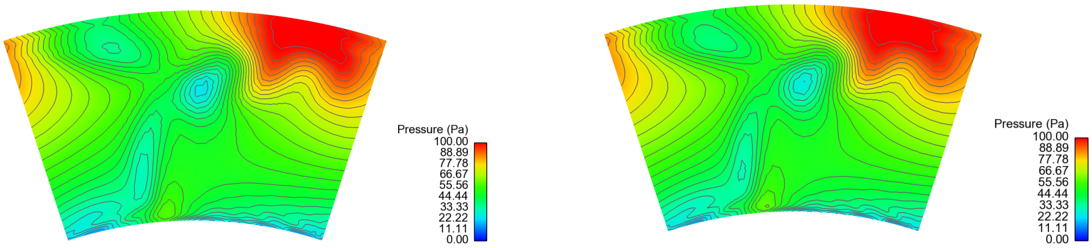

(d) Rotor III, $\lambda = 15°$ (e) Rotor IV, $\lambda = 20°$

Figure 6.10: Static Pressure Distribution: Rotor Outlet

slightly above midspan indicating vortex shedding from TE. A shift of these vortices towards SS has been noticed with the increase in the sweep angle. Similar behaviour has been shown in 6.11 with a relatively improved overall flow due to this shift. The rotors have significant radial velocity towards the tip on SS and towards the hub on the PS. This behaviour produces a secondary flow structure filling the whole blade passage. The pressure distribution of swept blades exerts an inward effect in the vicinity of the blade SS which is opposite to fluid motion driven by centrifugal forces. In this way a certain control on secondary flows is gained in the FSW rotor.

Figures 6.12, 6.13 and 6.14 show the static pressure distribution and contours plotted on pitchwise planes at three different radial locations named as Near-hub, midspan and Near-tip, respectively. The comparison of these pictures reveals a general trend of high loading near the tip and reduced pressure near the hub at LE. This result is not consistent with the findings of previous work carried out by a number of researchers [26, 32, 35, 71, 86], as according to them the negative/positive sweep increases/decreases the blade load near the endwall and shifts the blade load towards the LE/TE.

The pressure contours near the hub (Fig. 6.12) show that the forward sweep results in a low pressure region near the LE on the suction surface. The pressure recovery is significant

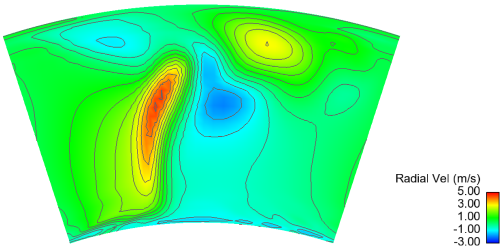

(a) USW

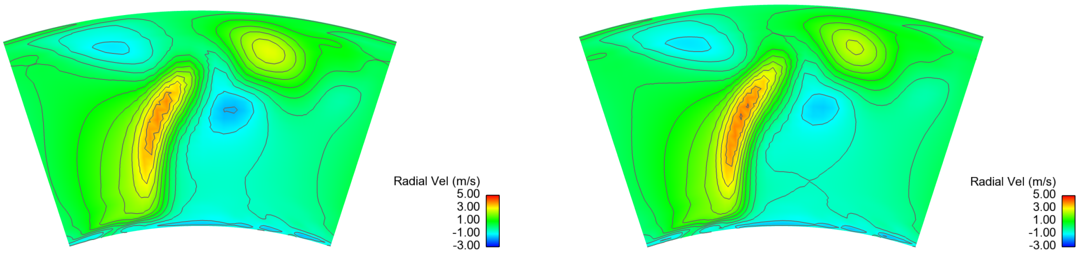

(b) Rotor I, $\lambda = 5°$ (c) Rotor II, $\lambda = 10°$

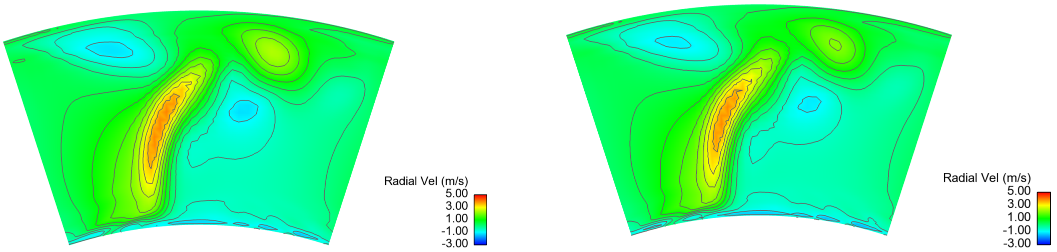

(d) Rotor III, $\lambda = 15°$ (e) Rotor IV, $\lambda = 20°$

Figure 6.11: Radial Velocity Distribution: Rotor Outlet

in FSW blades due to higher positive pressure gradient towards downstream. A relatively smooth pressure distribution is seen on the pressure surface near the hub with a positive pressure gradient. Towards the TE, the pressure distribution is almost same for all the rotors but with a slight increase in pressure values for FSW rotors.

At midspan section of USW (Fig. 6.13(a)), a zone of low pressure can be seen on the SS which extends near the LE up to the mid chord. The size of this low pressure zone reduces for blades with higher sweep angles as shown in Figures 6.13(d) and 6.13(e). Better pressure recovery has been noticed in case of FSW blades. The pressure distribution is again relatively smooth on the PS as the sweep angle is increased. The pressure values are higher near and after the TE for FSW blades. The same is true when compared with the near-hub sections.

The comparison of Near-tip sections shows almost same distribution of static pressure for all the rotors. The main feature is the generation of wake region on the SS which extends close to the TE of the adjacent blade. In case of Rotor III and IV, as shown in Figures 6.14(d) and 6.14(e), the wake zones have some elongation compared to the ones generated in other rotors. Also, slightly higher pressures are achieved as the sweep angle increases.

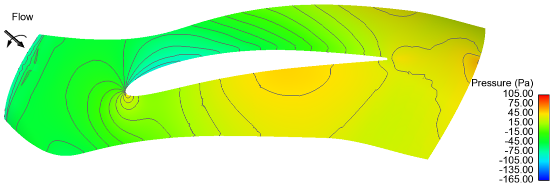

(a) USW

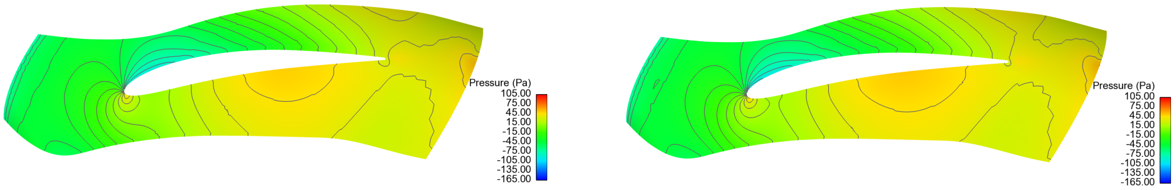

(b) Rotor I, $\lambda = 5°$ (c) Rotor II, $\lambda = 10°$

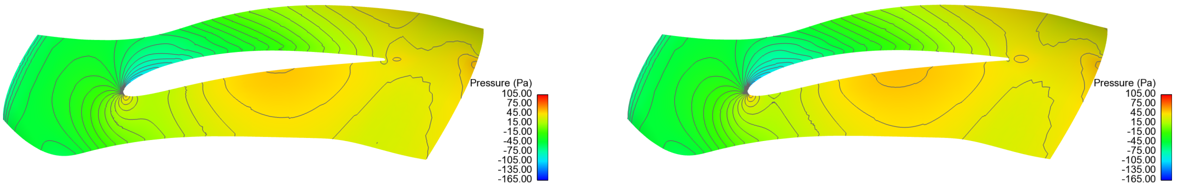

(d) Rotor III, $\lambda = 15°$ (e) Rotor IV, $\lambda = 20°$

Figure 6.12: Static Pressure Distribution: Near-hub Section

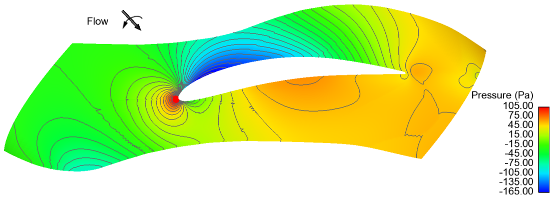

(a) USW

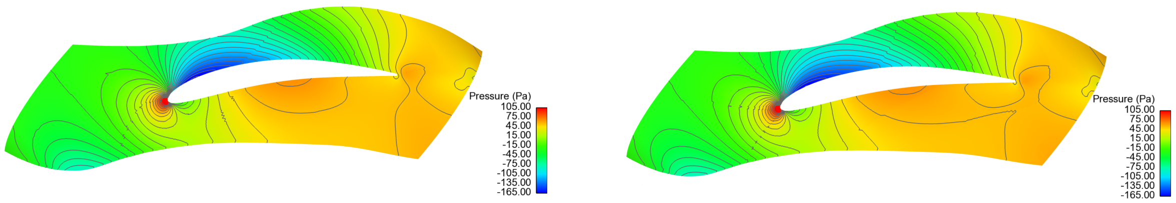

(b) Rotor I, $\lambda = 5°$ (c) Rotor II, $\lambda = 10°$

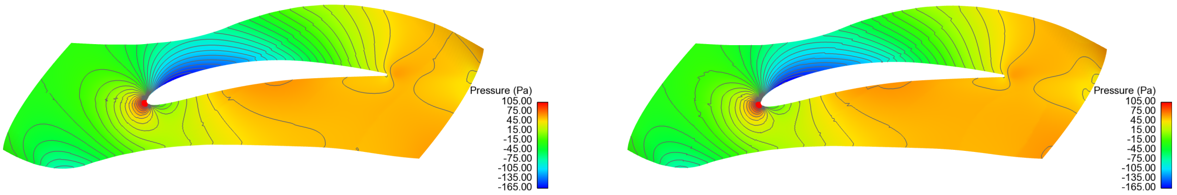

(d) Rotor III, $\lambda = 15°$ (e) Rotor IV, $\lambda = 20°$

Figure 6.13: Static Pressure Distribution: Midspan Section

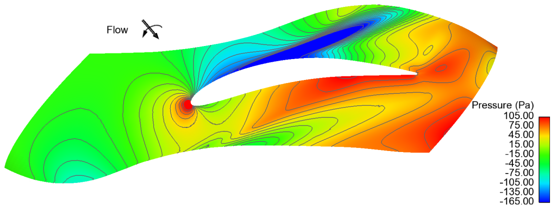

(a) USW

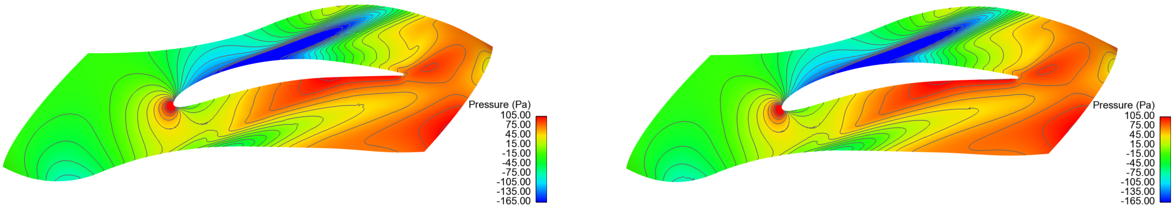

(b) Rotor I, $\lambda = 5°$ (c) Rotor II, $\lambda = 10°$

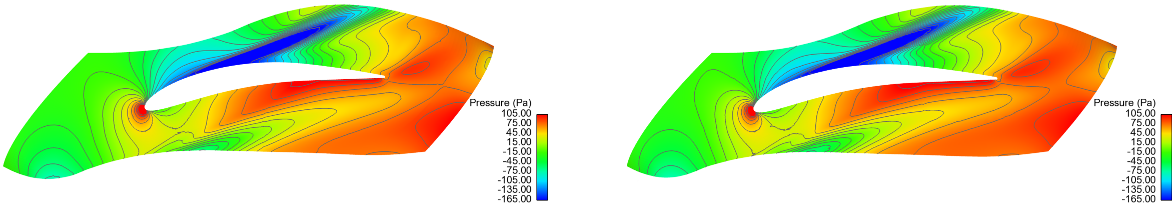

(d) Rotor III, $\lambda = 15°$ (e) Rotor IV, $\lambda = 20°$

Figure 6.14: Static Pressure Distribution: Near-tip Section

The overall pressure distribution depicts flow blockage caused by separation and vortex generation.

6.3.1.2 Surface Streamlines

The evolution of flow within the blade passage is analysed with respect to the fluid pattern close to the PS, SS and pitchwise radial sections by plotting the surface streamlines. For the swept rotors, it has been pointed out in the previous section that getting closer to the LE, the near-tip blade sections protrude into the upstream flow and carry out work on the fluid in advance compared with the blade sections near hub. Such effect is recognised for a FSW in references [46, 55, 87] and appears also for forward skewed tip rotor in reference [85]. Here, the main effects caused by sweep on the near-blade flow are discussed by visualising the behaviour of surface streamlines.

In figure 6.15, traced relative velocity streamlines on the suction surfaces of the various rotors are shown. The figure depicts the boundary layer migration phenomena and clearly shows that boundary layer fluid from various radial locations on the blade migrates towards the tip and accumulates at the tip mid-chord regions which later turns into tip corner stall cells. For more swept blades, this accumulation is reduced as the migratory boundary layer fluid is suppressed in the regions above the mid span, before reaching the tip to form the stall cells. Generally the radial outward flow result in an elongated

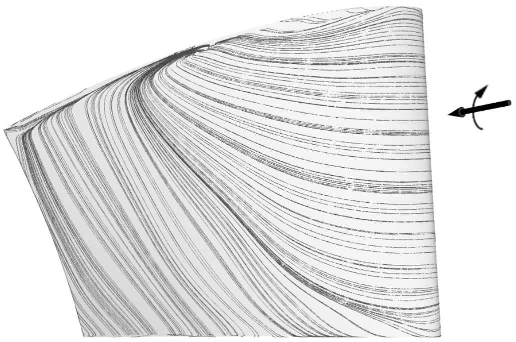

(a) USW

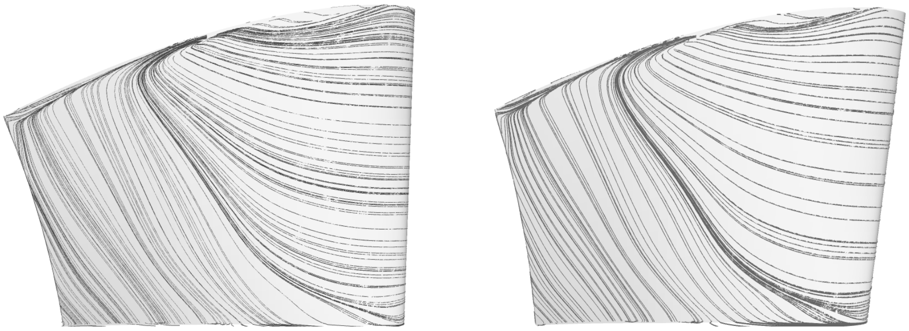

(b) Rotor I, $\lambda = 5°$

(c) Rotor II, $\lambda = 10°$

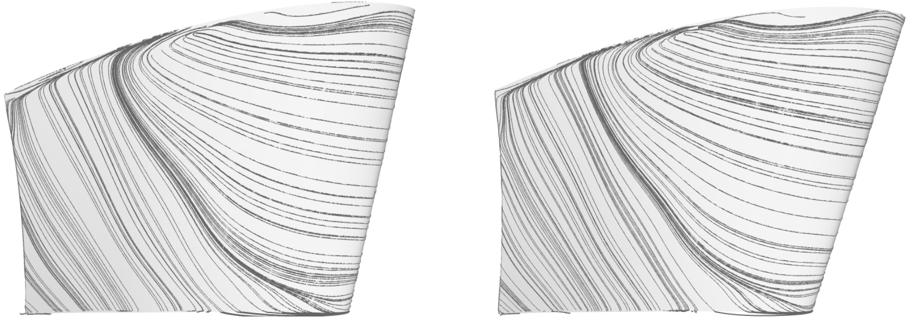

(d) Rotor III, $\lambda = 15°$

(e) Rotor IV, $\lambda = 20°$

Figure 6.15: Surface Streamlines: Suction Side

path of the fluid particles on the suction surface in the zone of adverse pressure gradient. The fluid particle path tends to be the longest near the hub on the LE of SS in the case of USW. As pointed out in reference [35], the longer path of the fluid particles on the suction surface results in the thickened BL since the wall friction becomes more effective. The thickening of suction surface BL increases the associated losses.

The corner stall flow pattern is present at all blades and evident at the tip. Corner stall is basically a result of the cross-passage flow driving the well-known classical passage vortex (PV) and washing up endwall boundary layer material up the suction surface.

Corner stall is linked to the presence of at least one three-dimensional separation line, at which the profile and endwall boundary layer interact and separate from the suction

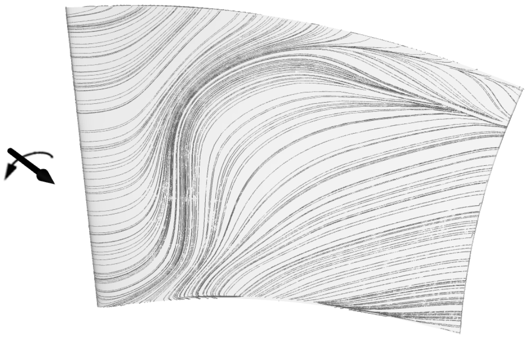

(a) USW

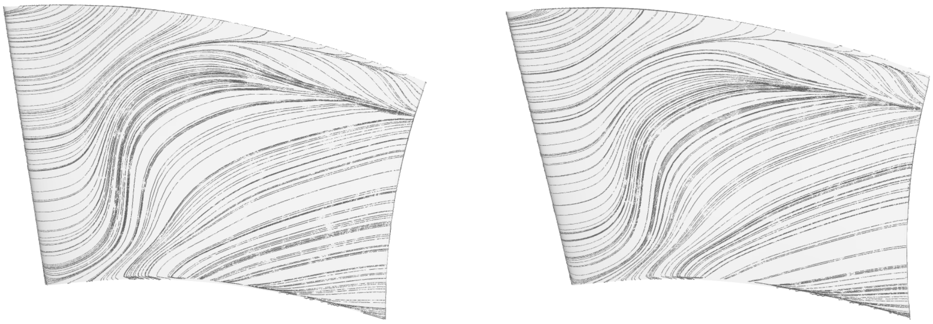

(b) Rotor I, $\lambda = 5°$

(c) Rotor II, $\lambda = 10°$

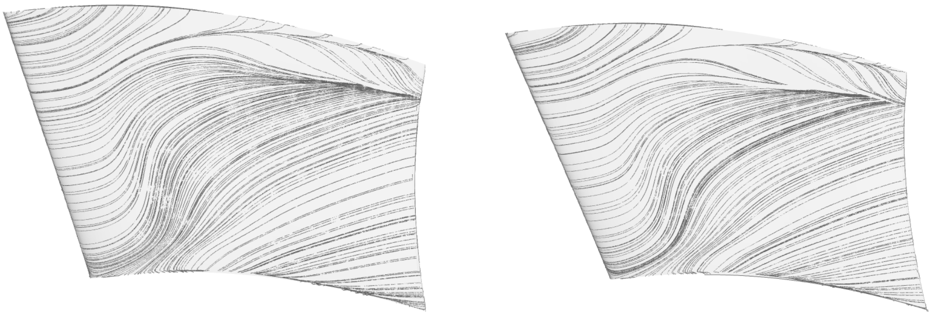

(d) Rotor III, $\lambda = 15°$

(e) Rotor IV, $\lambda = 20°$

Figure 6.16: Surface Streamlines: Pressure Side

surface. This does not necessarily require reverse flow. When the corner stall grows and gets more severe, a complicated pattern of three-dimensional separation lines, attachment lines and foci can occur. Reverse flow is likely to be involved in these cases [32].

The flow field of the USW features larger tip corner stall. At any condition the corner stall structure in the USW is more complex than in the FSW. This shows that the blade performance is limited by the flow phenomena occurring in the hub and tip regions. Looking at the corner stall pattern on the FSW, there is less tendency of the tip boundary layer material washing up the suction surface in the front portion where the sweep-induced PV delays cross-passage flow.

Figure 6.16 shows the surface streamlines on the PS of all the blades. The boundary layer flow varies more on PS as compared to that on SS, which is quite an unusual finding as in most of the literature it is the SS which undergoes severe changes with the sweep. The reason could be the unique geometry of the USW blade as it has a tapered hub with cylindrical casing (Section 5.3).

There is stronger radial migration of endwall boundary layer fluid in the front portion of the blade, where cross-passage pressure gradients are increased through the loading shift induced by the endwall potential effect of sweep. It is observed that flow turning in USW rotor below the mid span is quite higher. The flow accumulates above the mid span showing the tendency of USW rotor to deflect the flow towards the casing resulting in higher axial velocity in this region. The separation line that represents the envelope of the corner stall region builds a barrier to the approaching flow (involving significant local reverse flow). This behaviour is suppressed when the sweep angles are increased. This phenomenon resulted in higher pressure rise at higher radii, as the increased flow above the mid span together with low flow turning in these regions tend to minimize the secondary flows and wake related losses.

The Figure 6.16(a) shows that in case of USW blade, the flow acceleration close to the front region is normal to the endwall which moves the flow streamlines upward. Radial pressure gradient at this region, which is adverse in nature, causes the upward movement of the streamlines. Effect of sweep on the streamline shift is observed a little away from the front region. While USW rotor showed outward flow shift, FSW rotors showed gradual inward flow shifts. In FSW rotors, as the flow progresses into the blade passage, it is deflected away from the tip with high inward radial velocity. The separation lines on the PS of Rotor IV, Figure 6.16(e), are more in line with the main flow direction and therefore produce less blockage.

Figures 6.17-6.19 show the relative velocity surface streamlines and the distribution of radial velocity on near-hub, midspan and near-tip sections. More positive (outward) is the radial velocity, more is the flow towards the casing and opposite is the case with negative (inward) radial velocities. Slight variation is seen in respective rotors with high radial velocities at hub and decreasing towards the higher radii.

The radial velocity distribution near the hub (Fig. 6.17) shows that there is a radial outward flow away from the leading edge on the suction surface. Towards the trailing edge, a higher radial outward flow can be seen on the suction surface. However, for USW blade, this tendency is not maintained after the flow has left the blade but swept blades have followed it to some extent. An axisymmetric streamline flow is seen near the leading edge of all rotors, when the radial component of velocity is zero. An opposite behaviour is seen on the pressure surface near the hub, where a radial inward flow is initially seen close to the leading edge with forward sweep. Near the trailing edge, a slightly radial outward flow is noticed for the USW and FSW rotors on the PS. The 20 degree swept blade has the highest radial velocity in this region. However, the pattern of radial velocity at the rotor exit is nearly the same in all rotors on the PS of the blade. The streamlines show no separation of flow from the blades' surfaces in the near-hub section.

A similar observation can be seen at the midspan in Fig. 6.18. The radial outward flow is higher on the SS of FSW blades near the LE and mid-chord, as compared to USW blade. A zone of high radial velocity magnitude can be seen near the trailing edge on the suction surface for USW, indicating a thick boundary layer growth. With forward sweep,

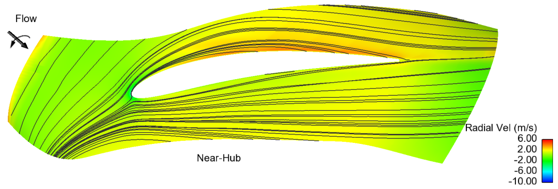

(a) USW

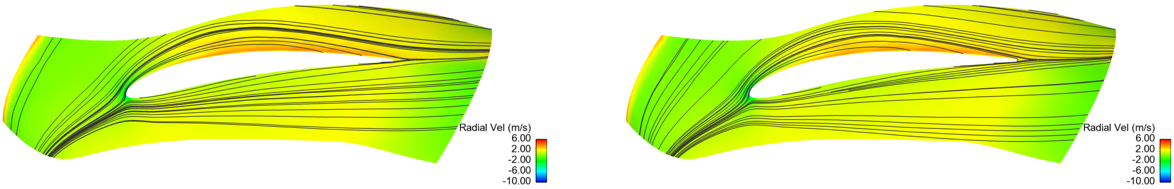

(b) Rotor I, $\lambda = 5°$ (c) Rotor II, $\lambda = 10°$

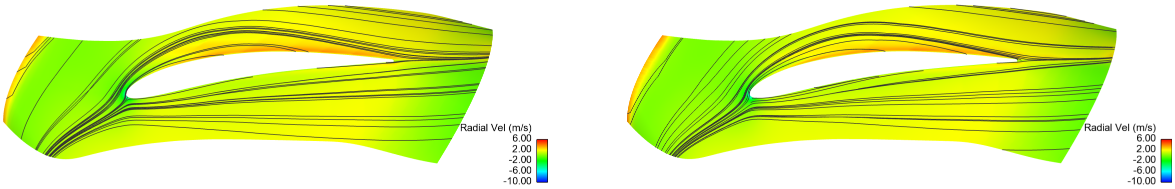

(d) Rotor III, $\lambda = 15°$ (e) Rotor IV, $\lambda = 20°$

Figure 6.17: Streamlines and Variation of Radial Velocity: Near-hub Section

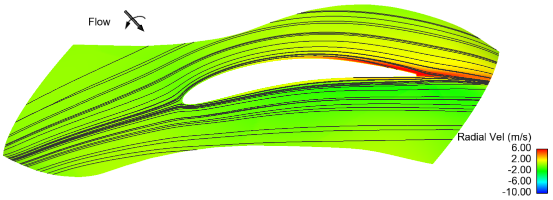

(a) USW

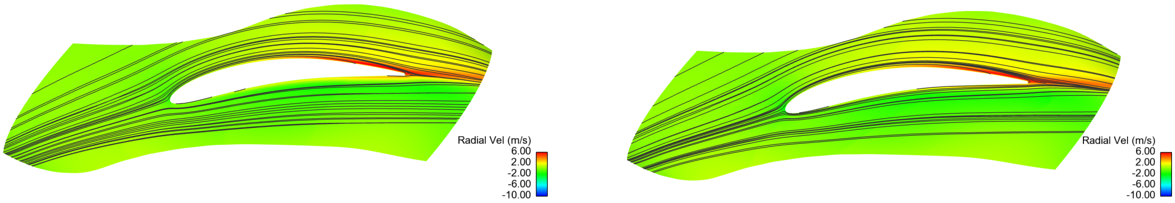

(b) Rotor I, $\lambda = 5°$ (c) Rotor II, $\lambda = 10°$

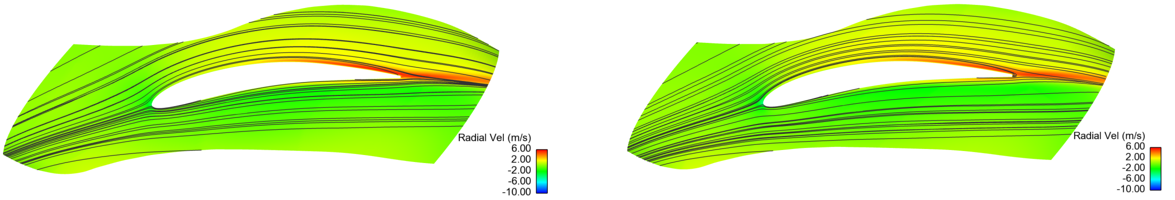

(d) Rotor III, $\lambda = 15°$ (e) Rotor IV, $\lambda = 20°$

Figure 6.18: Streamlines and Variation of Radial Velocity: Midspan Section

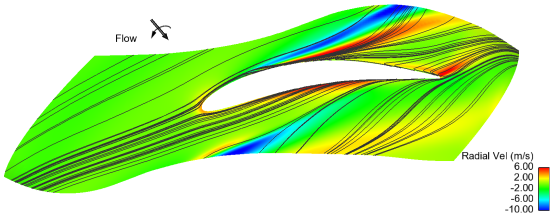

(a) USW

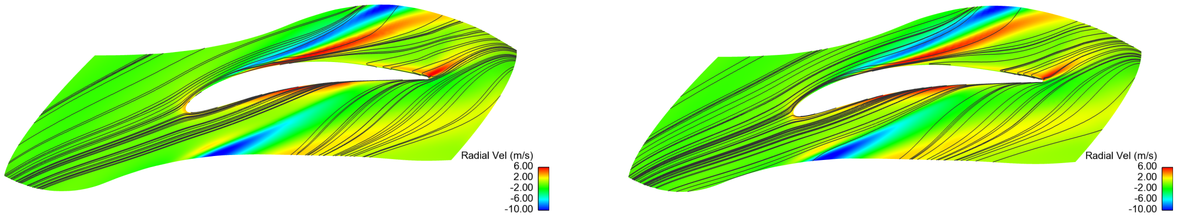

(b) Rotor I, $\lambda = 5°$

(c) Rotor II, $\lambda = 10°$

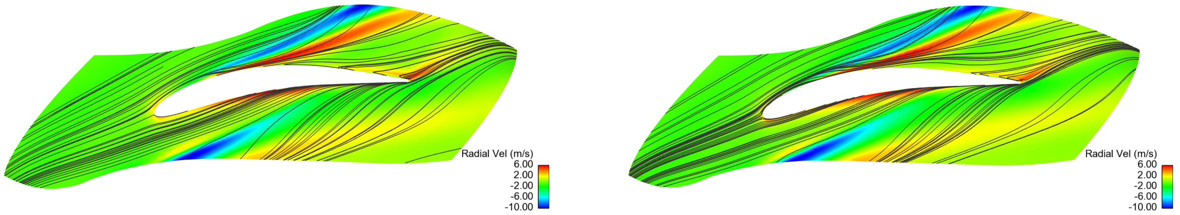

(d) Rotor III, $\lambda = 15°$

(e) Rotor IV, $\lambda = 20°$

Figure 6.19: Streamlines and Variation of Radial Velocity: Near-tip Section

relatively lower radial velocities are found in this region, indicating a reduction in the blade boundary layer shift towards the tip. As a general trend, the zone of high radial velocities appear to extend in the line of TE after leaving the blade for all the rotors. The radial velocity distribution is almost the same on the PS of all the blades. No twisting of streamlines is observed which indicates an attached flow to the blades.

In Fig. 6.19, the radial velocities and streamlines are shown for the near-tip section of all the rotors. Higher radial outward flow can be seen at the LE of the USW blade than that for the FSW blades in the same region. It indicates that less flow passes over the tip as the blade is swept forward. Since it is the leading edge at the tip which receives the incoming fluid first, energy transfer and hence blade loading starts at this location and results in a radial pressure gradient in addition to already existing spanwise pressure gradient and the blade force introduced by the blade sweep. This causes the flow streamlines in these rotors to undergo further deflections. The streamlines undergo twisting and the flow is separated near mid-chord on the SS. The twisting is more in case of USW blade while the separation seems to start earlier as the sweep is applied. Near the trailing edge, a similar behaviour has been observed as for midspan section i.e. a high radial velocity zone on the SS. The magnitude of radial velocity is again higher for USW blade than that for FSW blades. However, the zone disappears as the flow leaves the TE in all cases. Reversed flow has also been observed in this region for all the blades and is relatively more in case of USW blade. The flow has high radial velocity near mid-chord on the PS in all rotors, showing the crossflow through the tip gap. No significant difference can be noticed in the radial velocity and streamlines pattern on the PS of all the rotors.

6.3.1.3 3D-Flow Effects

It is a well-known fact that blade sweep introduces three-dimensionality into the fluid path lines in itself [46, 48, 77, 94], i.e. the streamlines on the SS and PS represent splitting and torsion of the incoming stream surfaces. Flow with large spanwise velocity causes the stream surfaces to undergo twisting. The spanwise direction of a swept blade is not perpendicular to the direction of flow and thus introduces additional radial blade force due to which streamlines acquire additional curvature. The curvature direction is different on SS and PS depending on the sweep type employed, as a result of which the original stream surface made under the assumption of radial equilibrium is twisted [65].

Figure 6.20 shows the streamlines released upstream region inside and close to the tip clearance. The streamline patterns in all rotors depict that the flow has strong helical motion and undergoes separation after being ejected from the SS of the respective blades. The primary objective of sweeping the blade is to prevent the centrifuged boundary layer flow on the rotor suction surface from getting accumulated near the casing. Natures of these separations, as modified by the blade sweep do not have much difference at BEP. It has been mentioned in the literature that the presence of three dimensional separations appears to be universal; and the challenge for the designer is to limit the loss and blockage produced. For well designed blade passages, the 3D separations may sometimes be small enough to ignore or overlook [28, 29]. It is clearly visible that in the case of USW rotor (Fig. 6.20(a)), the migration of boundary layer fluid from various radial locations on the blade towards the tip resulted in the flow separation from the blade in that region which finally turns out as tip corner stall. The same is true for swept rotors but the separation is slightly less vigorous as the sweep angle is increased.

The flow scenario in Figure 6.20 shows 3D velocity streamlines leaking through the tip gap owing to the local blade loading conditions. This leakage drops the pressures on the suction edge leading to higher pressure differentials. This process eventually stabilizes at certain leakage conditions, which are case specific. Streamlines crossing the tip gap through the low static pressure zone inside the tip have higher leakage velocity. They flow approximately tangentially near the blade mid-chord, where the pressure differentials between PS and SS are lowest on the tip. This figure confirms that tip leakage flow is fully 3D in nature, which is neither normal to the camber line [31], nor parallel to the rotation (tangential). The streamlines represent three-dimensional structures that are not constrained in the radial direction. The reverse flow generated from near mid-chord of the blade suction side is due to the rolling-up of tip leakage flow. The rolling-up of tip leakage flow is initiated near the position of the maximum static pressure difference (Fig. 6.7), which is located at approximately 30% chord downstream from the leading edge of the blade suction side.

As already stated in Section 6.3.1.2 with reference to Figure 6.14 that the relative velocity deficit region is observed to penetrate close to the TE of the adjacent blade, without crossing through its tip clearance region to cause what is known as “double-leakage”.

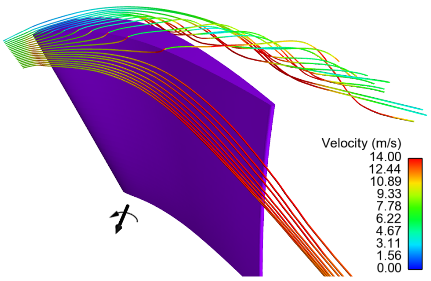
Velocity (m/s)
14.00
12.44
10.89
9.33
7.78
6.22
4.67
3.11
1.56
0.00

(a) USW

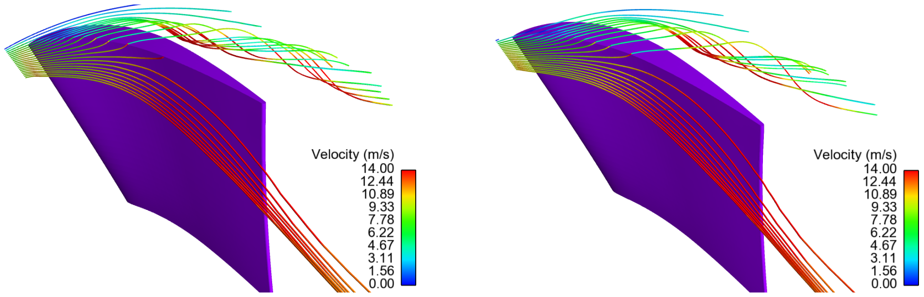
Velocity (m/s)
14.00
12.44
10.89
9.33
7.78
6.22
4.67
3.11
1.56
0.00
Velocity (m/s)
14.00
12.44
10.89
9.33
7.78
6.22
4.67
3.11
1.56
0.00

(b) Rotor I, $\lambda = 5°$ (c) Rotor II, $\lambda = 10°$

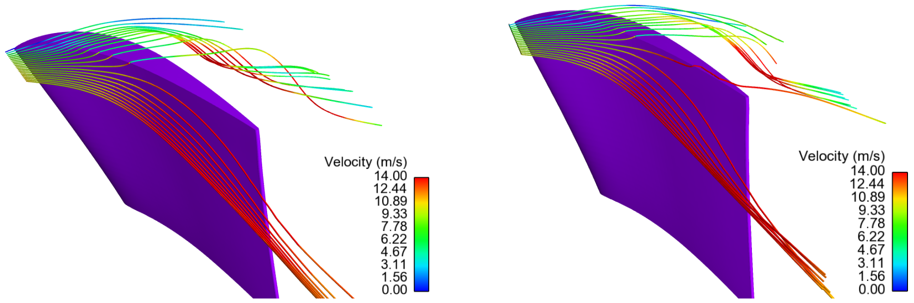
Velocity (m/s)
14.00
12.44
10.89
9.33
7.78
6.22
4.67
3.11
1.56
0.00
Velocity (m/s)
14.00
12.44
10.89
9.33
7.78
6.22
4.67
3.11
1.56
0.00

(d) Rotor III, $\lambda = 15°$ (e) Rotor IV, $\lambda = 20°$

Figure 6.20: 3D Streamlines through Tip Gap

Double leakage refers to tip clearance flow leaking across the adjacent blade tip again but with a lower streamwise velocity component [76] and this has not occurred for any case. In all the blade configurations shown, due to higher blade loading conditions, the leakage flow quickly tends to roll-up into vortex resulting in early portion of the tip chord subjected to lower pressure troughs where a strong vortex is originated.

6.3.1.4 Lambda$_2$ Method

Generation of vortices are tracked using the Lambda$_2$ method proposed by Jeong and Hussain [41]. The method is one of the most common ways of detecting vortices [73] and is based on the assumption of low pressure inside vortical structures [72].

According to this method, a vortex in an incompressible flow is defined in terms of the eigenvalues of the symmetric tensor $\mathbf{S^2} + \mathbf{\Omega^2}$; where $\mathbf{S}$ and $\mathbf{\Omega}$ are the symmetric and antisymmetric parts of the velocity gradient tensor $\nabla\mathbf{v}$, respectively. This definition cap-

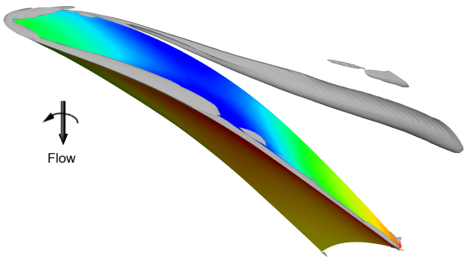

(a) USW

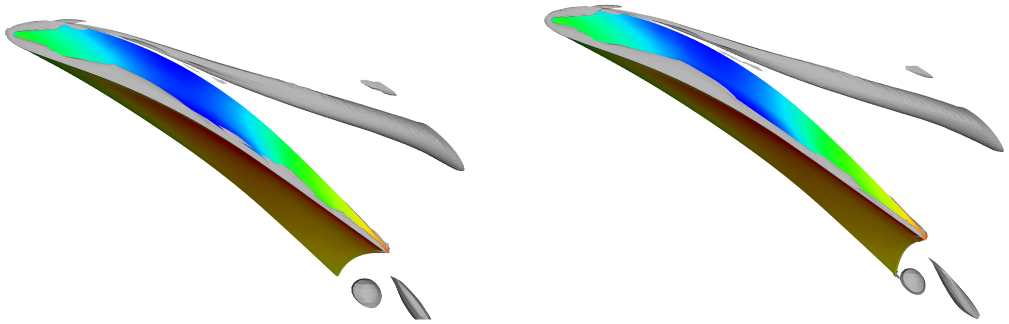

(b) Rotor I, $\lambda = 5°$ (c) Rotor II, $\lambda = 10°$

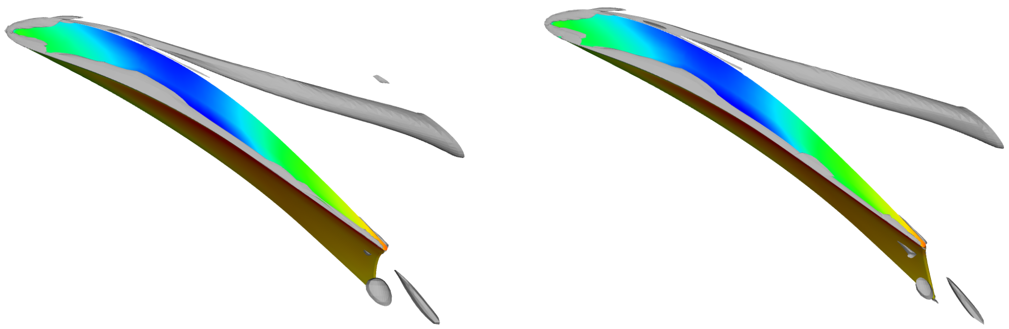

(d) Rotor III, $\lambda = 15°$ (e) Rotor IV, $\lambda = 20°$

Figure 6.21: Vortex Structure; Lambda$_2$ Method

tures the pressure minimum in a plane perpendicular to the vortex axis at high Reynolds numbers, and also accurately defines vortex cores at low Reynolds numbers [41]. A vortex region is present when two of the three eigenvalues are negative. As the name of the method implies, only the second eigenvalue is used for the visualization. The vortex strength increases as the negative λ_2 value decreases. The Lambda$_2$ method only determines vortical regions by disregarding components that might lead to inaccuracies between the existence of a pressure minimum and the existence of a vortex. Galilean invariance is retained, i.e., the Lambda$_2$ method delivers identical solutions even when a constant vector is added to the vector field. This is quite important when different reference frames are used [72]. However, in situations where several vortices exist, it can be difficult for this method to distinguish between individual vortices [42, 73].

In Figure 6.21, three-dimensional structures of the tip leakage vortex (TLV) for all rotors are shown. The TLV originates near the leading edge from interaction between the incoming flow and flow coming over the blade tip. As the blade loading increases, the pressure gradient over the tip increases and the tip vortex moves further away from the blade SS in the circumferential direction after formation near the leading edge. It can be seen that the TLV gets stronger as the flow proceeds downstream. However, due to the strong interaction with the through-flow near the PS of the adjacent blade, it finally diffuses. It is observed that these vortices are maintained and so-called vortex breakdown is not observed in any rotor flow passage. The locus of TLV center is also nearly same regardless of forward sweep. For higher sweep angles, however, TLV has slight radial inward inclination alongwith the circumferentially away movement.

The rolling vortex is a source of flow blockage in the upstream portions of the passage resulting in slightly increased incidence. The TLV in all rotors penetrated into the passage, as already discussed, almost till the TE of the adjacent blade but there is no significant difference for deciding higher blockage among the various rotor configurations at BEP.

6.3.2 Near-Stall: Steady State

In this section, the results obtained from the steady state simulations carried out at Near-Stall condition ($Q = 164$ m^3/hr) are discussed. As mentioned earlier in section 6.3, only two rotors, USW and Rotor II, have been considered for the analysis at Near-Stall. The main objective of this reduced flow rate analysis is to understand the flow streamline pattern on/around the blade and the vortex behaviour leading to blower stall.

6.3.2.1 Surface Streamlines

The relative velocity streamline traces on the SS and PS surfaces of the two rotors are shown in Figures 6.22 and 6.23, respectively. The boundary layer fluid has a general behaviour of outward radial flow, however, the stall behaviour is different in both cases. The corner stall structures of greater complexity are noticed on both rotors as compared to the those observed at BEP.

Figure 6.22(a) shows that in case of USW, the fluid on SS tends to migrate towards the tip but is suppressed before reaching the tip due to flow separation in the regions above mid span. In particular, large flow separation originating from the tip LE of the blade is observed. The separation extends almost up to the full tip length. It is noted that the separated flow is more complex as it moves downstream. The USW is also affected by small separation that originated near the hub LE. The downstream configuration of low-energy separated flow results in a radial outward streamline path, as traced by the reattachment line. The reattachment line changes its direction from radial outward to axial at about 75% chord length above mid span and the streamlines accumulate at the tip TE resulting in the tip corner stall. Concerning the Rotor II, Figure 6.22(b) shows that the streamlines on the SS are relatively axisymmetric than those observed for USW. The flow separation can be seen originating downstream of the tip LE and seems to continue up to the 75% chord length. This behaviour allowed the streamlines to reach up to the blade tip featuring a reverse flow path or tip corner stall in that region. However, the same behaviour depicts less distortion in the flow pattern and supports the ability of Rotor II to work better at the higher radii as compared to USW. There is also a separated flow

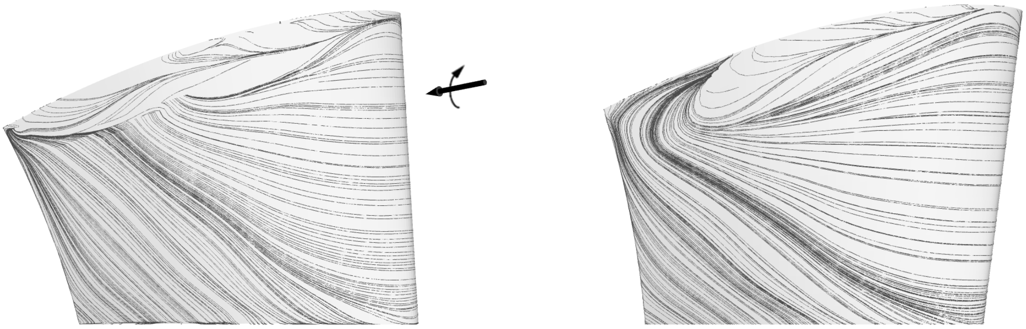
(a) USW (b) Rotor II, $\lambda = 10°$

Figure 6.22: Surface Streamlines near Stall Condition, Steady Case: Suction Side

region at the hub which has originated near the mid-chord unlike USW. The attachment line is shifted more towards downstream for Rotor II. The 10 degree forward swept blade thus behaved such that the hub stall onset is delayed.

It is well known that the separation on the blade suction surface deteriorates the performance of a turbomachinery. The larger separation in case of USW resulted in lower pressure rise at near-stall. It should be noted that the movement of the attachment line to the downstream on the blade suction surface can result in the increase in total pressure efficiency of the FSW. These behaviours justify somehow the sudden change in the behaviour of the characteristic curves of these rotors at near-stall in Figure 6.5.

Figure 6.23(a) shows the time-averaged flow close to the PS of USW rotor. There is a strong radial outward flow in the front portion of the blade thus indicating secondary flow. Further inspection shows a weak tip corner stall near the LE which may have occurred due to the distortion of the vortex filament of the inlet boundary layer passing with the flow through a curved passage [75]. The flow separation at about 25% chord length is also observed near hub endwall. In the rear portion of the blade, the streamlines tend to follow axisymmetric pattern of the attachment line, showing no significant flow blockage. However, the flow leakage at the tip can be seen before mid-chord resulting in the tip corner stall on the SS. Figure 6.23(b) gives an overview of the streamlines pattern on the PS of Rotor II. A strong tip corner stall downstream LE appears to be a prominent feature. The reverse flow in this region results in more flow leakage through tip. The radial outward boundary layer flow is not strong in this case and the streamlines are more in line with the main flow direction thus causing less overall blockage. A weak stall region is also present near the hub but has no significant effect on the flow pattern.

6.3.2.2 3D-Flow Effects

Figures 6.24 and 6.25 show the 3D streamlines and vortex structures developed for USW and Rotor II at near-stall, respectively. The behaviour of these features confirms the presence of unsteady flow effects at the stall condition.

The comparison of Figures 6.24(a) and 6.24(b) points out a general trend of 3D relative velocity streamlines leaking through the tip gap near mid-chord. Most of the leakage flow

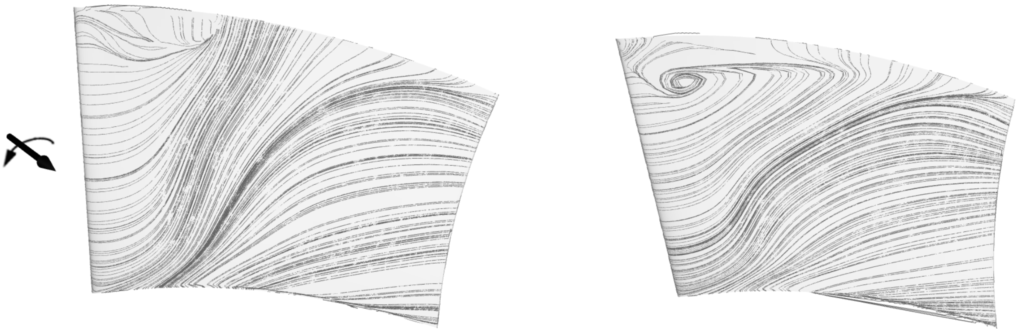

(a) USW (b) Rotor II, λ = 10°

Figure 6.23: Surface Streamlines near Stall Condition, Steady Case: Pressure Side

exits the clearance gap with a negative axial velocity component creating vortex related flow blockage. The velocities of these 3D streamlines crossing the tip gap are highest and therefore interacts more severely with the main flow on the SS of the blade passage. The flow is separated near the tip LE of both rotors. The uniform strong helical motion of the 3D streamlines on the SS as observed at BEP is not present anymore and the unsteady effects are more prominent. It is noted that the blockage is larger for USW on the SS as compared to Rotor II, as can be distinguished by strong swirling of 3D streamlines.

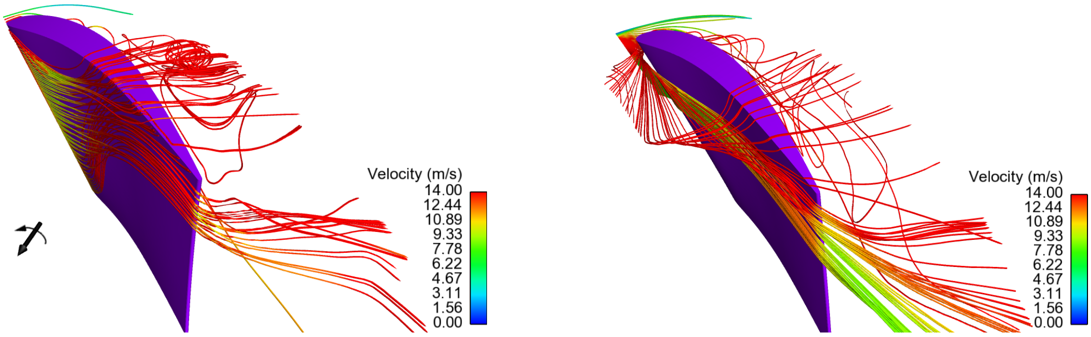

(a) USW (b) Rotor II, λ = 10°

Figure 6.24: 3D Streamlines, Steady Case: Near Stall Condition

A similar unsteady behaviour is observed in Figures 6.25(a) and 6.25(b) showing the vortex structures in the flow passages of the two rotors. In case of USW, a large vortex originates downstream the LE on PS and spreads circumferentially as well as towards the TE. On the SS, the tip leakage vortex originates near the LE and moves away from the suction surface while getting stronger in the flow direction and finally leading to the “vortex breakdown”. The stall cells are found to propagate in the direction opposite to the blade rotation. The strong distortion of the flow due to vortex shedding continues while a large blockage is also formed near the TE. It has been indicated in various previous studies [34, 38, 44, 95] that tip clearance vortex breakdown occurs when the tip clearance vortex interacts with the passage shock at near-stall conditions. It was indirectly implied that vortex breakdown causes stall inception in these investigations on transonic flow in a radially stacked rotor. The Rotor II experiences a large circulation in front of LE which

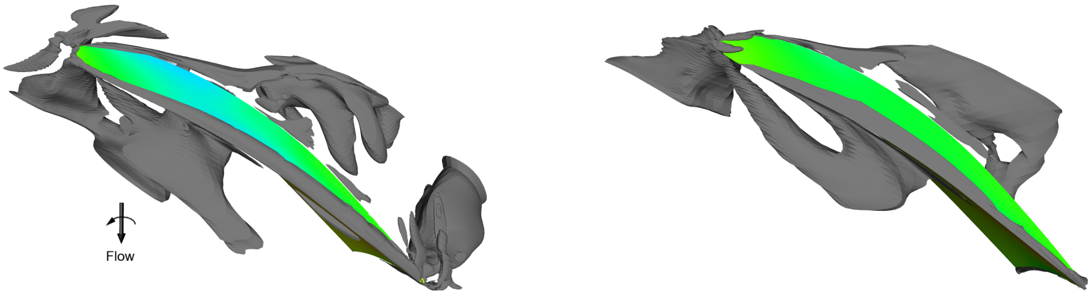

(a) USW, Steady (b) Rotor II, $\lambda = 10°$, Steady

Figure 6.25: Vortex Structure, Steady Case: Near Stall Condition

caused circulation of the fluid and the absence of through flow in this region. The PVs are also developed on both sides of the blade with increasing strength downstream. However, the vortex breakdown is less severe in Rotor II as compared to USW indicating less flow blockage in the blade passage.

6.3.3 Near-Stall: Unsteady

In the previous sections, the results discussed are based on the steady simulations thus any unsteady effect on the flow field is suppressed. In this respect, it is not sure that the flow pattern represents either the time-mean or the instantaneous flow actually occurring. It is well known that the flow interaction between the tip leakage vortex and the main flow is inherently unsteady at stall and near-stall conditions and the flow becomes highly oscillatory [24, 34, 38, 50, 54, 95]. The main purpose of this unsteady investigation is to advance the current understanding of the flow field near the blade tip and within the blade passage at near-stall condition for both the considered USW and FSW rotors. The variations in pressure distribution and limiting streamlines pattern on the suction surface for the unsteady flow field are discussed. Moreover, the instantaneous 3D streamlines and vortex structures are visualised and described as a main part of this section. The analysis covers five nondimensional times after several transient period of calculation. These are $t/T_{pp} = 0$, $t/T_{pp} = 0.2$, $t/T_{pp} = 0.4$, $t/T_{pp} = 0.6$ and $t/T_{pp} = 0.8$, where T_{pp} is the passage-to-passage time period.

Figure 6.26 shows the time-resolved unsteady distribution of static pressure and surface streamlines on SS of USW and Rotor II at the near-stall condition. The USW and Rotor II are separated in left and right columns respectively. It is important to mention that from one subfigure to the next (vertically) in each column, the blade moves 7.2 degrees, which corresponds to 1/5 of the blade passage passing period T_{pp}. The same applies for the other upcoming figures of this section.

Considering the USW rotor, the radial pressure gradient near the hub LE causes the BL flow to migrate towards tip. Near mid-chord and close to the tip, adverse pressure gradients occur with time. The variation of the surface streamlines show that there are lines of separation and attachment near LE at hub. The location and type of these lines do not vary much with time. At 80% blade span, however, the topology of the these streamlines

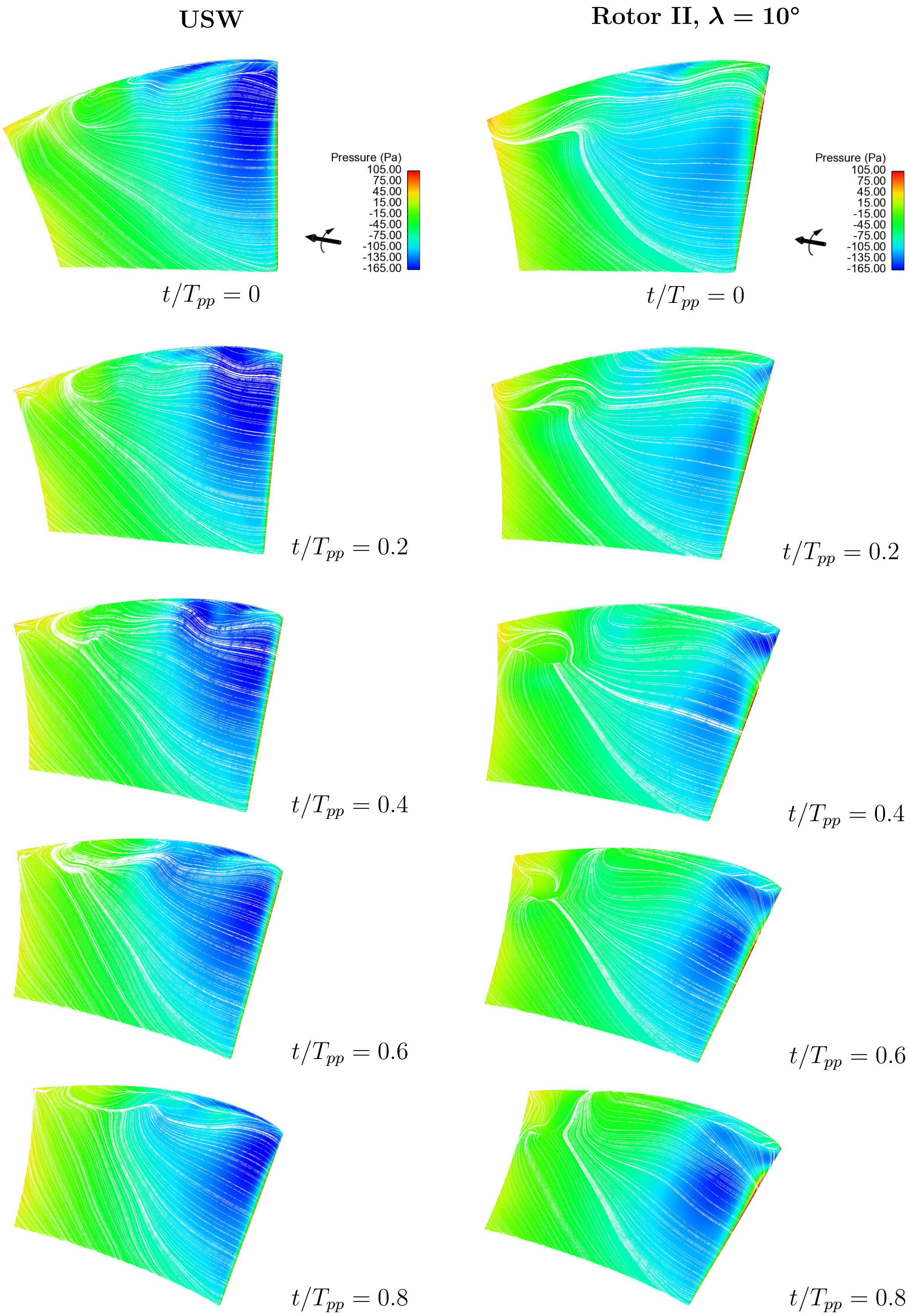
USW
Rotor II, $\lambda = 10°$
Pressure (Pa)
105.00
75.00
45.00
15.00
-15.00
-45.00
-75.00
-105.00
-135.00
-165.00
Pressure (Pa)
105.00
75.00
45.00
15.00
-15.00
-45.00
-75.00
-105.00
-135.00
-165.00

$t/T_{pp} = 0$ $t/T_{pp} = 0$

$t/T_{pp} = 0.2$ $t/T_{pp} = 0.2$

$t/T_{pp} = 0.4$ $t/T_{pp} = 0.4$

$t/T_{pp} = 0.6$ $t/T_{pp} = 0.6$

$t/T_{pp} = 0.8$ $t/T_{pp} = 0.8$

Figure 6.26: Static Pressure Distribution and Surface Streamlines on SS at Selected Times

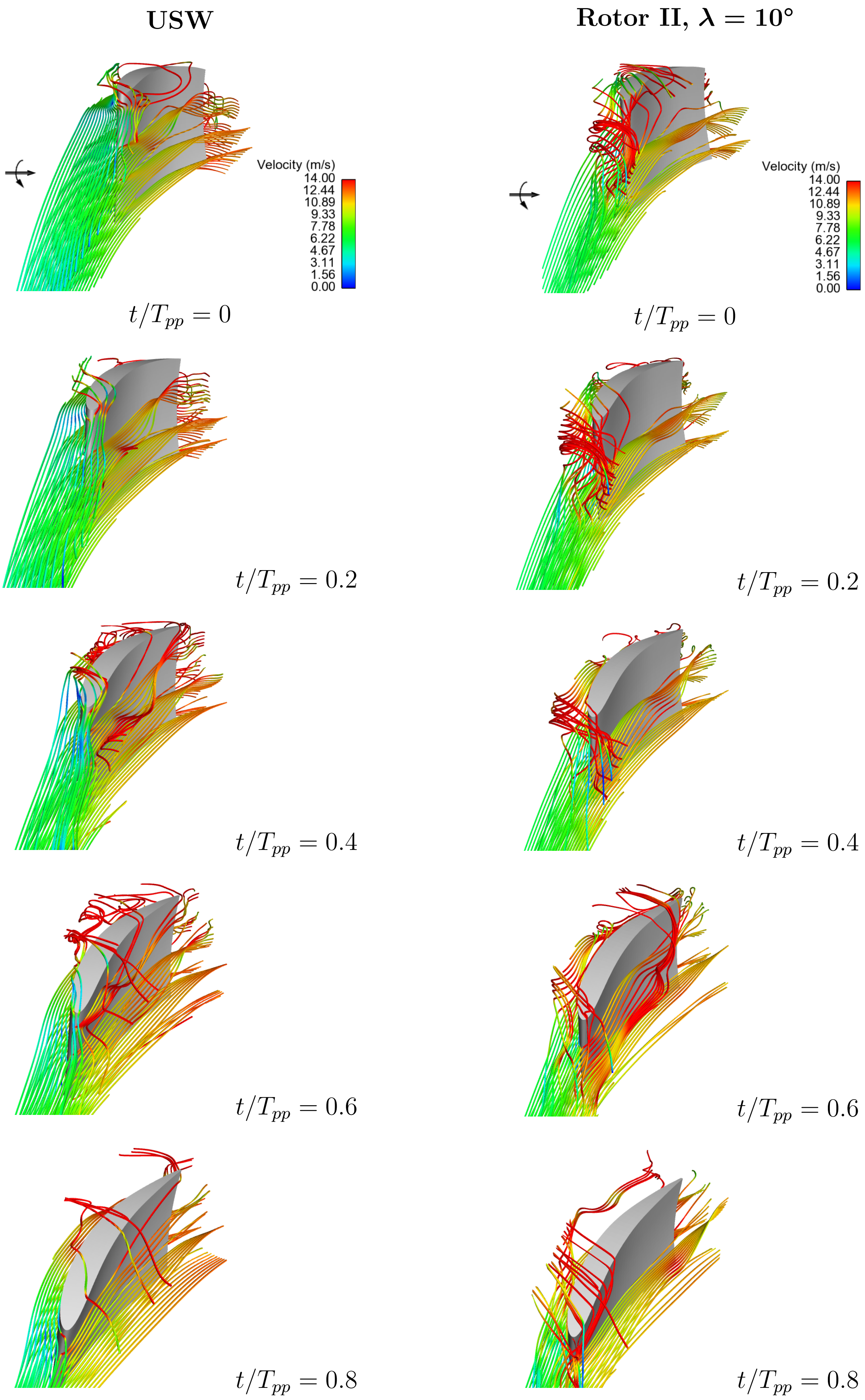
USW
Rotor II, $\lambda = 10°$
Velocity (m/s)
14.00
12.44
10.89
9.33
7.78
6.22
4.67
3.11
1.56
0.00
Velocity (m/s)
14.00
12.44
10.89
9.33
7.78
6.22
4.67
3.11
1.56
0.00

$t/T_{pp} = 0$ $t/T_{pp} = 0$

$t/T_{pp} = 0.2$ $t/T_{pp} = 0.2$

$t/T_{pp} = 0.4$ $t/T_{pp} = 0.4$

$t/T_{pp} = 0.6$ $t/T_{pp} = 0.6$

$t/T_{pp} = 0.8$ $t/T_{pp} = 0.8$

Figure 6.27: Unsteady 3D Streamlines through the Blade Passage

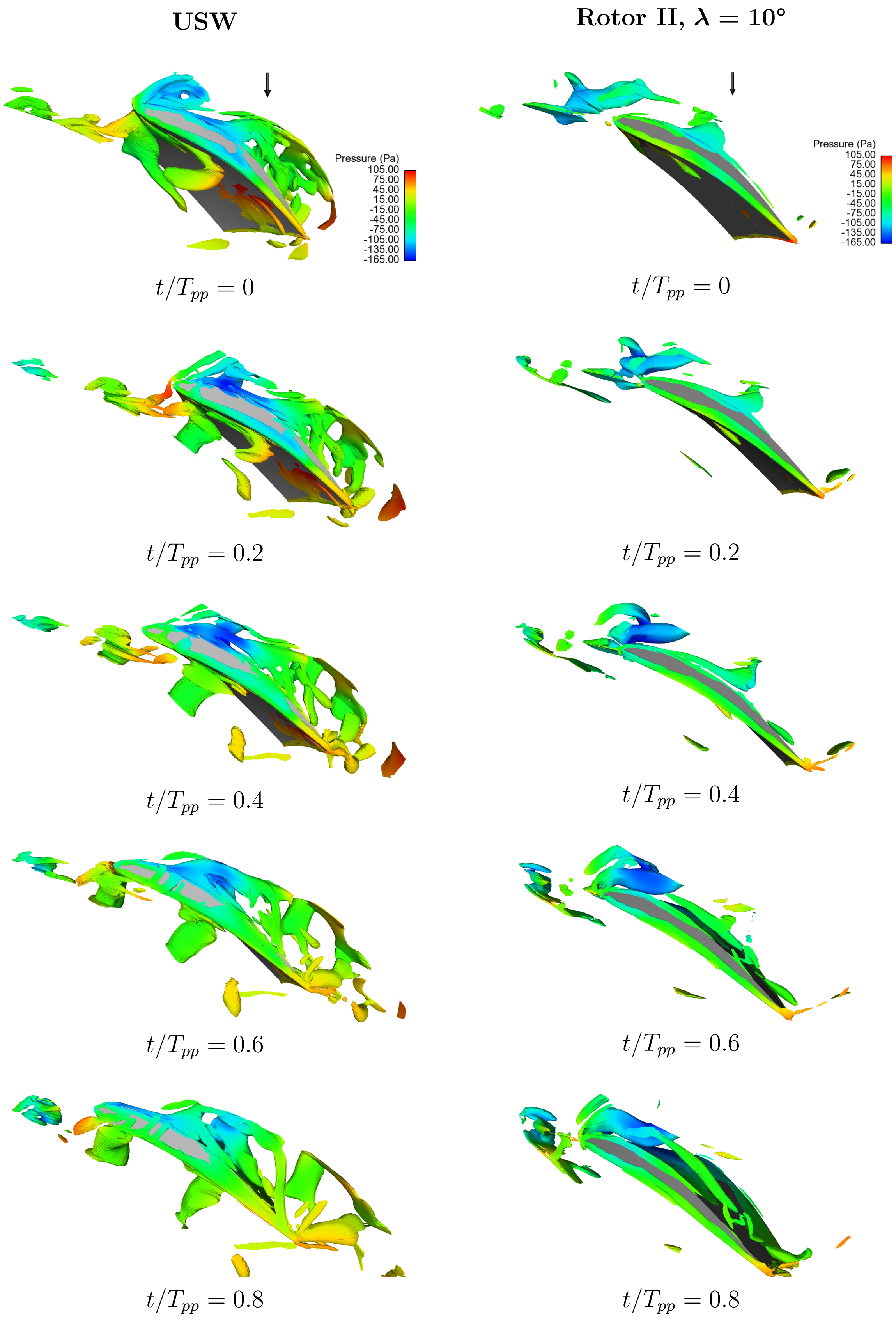

USW

Rotor II, $\lambda = 10°$

$t/T_{pp} = 0$ $t/T_{pp} = 0$

$t/T_{pp} = 0.2$ $t/T_{pp} = 0.2$

$t/T_{pp} = 0.4$ $t/T_{pp} = 0.4$

$t/T_{pp} = 0.6$ $t/T_{pp} = 0.6$

$t/T_{pp} = 0.8$ $t/T_{pp} = 0.8$

Pressure (Pa)
105.00
75.00
45.00
15.00
-15.00
-45.00
-75.00
-105.00
-135.00
-165.00

Figure 6.28: Instantaneous λ_2 Surfaces

changes with time. The focal point, which indicates three-dimensional attachment represented by circular and spiral flow pattern, appears at tip mid-chord at $t/T_{pp} = 0.4$ and $t/T_{pp} = 0.6$. These time-resolved thick boundary layer onset lines get accumulated within the region of mid-chord and 80% chord near tip and locally moves upstream with time which can be an effect of the TLV. A weak corner stall occurs close to the TE of the tip at $t/T_{pp} = 0.2$, $t/T_{pp} = 0.4$ and $t/T_{pp} = 0.6$ and diminishes near the completion of the blade passage cycle. For Rotor II, the diffusion of pressure is observed near the tip LE showing flow separation. The distribution of pressure in the front portion of the blade becomes uniform with time. The attachment lines near the hub have no significant variation with time in this case too. Due to the early separation of flow in Rotor II, the streamlines are diverted towards the main flow direction. The shift of attachment line from radial to axial direction up to 70% span confirms this positive effect. A large stall region is developed above midspan downstream mid-chord at $t/T_{pp} = 0.4$ and $t/T_{pp} = 0.6$. It causes the flow to move towards tip resulting in corner stall. Generally, the interaction of the boundary layer flow with the TLV and PVs generates complex local skews on the thick boundary layer onset line in both cases. The phenomena of flow instability and stall inception in both rotors are directly related to the observed unsteady flow behaviour and that they might be linked to their stall.

Figure 6.27 shows the instantaneous 3D relative velocity streamlines passing through the blade passages of USW and Rotor II. The flow leakage starts from the tip LE in case of USW which causes flow separation on the SS. The spiral rolling of the streamlines occurs at $t/T_{pp} = 0.2$ following their strong dispersion at $t/T_{pp} = 0.4$. It is evident that the bubble-type breakdown happens in the TLV at this instant. The presence of this large recirculation region is observed downstream LE away from SS of USW. It is found that the flow in this region has high velocities which results in strong interaction with the mainstream flow thus causing breakdown and flow blockage. Rotor II experiences a different behaviour as there is a strong helical motion of 3D streamlines in front of tip LE. This phenomenon reduces the separation of flow from SS and limits it to the upstream mid-chord portion of the blade near the tip. At $t/T_{pp} = 0$, $t/T_{pp} = 0.2$ and $t/T_{pp} = 0.4$, it is observed that the 3D streamlines keep the nature of their rolling and are sound in spite of the interaction with the main flow till downstream mid-chord. At $t/T_{pp} = 0.6$, the flow leaking through the tip gap downstream the mid-chord interacts with the main flow as well as with the already existing 3D streamlines and develops a breakdown region. However, the breakdown region is much smaller than that observed for USW.

The instantaneous Lambda$_2$ surfaces developed in the USW and Rotor II at selected times are shown in Figure 6.28. The flow fields show that the formation of the TLV and PV is intermittent. Fluid irregularly spills around the leading edge into the adjacent blade passage at near-stall. The TLV fluctuates with time in the blade passages of both rotors. It is observed that the USW blade undergoes more vortex shedding than Rotor II. The TLV in USW twists and turns violently in the pitchwise direction, interacting with the pressure surface of the adjacent blade. The shed vortices travel from the suction surface to the pressure surface with a frequency that is non-synchronous with the rotor. A clear and large leakage vortex is detected here in case of USW which is generated in upstream at tip LE. At $t/T_{pp} = 0$, the streamwise velocity of the vortex core is quite high indicating the TLV stability. Some low-speed regions exist near the blade suction surface at this cross section. The low-speed regions indicate that the flow near the blade suction surface becomes unstable and presents a three-dimensional characteristic although the flow does not separate in the whole. The TLV appears less concentrated at some instants and its shape varies. At $t/T_{pp} = 0.4$, the TLV expands near tip mid-chord showing that it becomes unstable. In addition, the local low-speed regions near the blade suction surface continue to develop and connect to each other with a slight shift in circumferential and radial directions. The TLV then breaks down here and the vortex folds because the velocity in the vortex core is quite low. The broken TLV blocks the mainstream causes much loss. It is also observed that the PVs are sometimes weak and sometimes get strong enough to be comparable with the broken TLV. Moreover, the low-energy fluid begins to concentrate at the TE corner as for $t/T_{pp} = 0.6$ and $t/T_{pp} = 0.8$. The concentration can be due to the flow turning at the corner and the large amount of negative vorticity vortices inside the low-energy fluid. This corner vortex has a large scale and blocks the mainstream. This kind of corner vortex is different than the typical concentrated vortex, since it is formed by many discrete vortices. In addition, the results reveal that not all the vortices transported from the suction surface have concentrated in the corner, some of them move further to the middle of the rotor passage and transports low-energy fluid to the region. The TLV in the blade passage of Rotor II is not so strong. However, a strong PV is observed in front of tip LE. It is found that the breakdown of the PV is spiral-type for Rotor II as shown at $t/T_{pp} = 0.2$ and $t/T_{pp} = 0.4$. The TLV interacts with the main flow at tip mid-chord for $t/T_{pp} = 0.2$ and its breakdown occurs at $t/T_{pp} = 0.8$ downstream tip mid-chord. Before the leakage vortex breaks down, its location and scale are stable. The corner vortex does not exist in this case.

The unsteady simulation results indicate that the breaking of the TLV, its interaction with mainstream, the unstable flow on blade suction surface, and the interaction between the corner vortex and mainstream is the trigger for the loss for an axial blower at near stall condition.

Chapter 7

Conclusions and Recommendations

The effect of forward sweep on the three-dimensional velocity flow field of a single blade passage of an axial blower has been predicted by CFD. The forward sweep has been incorporated to the rotor blade sections without redesigning them from baseline. All geometrical and flow features are typically preserved while incorporating the forward sweep to the blade sections for comparison purposes. The results in the current study can be used as the basic design tool for axial blowers and can be helpful for the industries with minimum research investment on such appliances.

The steady state analyses have been carried out at different flow rates to obtain the characteristic curves of all the blowers. Unsteady simulations are run on two selected blowers for further understanding of the flow behaviour at near-stall condition. Based on the numerical results, it is concluded that the three-dimensional flow in axial flow turbomachinery of high rotational speed and moderate pressure rise can be simulated well with the help of advanced CFD techniques. The predictions rest on several assumptions and the complex flow phenomena cannot be predicted by theory alone.

To the knowledge of the author, this is the first time forward sweep only has been studied for axial blowers used specifically in network servers and telecommunication industry. The concept is found to be a helpful tool for better blower design with minimum effort/cost.

7.1 Summary and Conclusions

The numerical simulations for the validation studies have been carried out on different types of grid cells that include the tetrahedral with prism layers as well as the structured and unstructured hexahedral with boundary layers. The grid sizes are varied ranging from 0.25M to 1.8M cells. The structured hexahedral grids have produced better results than the other grids. The coarse grids have shown their inability to resolve the 3D effects within the rotor flow field, however they have done well when used for the comparison of integral values. The finer grids have not produced better validation results as the unsteady effects have become stronger with smaller cell sizes.

It is concluded that the k-ε model has poorly predicted the flow separation process, which is actually one of the major weaknesses of this model. Standard two-equation turbulence models often fail to predict the onset and the amount of flow separation under adverse pressure gradient conditions, which is true for this study. The real flow seems to be more separated than the calculations suggest. However, the model behaved very well at BEP and higher flow rates. The comparison between the efficiency curves based on the experimental and numerical values for hexa-grid with SST k-ω model shows a very good match at lower flow rates and at BEP, however, slightly higher efficiency values are obtained beyond the design point for numerical simulation. This raise can be due to the model sensitivity to the free stream value of ω. Moreover, the geometric simplifications like removal of fixtures from the actual geometry and extension of hub could have caused a slight increase in the efficiency beyond the BEP. An interesting feature observed in the overall comparison is that irrespective of computational grids and the turbulence models chosen, the Δp value is almost always the same at BEP in all the simulation results. This can be considered as grid independence but only at BEP. It can be concluded that the validation studies should not be limited to BEP and calculations must also be performed for other data points, especially at near-stall, to have the real comparison.

Detailed flow field results indicate that the forward swept blades cause a spanwise redistribution of flow rate and pressure toward the blade midspan while reducing tip load. The tip of FSW carries out work on the incoming fluid in advance compared with the blade sections at lower radii, due to its protrusion into the upstream relative flow field. The aerodynamic losses of highly FSW blower are decreased significantly near blade tip and hub endwall region. The high axial velocity observed near the hub reduces the secondary losses; consequently, pressure rise is higher in forward swept rotors. Higher pressure rise indicates efficient energy transfer. The lower overall pressure losses results in higher total pressure efficiency. The FSW blowers has a stall margin shifted towards lower flow rates thus an improved stall margin which favours the application of forward sweep. Moreover the efficiency for the off-load range and the total pressure peak provided by the FSW blowers are higher than by the USW blower. The static pressure loss in stall state is less drastic for high FSW blowers than for USW. Thus FSW blades tend to improve the blower performance and have the potential of wide-spread application.

The leakage flow originating from the tip clearance rolls up into a spiral to form a leakage vortex. The magnitude and intensity of the tip leakage vortex grow as the flow moves downstream. The mixing interaction between the tip leakage flow and the main flow produces low axial velocity regions. This leads to flow loss and blockage of the main flow in the tip region. There are underturning zones near and in the blade tip region. At BEP, all rotors feature a stable tip clearance vortex showing no significant effect of forward sweep. The tip clearance vortex does not break down and thus has a very weak effect on the performance of the rotors. As anticipated, forward sweeping resulted in minimizing the severity of flow separation at the suction surface. Forward sweep changes the streamline pattern in such a way that the suction surface streamline while being deflected towards the casing moves to the blade LE and the pressure surface streamline is deflected towards the hub. It can be concluded that forward sweep reduces the flow turning by the blade sections and deflects the flow towards hub.

The separation of the suction side boundary layer and vortex breakdown at near-stall condition are considered to be the reasons for the difficulties in obtaining accurate numerical predictions. The tip clearance vortex, formed by fluid crossing the tip gap very close to the LE, moves away from the suction side and radially inward as the rotor operates closer to the stall condition. It is noted that the three-dimensional nature of the flow separation near the tip is stronger than that near the hub for both selected rotors i.e. USW and Rotor II. It is evident that the variation of limiting streamlines and three-dimensional flow patterns near the tip are caused by the tip leakage vortex breakdown. It is found that large-scale flow oscillation are caused by the breakdown of the tip leakage vortex near the rotor tip. Comparing to design condition, the tip leakage vortex at near-stall condition generates and breaks down earlier and interacts more violently with mainstream, which causes large blockage and much loss near the rotor tip. The breakdown of the tip leakage vortex takes place due to the interaction between the leakage vortex and mainstream and brings about large-scale unsteady flow phenomena near the tip. The forward swept blade has been found to induce a vorticity component in the front portion of the passage at near-stall. However, the breakdown of TLV is severe in USW and consequently the associated losses.

Instantaneous velocity field simulations performed at near stall condition reveals the mechanism of the formation, development, and evolution of the leakage vortex and the corner vortex. The breakdown of the leakage vortex causes the track of leakage vortex to turn abruptly and strong unsteady vortices form there. Losses mainly come from the viscous and turbulent mixing before the leakage vortex breaks down and also from the strong interaction between the vortices and mainstream after the leakage vortex breaks down. The loss by the latter is much greater and is the main part of tip flow loss. The occurrence of a corner vortex is one of the main differences for rotor tip flow of USW and Rotor II at near-stall condition.

7.2 Future Recommendations

The current work can be extended by carrying out the same numerical simulations for higher sweep angles, for example 30°and 45°. This may help in further understanding of significant forward sweep effects on such blowers.

Further studies are necessary to find ways to control the flow structure near the casing, especially the formation of the low momentum area, for efficient operation with a wider stall margin.

It is recommended that the mesh be refined so that it more closely matches the grid size of the meshes used for these calculations. This will ensure improved accuracy as well as eliminate any error associated with a coarse mesh. Secondly, simulations should be run near stall conditions, and the results should be compared to experimental data to ascertain if the FLUENT® code (or any other CFD code) can accurately model stall conditions for finer grids. In general it can be said, that from the unsteady simulation the dynamic loading of the blade can be calculated. This simulation has to be very accurate especially concerning the wakes behind the blade LE. Therefore fine computational grids and sophisticated turbulence models are required. By knowing the dynamic forces from these simulations the structural design can be improved and the durability of the structure can be assessed.

The forward sweep application can be further studied for its effects on noise reduction. The noise level for a particular fan/blower design can be just as critical a property as flow rate or efficiency. Noise has no effect on cooling, but is very important to the system end user. Modern designs require minimal fan/blower noise to satisfy the users' demands of a quiet system. Aeroacoustic analysis of the blower will surely help to reduce the noise generation to an optimum level.

Large Eddy Simulations (LES) and Direct Numerical Simulations (DNS) are other possible approaches for such engineering flows at realistic Reynolds numbers. These methods allow us to study all details of the complex flow phenomena prevailing such as transition and the travel of wakes through the rotor passage influencing strongly the transition. However, such calculations are very expensive as they may take several months on the biggest supercomputers available. Hence, DNS is clearly not the method for routine engineering calculations, but it is an important tool for studying the details of certain complex flow phenomena such as near-wall turbulence and transition mechanisms, and it can be used increasingly for this purpose. LES can also be applied to such geometrically complex, fully 3D flow situations. The method has the ability to produce realistically the main features, including the unsteady behaviour as well as the time-averaged quantities. LES is clearly superior to RANS whenever large-scale structures dominate the behaviour and when unsteady effects like vortex shedding are present. LES calculations are cheaper than DNS, but they are still fairly costly. However, they are often affordable on modern computers, for some problems even on clusters of PCs, and they can be used for practical applications in cases where the aforementioned effects are important. For high Reynolds number flows involving walls, some special near-wall modelling is necessary and here LES/RANS coupling of some kind (Detached Eddy Simulation, DES) will be the method of the future. The further increase in computer power will certainly lead to an increased use and exploitation of DNS and LES.

Part V

Appendix

Appendix A

Abbreviations and Nomenclature

Abbreviations

2D	two-dimensional
3D	three-dimensional
BEP	best efficiency point
BL	boundary Layer
BSW	backward swept
CAD	computer aided design
CFD	computational fluid dynamics
DH	dihedral
DNS	Direct Numerical Simulation
Fig.	Figure
FSW	forward swept
FVM	finite volume method
GCI	grid convergence index
i.e.	id est (that is)
LDA	Laser Doppler Anemometry
LE	leading edge
LES	Large Eddy Simulation
MRF	Multiple Reference Frame
NRS	non-radial stacking
PS	pressure side/surface
PV/PVs	passage vortex/passage vortices
Q3D	quasi-three-dimensional
RANS	Reynolds Averaged Navier-Stokes
RDE	relative discretisation error
RE	Richardson extrapolation
Rotor I, II, II, IV	rotor with 5, 10, 15, 20 degree forward swept blade resp.
RS	radial stacking
RST	Reynolds Stress Transport
SIMPLE	Semi-Implicit Method for Pressure-Linked Equations

SOR	stable operating range
SS	suction side/surface
SST	shear stress transport
SW	sweep
TE	trailing edge
TLV	tip leakage vortex
uns	unstructured
USW	unswept

Latin Letters

$a,\ b$	linearised coefficients
$\vec{A}$	surface area vector
c	absolute velocity
C	blade chord length
$\mathrm{d}V$	infinitesimal control volume element having sides $\mathrm{d}x, \mathrm{d}y, \mathrm{d}z$
D	characteristic dimension, average diameter
f	volume forces in momentum equation, general variable, face
F	general function
F_s	factor of safety
g	gravitational acceleration, coefficient of error term
h	linear measure of grid
H	hydraulic head
I	turbulent intensity
$\vec{I}$	momentum
J	mass flux
k	turbulent kinetic energy
L	length
m	mass
$\dot{m}$	mass flow rate
M	force moment, million
n	rotor speed (r/s), interval number
N	rotor speed (rpm), number of grid cells, number
p	order of convergence/accuracy
P	pressure, power
Q	volume flow rate
r	radius, radial coordinate, grid refinement ratio
$\vec{r}$	displacement vector
Re	Reynolds number

s	blade pitch
S	source term in transport equation, source per unit volume
t	time
T	total time, time period
U	speed, circumferential speed
$u,\ v,\ w$	components of velocity vector in $x,\ y,\ z$ -direction
$\vec{v}$	fluid velocity vector
V	3D control volume
$\overline{u_i' \cdot u_j'}$	Reynolds or turbulent stress tensor
Z	blade count
y^+	dimensionless wall distance
$x,\ y,\ z$	cartesian coordinates

Greek Letters

α	under-relaxation factor
β	velocity/flow angle
χ	hub-tip ratio
δ_{sk}	skew angle
Δp	static pressure rise
Δt	numerical time step
ε	turbulent dissipation rate
η	total pressure efficiency (numerical efficiency)
η_H	hydraulic efficiency
γ	blade stagger angle
Γ	diffusion coefficient
λ	sweep angle
λ_2	second eigenvalue (Lambda$_2$ method)
μ	dynamic viscosity
μ_t	turbulent viscosity
ν	kinematic viscosity
ω	specific dissipation rate, angular speed
ϕ	Flow coefficient, any dependent variable in transport equation
Ψ	Pressure rise coefficient
ξ	Power coefficient
ρ	fluid density
σ	blade solidity, friction effect
τ	one-dimensional normal stress
θ	hub taper angle

Subscripts and Superscripts

0	initial condition (t=0), inlet
0h, 0c	hub at inlet, casing at inlet
3	outlet
avg	average
char	characteristic
e	exact value
f	face
H	hydraulic
i, j, k	indices (1, 2, 3 ...)
in	inlet
out	outlet
m	axial component, mid-span
n	interval number
nb	neighbour cells
p	pressure, order of convergence/accuracy
pp	passage-to-passage
P	pressure
s	static
SOU	second-order upwind
t	tangential component, time-dependent, tip
x, y, z	in x, y, z -direction

$*$	guessed value
$\bar{}$	time-averaged
$'$	fluctuating quantity, corrected value
$\vec{}$	vector quantity
T	transpose

Mathematical Operators

∇, grad	Nabla-Operator, Gradient
$\nabla\cdot$, div	Divergence
$\times$	Vector product
Δ	Laplace-Operator

List of Figures

1.1 Schematic of an Axial Flow Blower 4
1.2 Static Pressure Curve, Axial Blower 5
1.3 Axial Blower, PMDM 6

2.1 Flow in an Axial-Flow Machine 16
2.2 Flow in a Radial (Centrifugal) Fluid-Flow Machine 17
2.3 Propeller Fans 18
2.4 Direct Drive Tubeaxial Fan 19
2.5 Vaneaxial Blower 19
2.6 Multi-Stage Axial Blower 20
2.7 CAD-Geometry of Blower 20
2.8 Inlet and exit velocity diagrams 30

4.1 Original Axial Flow Blower 46
4.2 Performance Curves, Experimental Data 47
4.3 Typical Blower Test Facility 48
4.4 Validation Setup 48
4.5 Original Geometry of Axial Blower 49
4.6 Simplified Geometry: Blower Assembly 49
4.7 CAD Model Setups 50
4.8 Fluid Domains and Multiple Frames of Reference 51
4.9 Hybrid Grid and Cut-Plane Section 52
4.10 Surface Mesh, Rotor/Casing Assembly 52
4.11 Hub and Blade Prism Layers 53
4.12 Hybrid Mesh Quality 53
4.13 Passage-to-Passage Turbo Volume 53
4.14 Boundary Layers and Size Function on Blade Surfaces 54

4.15 Tip Clearance Resolution 54
4.16 Final Hexahedral Unstructured Mesh 55
4.17 Turbo Volume Cut Plane showing Better Mesh Quality 55
4.18 Boundary Conditions for Passage-to-Passage Setup 56
4.19 Convergence Curves 58
4.20 Pressure Rise vs. Inversed Number of Grid Cells 61
4.21 Comparison: Experimental and Numerical Δp vs. Q (Hybrid Grid) 63
4.22 Contours of Wall y-plus, k-ε Model 63
4.23 Contours of Wall y-plus, SST k-ω Model 64
4.24 Comparison: Experimental and Numerical Δp vs. Q (Hexa- Grid) 64
4.25 Contour of Wall y-plus, Passage-to-Passage (Hexa- Grid) 65
4.26 Efficiency Comparison (Hexa- Grid) 65
4.27 Overall Comparison: Δp vs. Q 66

5.1 Sweep, Dihedral, and Circumferential Skew 70
5.2 Forward and Backward Sweep 71
5.3 Positive and Negative Sweep, Forward Swept Blade 71
5.4 Forward Skewed Fan Blade 72
5.5 Unswept Old and New Reference Rotors 72
5.6 Performance Comparison, New USW Rotor 73
5.7 Blade Profile Sections and Main Edges of USW Rotor 74
5.8 Sweep Angle Description 76
5.9 Simplified Forward Sweep Technique 76
5.10 Moved Sections of Modified Rotors, Forward Sweep 77
5.11 View of Unswept and Swept Rotors 78

6.1 Streamlines on Suction Side for Different Grid Sizes 82
6.2 Comparison of Vortex Generated with Variation in Grid Size 83
6.3 Pressure Rise as a function of Inversed Number of Grid Cells 84
6.4 Static Pressure Rise vs. Flow Rate, Unswept and Swept Rotors 85
6.5 Total Pressure Efficiency, Unswept and Swept Rotors 86
6.6 Comparison of USW and Rotor II: Unsteady Case 87
6.7 Static Pressure Distribution: Suction Side 88
6.8 Static Pressure Distribution: Pressure Side 89
6.9 Static Pressure Distribution: Tip 90

6.10 Static Pressure Distribution: Rotor Outlet 91
6.11 Radial Velocity Distribution: Rotor Outlet 92
6.12 Static Pressure Distribution: Near-hub Section 93
6.13 Static Pressure Distribution: Midspan Section 93
6.14 Static Pressure Distribution: Near-tip Section 94
6.15 Surface Streamlines: Suction Side 95
6.16 Surface Streamlines: Pressure Side 96
6.17 Streamlines and Variation of Radial Velocity: Near-hub Section 98
6.18 Streamlines and Variation of Radial Velocity: Midspan Section 98
6.19 Streamlines and Variation of Radial Velocity: Near-tip Section 99
6.20 3D Streamlines through Tip Gap 101
6.21 Vortex Structure; Lambda$_2$ Method 102
6.22 Surface Streamlines near Stall Condition, Steady Case: Suction Side 104
6.23 Surface Streamlines near Stall Condition, Steady Case: Pressure Side . . . 105
6.24 3D Streamlines, Steady Case: Near Stall Condition 105
6.25 Vortex Structure, Steady Case: Near Stall Condition 106
6.26 Instantaneous Pressure Distribution and Surface Streamlines 107
6.27 Unsteady 3D Streamlines through the Blade Passage 108
6.28 Instantaneous λ_2 Surfaces 109

List of Tables

4.1 Experimental Data 46
4.2 Pressure Rise Data for Different Grids 61
4.3 Verification Results for Different Mesh Combinations 62
4.4 Relative Difference: Experimental and Numerical Data 66

5.1 Main Geometrical and Operational Characteristics of USW Rotor 74

6.1 Pressure Rise Data for Different Grids, New Reference USW 81
6.2 Discretisation Error and Uncertainty Results 84

Bibliography

[1] Improving fan system performance: A sourcebook for industry. U.S. Department of Energy's (DOE) Industrial Technologies Program and the Air Movement and Control Association International, Inc. (AMCA), 1989.

[2] Guide for the verification and validation of computational fluid dynamics simulations. Tech. Rep. G-077-1998, AIAA, 1998.

[3] EASy!™ design now for fans and blowers. In *SpinOffs*, vol. 2. Concepts NREC, 2004.

[4] *Handbook FLUENT®: User's Guide, Version 6.3.26.* ANSYS®, USA, 2006.

[5] *Best Practice Guideline for the CFD Simulation of Flows in the Urban Environment.* COST Action 732, May 2007.

[6] Ahn, C.-S., and Kim, K.-Y. Aerodynamic design optimization of a compressor rotor with navier–stokes analysis. *J. Power and Energy 217 Part A* (2003), 179–183.

[7] Anderson, J. D. *Computational Fluid Dynamics.* McGraw-Hill, 1995.

[8] Beiler, M. G., and Carolus, T. H. Computation and measurement of the flow in axial flow fans with skewed blades. *J. Turbomachinery 121* (January 1999), 59–66.

[9] Benner, M., Sjolander, S., and Moustapha, S. The influence of leading-edge geometry on secondary losses in a turbine cascade at the design incidence. In *Proceedings of ASME Turbo Expo 2003: Power for Land, Sea and Air* (June 2003), GT2003-38107.

[10] Bergner, J., Kablitz, S., Hennecke, D. K., Passrucker, H., and Steinhardt, E. Influence of sweep on the 3d shock structure in an axial transonic compressor. In *Proceedings of ASME Turbo Expo 2005: Power for Land, Sea, and Air* (June 2005), GT2005-68835.

[11] Bradbury, P. J., Nguyen, P. X., and jr. Jenkins, C. R. Axial flow fan. US 6,457,953 B1. U. S. Patent Documents, October 2002.

[12] Burguburu, S., Toussaint, C., Bonhomme, C., and Leroy, G. Numerical optimization of turbomachinery bladings. In *Proceedings of ASME Turbo Expo 2003: Power for Land, Sea, and Air* (June 2003), GT2003-38310.

[13] Casey, M., and Wintergerste, T. Best practice guidelines. Tech. Rep. 1, ERCOFTAC, January 2000.

[14] Celik, I. B., Ghia, U., Roache, P. J., Freitas, C. J., Coleman, H., and Raad, P. E. Procedure for estimation and reporting of uncertainty due to discretization in cfd applications. *J. Fluids Engineering 130*, 078001 (July 2008), 4.

[15] Corsini, A., and Rispoli, F. The role of forward sweep in subsonic axial fan rotor aerodynamics at design and off-design operating conditions. In *Proceedings of ASME Turbo Expo 2003: Power for Land, Sea, and Air* (June 2003), GT2003-38671.

[16] Corsini, A., and Rispoli, F. Using sweep to extend the stall-free operational range in axial fan rotors. In *Proc. Instn Mech. Engrs, Part A: J. Power and Energy* (2004), vol. 218, pp. 129–139.

[17] Daugherty, R. L., and Franzini, J. B. *Fluid Mechanics with Engineering Applications*, 8 ed. McGraw-Hill, 1985.

[18] Denton, J. D., and Dawes, W. N. Computational fluid dynamics for turbomachinery design. *Proc. Instn Mech. Engrs 213 Part C* (1999), 107–124.

[19] Denton, J. D., and Xu, L. The exploitation of three-dimensional flow in turbomachinery design. *Proc. Instn Mech. Engrs Vol 213 Part C* (1999), 125–137.

[20] Denton, J. D., and Xu, L. The effects of lean and sweep on transonic fan performance. In *Proceedings of ASME Turbo Expo 2002* (June 2002), GT-2002-30327.

[21] Dixon, S. L. *Fluid Mechanics and Thermodynamics of Turbomachinery*, 4th ed. Butterworth-Heinemann, 1998.

[22] Downie, R. J., Thompson, M. C., and Wallis, R. A. An engineering approach to blade designs for low to medium pressure rise rotor-only axial fans. *Experimental Thermal and Fluid Science 6* (May 1993), 376–401.

[23] Epple, P., Časlav Ilic, and Durst, F. Combined analytical and numerical radial fan performance optimization. In *Conference on Modelling Fluid Flow (CMFF'06)* (September 2006).

[24] Feng, J., Benra, F.-K., and Dohmen, H. Unsteady flow visualization at part-load conditions of a radial diffuser pump: by PIV and CFD. *J. Visualization 12*, 1 (2009), 65–72.

[25] Ferziger, J. H., and Perić, M. *Computational Methods for Fluid Dynamics*, 3 (rev.) ed. Springer, 2002.

[26] Friedrichs, J., Baumgarten, S., Kosyna, G., and Stark, U. Effect of stator design on stator boundary layer flow in a highly loaded single-stage axial-flow low-speed compressor. In *Proceedings of ASME Turbo Expo 2000* (May 2000), GT-616.

[27] Gallimore, S. J., Bolger, J. J., Cumpsty, N. A., Taylor, M. J., Wright, P. I., and Place, J. M. M. The use of sweep and dihedral in multistage axial flow compressor blading – `I` and `II`. *J. Turbomachinery 124* (October 2002), 521–541.

[28] Gbadebo, S. A., Cumpsty, N. A., and Hynes, T. P. Three-dimensional separations in axial compressors. *J. Turbomachinery 127* (April 2005), 331–339.

[29] Gbadebo, S. A., Cumpsty, N. A., and Hynes, T. P. Interaction of tip clearance flow and three-dimensional separations in axial compressors. *J. Turbomachinery 129* (October 2007), 679–685.

[30] Govardhan, M., Kumar, O. G. K., and Sitaram, N. Computational study of the effect of sweep on the performance and flow field in an axial flow compressor rotor. *Proc. IMechE, Part A: J. Power and Energy 221* (2007).

[31] Govardhan, M., Sastri, S. S. S. R. K., and Vishnubhotla, V. S. Experimental investigations of the three-dimensional flow in a large deflection turbine cascade with tip clearance. *J. Thermal Science 7*, 3 (September 1998), 149–164.

[32] Gümmer, V., Wenger, U., and Kau, H.-P. Using sweep and dihedral to control three-dimensional flow in transonic stators of axial compressors. In *ASME Turbo Expo 2000* (May 2000), no. 2000-GT-0491.

[33] Hah, C., Rabe, D. C., and Wadia, A. R. Role of tip-leakage vortices and passage shock in stall inception in a swept transonic compressor rotor. In *Proceedings of ASME Turbo Expo 2004: Power for Land, Sea, and Air* (June 2004), GT2004-53867.

[34] Hah, C., Voges, M., Mueller, M., and Schiffer, H.-P. Investigation of unsteady flow behavior in transonic compressor rotors with les and piv measurements. In *19th ISABE Conference* (Sep. 2009).

[35] Helming, K. Numerical analysis of sweep effects in shrouded propfan rotors. *J. Propulsion and Power 12*, 1 (Jan-Feb 1996), 139–145.

[36] Henry, V., and Rizzi, A. CFD analysis and design of ventilation fan blades. Tech. Rep. 99-08, Dept. of Aeronautics, Royal Institute of Technology, Stockholm, 1999.

[37] Hirsch, C. *Numerical Computation of Internal and External Flows*, vol. 1 & 2. John Wiley & Sons, 1994.

[38] Hofmann, W., and Ballmann, J. Some aspects of tip vortex behavior in a transonic turbocompressor. In *Proc. of the 16th ISABE* (2003), no. Paper No. 1223.

[39] Jang, C.-M., Li, P., and Kim, K.-Y. Optimisation of blade sweep in a transonic axial compresor rotor. *JSME International Journal 48, Series B* (2005), 793–801.

[40] Japikse, D., and Oliphant, K. N. Turbomachinery modeling: Explicit and implicit knowledge capturing (2005a). In *ASME Turbo Expo 2005: Power for Land, Sea and Air* (June 2005), GT2005-68099.

[41] Jeong, J., and Hussain, F. On the identification of a vortex. *J. Fluid Mech. 285* (1995), 69–94.

[42] Jiang, M., Machiraju, R., and Thompson, D. Detection and visualization of vortices. In *The Visualization Handbook*, C. D. Hansen and C. R. Johnson, Eds. Elsevier, Amsterdam, 2005, pp. 295–309.

[43] Keskin, A., Dutta, A. K., and Bestle, D. Modern compressor aerodynamic blading process using multi-objective optimization. In *ASME Turbo Expo 2006: Power for Land, Sea and Air* (May 2006), GT 2006-90206.

[44] Khaleghi, H., Boroomand, M., Tousi, A. M., and Teixeira, J. A. Stall inception in a transonic axial fan. *Proc. IMechE, Part A: J. Power and Energy 222* (2008), 199–208.

[45] Laurien, E., and Oertel, H. *Numerische Strömungsmechanik*, 3 ed. Vieweg +Teubner Verlag, 2009.

[46] Lee, G. H., Baek, J. H., and Myung, H. J. Structure of tip leakage flow in a forward-swept axial-flow fan. *Flow, Turbulence and Combustion 70* (2003), 241–265.

[47] Lei, V.-M., Spakovszky, Z. S., and Greitzer, E. M. A criterion for axial compressor hub-corner stall. *J. Turbomachinery 130*, 3 (July 2008), 031006 (1–10).

[48] Lewis, R. I., and Hill, J. M. The influence of sweep and dihedral in turbomachinery blade rows. *J. Mechanical Engineering Science 13*, 4 (1971).

[49] Lichtfuss, H.-J. Customized profiles - the beginning of an era. In *Proceedings of ASME Turbo Expo 2004, Power for Land, Sea, and Air* (June 2004), GT2004-53742.

[50] Liu, B., Wang, H., Liu, H., Yu, H., Jiang, H., and Chen, M. Experimental investigation of unsteady flow field in the tip region of an axial compressor rotor passage at near stall condition with stereoscopic particle image velocimetry. *J. Turbomachinery 126* (July 2004), 360–374.

[51] Liu, M., Liu, G., Joo, I., Song, L., and Wang, G. Development of in situ fan curve measurement for VAV AHU systems. *J. Solar Energy Engineering 127*, 2 (2005), 287–293.

[52] Loh, C., Nelson, D., and Chou, D. Optimization of heat sink design and fan selection in portable electronics environment. In *Semitherm Conference* (2000). http://www.enertron-inc.com/enertron-resources/library.php.

[53] Maaloum, A., Kouidri, S., and Rey, R. Aeroacoustic performance evaluation of axial flow fans based on the unsteady pressure field on the blade surface. *Applied Acoustics 65* (2004), 367–384.

[54] Matsunuma, T. Unsteady flow field of an axial-flow turbine rotor at a low reynolds number. *J. Turbomachinery 129* (April 2007), 360–371.

[55] McNulty, G. S., Decker, J. J., Beacher, B. F., and Khalid, S. A. The impact of forward swept rotors on tip clearance flows in subsonic axial compressors. *J. Turbomachinery 126* (October 2004), 445–454.

[56] Meyer, C. J., and Kröger, D. G. Numerical simulation of the flow field in the vicinity of an axial flow fan. *Int. J. Numerical Methods in Fluids 36* (2001), 947–969.

[57] Mohammed, K. P., and Raj, D. P. Investigations on axial flow fan impellers with forward swept blades. *J. Fluids Engineering* (Sep. 1977), 543– 547.

[58] Odeh, N., Grassie, T., Henderson, D., and Muneer, T. Modelling of flow rate in a photovoltaic-driven roof slate-based solar ventilation air preheating system. *Energy Conversion and Management 47*, 7-8 (2006), 909 – 925.

[59] Oertel, H. *Prandtl - Führer durch die Strömungslehre*, 12 ed. Vieweg+Teubner Verlag, 2008.

[60] Oertel, H. *Prandtl's Essentials of Fluid Mechanics*, 3 ed. Springer, 2009.

[61] Oertel, H., Böhle, M., and Dohrmann, U. *Strömungsmechanik*, 5 ed. Vieweg+Teubner Verlag, 2008.

[62] Park, K. Numerical study on the effects of blade leading edge shape to the performance of supersonic rotor. In *Proceedings of ASME Turbo Expo 2003: Power for Land, Sea, and Air* (June 2003), GT2003-38292.

[63] Passrucker, H., Engber, M., Kablitz, S., and Hennecke, D. K. The effect of forward sweep in a transonic compressor rotor. *Proc. IMechE, Part A: J. Power and Energy 217*, 4 (2003), 357–365.

[64] Ramakrishna, P. V., and Govardhan, M. Stall characteristics and tip clearance effects in forward swept axial compressor rotors. *J. Thermal Science 18*, 1 (2009), 40–47.

[65] Ramakrishna, P. V., and Govardhan, M. Study of sweep and induced dihedral effects in sub-sonic axial flow compressor passages – part 1: Design considerations – changes in incidence, deflection and streamline curvature. *Hindawi Int. J. Rotating Machinery* (December 2009).

[66] Ramakrishna, P. V., and Govardhan, M. Study of sweep and induced dihedral effects in sub-sonic axial flow compressor passages – part 2: Detailed study of the effects on tip leakage phenomena. *Hindawi Int. J. Rotating Machinery* (Jan 2010).

[67] Roache, P. *Verification and Validation in Computational Science and Engineering.* Hermosa, 1998.

[68] Roth, M., and Peikert, R. Flow visualization for turbomachinery design. Tech. rep., Swiss Center for Scientific Computing, ETH Zürich, Switzerland, 1996.

[69] Roy, B., Chouhan, M., and Sivadas, P. M. Aerodynamic studies on swept blades for axial flow fan/compressor. *IE (I) Journal –AS 85* (November 2005).

[70] Roy, C. J. Review of code and solution verification procedures for computational simulation. *J. Computational Physics 205* (2005), 131–156.

[71] Sasaki, T., and Breugelmans, F. Comparison of sweep and dihedral effects on compressor cascade performance. *J. Turbomachinery 120*, 3 (July 1998), 454–463.

[72] Schafhitzel, T., Vollrath, J. E., Gois, J., Weiskopf, D., Castelo, A., and Ertl, T. Topology-preserving $\lambda 2$-based vortex core line detection for flow visualization. In *Eurographics/IEEE-VGTC Symp. on Visualization* (2008), vol. 27.

[73] Schafhitzel, T., Weiskopf, D., and Ertl, T. Interactive investigation and visualization of 3d vortex structures. In *12th International Symposium on Flow Visualization '06* (September 2006).

[74] Shin, Y. H., Elder, R. L., and Bennett, I. Boundary layer measurement on the blade surface of a multi-stage axial flow compressor. In *Proceedings of ASME Turbo Expo 2003: Power for Land, Sea, and Air* (June 2003), GT2003-38183.

[75] Sieverding, C. H. Recent progress in the understanding of basic aspects of secondary flows in turbine blade passages. *ASME J. Eng. Gas Turbines Power 107* (1985), 248–257.

[76] Sirakov, B. T., and Tan, C.-S. Effect of unsteady stator wake—rotor double-leakage tip clearance flow interaction on time-average compressor performance. *J. Turbomachinery 125* (July 2003), 465–474.

[77] Smith, L. H., and Yeh, H. Sweep and dihedral effects in axial-flow turbomachinery. *J. Basic Engineering 85* (September 1963), 401– 416.

[78] Sørensen, D. N., and Sørensen, J. N. Toward improved rotor-only axial fans—part i: A numerically efficient aerodynamic model for arbitrary vortex flow. *J. Fluids Engineering 122* (June 2000), 318–323.

[79] Sørensen, D. N., Thompson, M. C., and Sørensen, J. N. Toward improved rotor-only axial fans—part ii: Design optimization for maximum efficiency. *J. Fluids Engineering 122* (June 2000), 323–329.

[80] Storer, J. A., and Cumpsty, N. A. Tip leakage flow in axial compressors. *J. Turbomachinery 113*, 2 (April 1991), 252–259.

[81] Tan, C., Yamamoto, A., Chen, H., and Mizuki, S. Flowfield and aerodynamic performance of a turbine stator cascade with bowed blades. *AIAA 42*, 10 (2004).

[82] Vad, J. Aerodynamic effects of blade sweep and skew in low-speed axial flow rotors at the design flow rate: an overview. In *Proc. Instn Mech. Engrs, Part A: J. Power and Energy* (2008), vol. 222, pp. 69–85.

[83] Vad, J., and Bencze, F. Three-dimensional flow in axial flow fans of non-free vortex design. *Int. J. Heat and Fluid Flow 19*, 6 (December 1998), 601–607.

[84] Vad, J., Bencze, F., Benigni, H., Glas, W., and Jaberg, H. Comparative investigation on axial flow pump rotors of free vortex and non-free vortex design. *Periodica Polytechnica Ser. Mech. Eng. 46*, 2 (2002), 107–116.

[85] Vad, J., Kwedikha, A. R. A., Horváth, C., Balczó, M., Lohász, M. M., and Régert, T. Aerodynamic effects of forward blade skew in axial flow rotors of controlled vortex design. *Proc. IMechE, Part A: J. Power and Energy 221* (2007), 1011–1023.

[86] Vad, J., Kwedikha, A. R. A., and Jaberg, H. Influence of blade sweep on the energetic behavior of axial flow turbomachinery rotors at design flow rate. In *Proceedings of ASME Turbo Expo 2004* (June 2004), GT2004-53544.

[87] Vad, J., Kwedikha, A. R. A., and Jaberg, H. Effects of blade sweep on the performance characteristics of axial flow turbomachinery rotors. *Proc. IMechE, Part A: J. Power and Energy 220*, 7 (2006), 731–751.

[88] Versteeg, H. K., and Malalasekera, W. *An Introduction to Computational Fluid Dynamics*, 1st ed. Longman, 1996.

[89] Wadia, A. R., Szucs, P. N., and Crall, D. W. Inner workings of aerodynamic sweep. *J. Turbomachinery 120* (October 1998), 671–682.

[90] Watanabe, H., and Zangeneh, M. Design of the blade geometry of swept transonic fans by 3d inverse design. In *Proceedings of ASME Turbo Expo 2003, Power for Land, Sea, and Air* (June 2003), GT2003-38770.

[91] White, F. M. *Fluid Mechanics*, 4th ed. McGraw-Hill Science Engineering, 1998.

[92] Wilcox, D. C. *Turbulence Modeling for CFD*, 2 ed. DCW Industries, Inc., 1998.

[93] Williams, M. The heart of your system: The fan. NMB Technologies, Inc.

[94] Wright, T., and Simmons, W. E. Blade sweep for low-speed axial fans. *J. Turbomachinery 112* (January 1990), 151–158.

[95] Yamada, K., Furukawa, M., Nakano, T., Inoue, M., and Funazaki, K. Unsteady three-dimensional flow phenomena due to breakdown of tip leakage vortex in a transonic axial compressor rotor. In *Proceedings of ASME Turbo Expo 2004, Power for Land, Sea, and Air* (June 2004), GT2004-53745.

[96] Yang, L., Hua, O., and Zhao-Hui, D. Optimization design and experimental study of low-pressure axial fan with forward-skewed blades. *Int. J. Rotating Machinery 2007* (2007), 10.

[97] Zhu, X., Lin, W., and Du, Z. Experimental and numerical investigation of the flow field in the tip region of an axial ventilation fan. *J. Fluids Engineering 127* (March 2005), 299–307.